FORMATION OF JETS BY IMPULSIVE ACCELERATION OF A CURVED FREE SURFACE

Thesis by

William Paul Gruber

In Partial Fulfillment of the Requirements

For the Degree of

Doctor of Philosophy

California Institute of Technology

Pasadena, California

1968

(Submitted May 21, 1968)

TABLE OF CONTENTS

ABSTRACT

The sudden axial acceleration of a column of liquid bounded at one end by a concave free surface has been found, experimentally, to produce a jet which issues from the free surface with a speed several times that imparted to the column.

Theoretical approximations to such flows, valid for small time, are formulated subject to the assumption that the fluid is inviscid and incompressible. In a special two-dimensional case, it is found that, for vanishingly small time, the velocity at the point on the free surface from which the jet emanates is $\pi/2$ times the velocity imparted to the column. The solutions to several problems in two and three dimensions assuming that the initial curvature of the free surface is small, lead to values for this ratio dependent upon the curvature- - the initial velocity in the case of axial symmetry exceeding that of the analogous two-dimensional problem by approximately 25%.

Experiments conducted upon the phenomenon give values systematically in excess of those predicted by the theory, although theory and experiment are in qualitative agreement with respect to the displacement of the free surface. It is suggested that the discrepancy is attributable to effects of finite curvature having been imperfectly accounted for in the axially-symmetric analysis.

Photographic materials on pp. 115, 120, and 121 are essential and will not reproduce clearly on Xerox copies. Photographic copies should be ordered.

ACKNOWLEDGMENTS

The author is indebted to Professor A. T. Ellis for guidance and encouragement throughout the course of the experimental work. Sincere thanks are due Professor T. Y. Wu for his assistance with the analysis.

The many intangible contributions to this undertaking made by his wife, Pamela, are gratefully acknowledged.

During the course of his graduate studies, the writer received financial assistance from the California Institute of Technology, the National Science Foundation, the Alfred P. Sloan Foundation, and the Office of Naval Research under contract Nonr-220(44).

Finally, the generous assistance rendered by Mrs. Barbara Hawk in the preparation of the manuscript is acknowledged.

NOMENCLATURE

Symbol	Definition	Page
a	two-dimensional shape parameter	7
a_n	ad hoc Fourier coefficient	10, 31
a_o, a_1, a_2	Fourier coefficients	32, 45
A	tube cross-sectional area	54
A_{2m}	coefficient in polynomial approximation	16, 39
A_n	ad hoc Fourier coefficient	35
b	two-dimensional shape parameter	25
B_n	ad hoc Fourier coefficient	35
$B_n(m)$	Fourier coefficient	38
c	acoustic velocity	53
$C_n(m)$	Fourier coefficient	40
d	column length in theoretical analysis	8, 43
d_s	distance from spark gap to bubble apex	71
D_{2m}	coefficient in polynomial approximation	41
D_n	Fourier coefficient	44
D_1	Fourier coefficient	46
$f(x)$	two-dimensional free surface height	27, 50
$F = \omega + i\overline{\omega}$	complex impulse function	9
F	scale of photograph	66
F_1	complex perturbation impulse function	21
$g(\xi'_s) = a - \eta'_s$		19
$g(r)$	axially symmetric free surface height	27, 43

Symbol	Definition	Page
g	gravitational acceleration	74
G	value of ψ_1 on $\eta = a$	20
h	$y_s' - y_s$	19
i	imaginary unit	
I_1', I	impulse	30, 37
J_n	Bessel function of first kind and order n	11
k	Fourier cosine transform variable	11
k_n	n^{th} positive root of $J_o'(k) = 0$	
m	integer	
n	integer	
n	coordinate normal to free surface	18
$\vec{n}$	unit normal vector	5
p	pressure	5
p_o	pressure jump across acoustic wave	53
p_m =	$2ma + i\zeta$	13
q	magnitude of velocity	54
q_n	normal component of q	54
Q, Q_1, Q_2	volume	68
r	radial coordinate	27
r', r'', r_n', r_n''	apparent radial coordinate on photograph	66, 67
R	geometrical radius of curvature at free surface midpoint	8, 28
R_s	spark bubble radius	78
R_t	tube radius	67

Symbol	Definition	Page
s	complex variable $\sigma + i\tau$	21
s	empirical correction factor	66
$s_m =$	$2ma - i\zeta$	13
t	time	5
$\vec{u}$	vector velocity	5
u	x-component of velocity	12
u_o	zeroth order Fourier component of u	15
u_o	perturbation in axial velocity	43
v	y-component of velocity	12
v_o	zeroth order Fourier component of v	15
v_o	velocity jump across acoustic wave	53
v_c	midpoint velocity	55
v_n	normal component of v	54
$\overline{v}$	spatial mean velocity	54
$\overline{v}_f$	spatial and temporal mean velocity based upon displaced volume at free surface	76
$\overline{v}_s$	spatial and temporal mean velocity based upon spark bubble volume	76
v_z	axial component of velocity	78
V_o	applied impulsive velocity in two dimensions	7
W	cosine transform of ω	11
x	two-dimensional horizontal coordinate	7
$\vec{x}$	position vector	
y	two-dimensional vertical coordinate	7
y_s	zeroth order free surface	8, 19

Symbol	Definition	Page
y_s'	perturbed free surface	19
z	axial coordinate	27
z	complex variable $x + iy$	9
z', z'', z_n', z_n''	apparent axial coordinate on photograph	66, 67
z_c'	apparent midpoint displacement	68
α	angle of incidence	53
β_{2m}	velocity ratio	58
$\gamma(x) =$	$e^{-\frac{i\pi x}{2}}$	15
δ	small parameter in axially-symmetric analysis	27, 43
Δ	free surface displacement	56
Δ_c	free surface displacement at midpoint	90
ϵ	small parameter in two-dimensional analysis	27, 50
ζ	complex variable $\xi + i\eta$	9
η	imaginary variable in ζ-plane	9
η	two-dimensional free surface height	47
η_o, η_1, η_2	approximations to η	48
η_s'	imaginary coordinate of perturbed free surface	19
θ	polar angle	54
ξ	real variable in ζ-plane	9
ξ_s'	real coordinate of perturbed free surface	19
ρ	fluid density	5
σ	real variable in s-plane	21
σ	surface tension	74

Symbol	Definition	Page
Σ	surface tension parameter	74
τ	imaginary variable in s-plane	21
φ	two-dimensional velocity potential	47
φ_0, φ_1	approximations to φ	49
φ, φ_m	two-dimensional impulse function	37
φ'	two-dimensional impulse function	28
$\varphi_0', \varphi_1', \varphi_2'$	approximations to φ'	29
χ, χ_m	axially-symmetric impulse function	40
χ'	axially-symmetric impulse function	31
$\chi_0', \chi_1', \chi_2'$	approximations to χ'	31
ψ	two-dimensional impulse function	19
ψ_0	zeroth order approximation to ψ	18
ψ_1	first order approximation to ψ	20
ω	two-dimensional impulse function	6
$\bar{\omega}$	harmonic conjugate of ω	9
Ω	axially-symmetric impulse function	43
Ω_0, Ω_1	approximations to Ω	43

Subscripts

x, y, r, z, t	partial differentiation	

Superscripts

(1), (2)	order of approximation	50, 51

I. INTRODUCTION

The problem to be considered is that of the motion of a body of liquid, partially bounded by a free surface, subsequent to the application of a system of forces which cause it to accelerate impulsively. Attention will be given specifically to geometries having a free surface concave into the fluid and in which the applied accelerations are more or less normal to the free surface. A prominent feature of many flows of this type is the formation of a liquid jet which issues from the free surface approximately parallel to the applied acceleration. An example is the splash which often follows the rapid setting down of a liquid-filled cup.

The formation of these jets has received attention for its role in the initiation and propagation of explosions. Bowden and McOnie(1) have found that the presence of voids within a liquid explosive greatly increases its shock sensitivity and leads to much higher reaction rates than prevail in a homogeneous liquid. They conclude on the basis of evidence cited below, that jets emanating from the surfaces of the voids serve to disperse the explosive and increase the surface area available for reaction.

Bowden and Brunton(2) and Brunton(3), in connection with an investigation of liquid-solid impact, employed jets formed by the sudden extrusion of a liquid through a circular hole. When the initial free surface was concave into the liquid, they observed a small jet to form at the tip of the main stream and move two or three times as fast; no

such precursor jets were found when the initial free surface was planar.

Watson and Gibson(4) caused an explosively-created shock wave to impinge from below upon several hemispherical air bubbles trapped beneath a thin film of plastic in contact with the top of a liquid-filled tank. The resulting jets were found to move fast enough to pit an aluminum specimen placed in their path. Watson and Gibson speculate that a mechanism of this sort may be operating within a cloud of cavitation bubbles - - the pressure wave from a collapsing bubble possibly causing a neighboring bubble to form a jet. Several studies (5), (6), (7) have implicated jets from collapsing bubbles as a possible cause of cavitation damage.

The work of Bowden and his students, summarized in Ref. (8), is illustrative of the varied geometries which can give rise to jets. In addition to the extrusion process mentioned above, they have observed jets when a thin layer of liquid with an elliptical void was squeezed between a hammer and anvil. Jets were found to emanate into the void from the two points having the greatest initial curvature. The phenomenon also occurs when two droplets, impacted in the hammer-anvil device, make contact. Jets issue in this case from the points of maximum curvature on the resulting "8"-shape. Finally, two explosion bubbles collapsing out of phase, Ref. (9), can exhibit an interaction which leads to the formation of jets, first in one bubble and then in the other.

The theory relevant to the formation of jets at a liquid free surface is not at all well-developed. The phenomenon seems quite similar to that occurring during the collapse of a conical or wedge-shaped liner

in a high-explosive charge, Ref. (10); however, the problem is much more difficult since the mass is distributed through a region of space rather than concentrated in a very thin layer. This requires that the conservation laws be applied in the form of differential equations rather than their more easily handled integrated forms. An attempt to treat the phenomenon in terms of the theory of shaped-charges has, nevertheless, been made by Kozirev (11).

Birkhoff and Caywood (12), studied the flow near the base of the up-jet formed behind a wedge after its entry into a tank of water. By matching, at one point, the magnitude and direction of a theoretical, steady, two-dimensional, jet flow to that determined experimentally, they found that the field everywhere was adequately described.

The discharge from a sharp-edge, two-dimensional orifice has been examined analytically by Curle (13). He considered the problem for both large and small time assuming an initially planar free surface. The sharp edges, however, lead to unrealistically high velocities and hence to a free surface shape for small time which does not seem physically reasonable.

Recently, some numerical work has been done concerning jets in real fluids. The shaped-charge problem has been considered by Harlow and Pracht (14); while Harlow and Shannon (15) have examined the phenomena, including the up-jet, associated with the impact of a liquid drop against a plane free surface.

The analytical work presented in the following represents an attempt to predict the velocity of the jet formed as a result of

impulsive acceleration in systems similar to Bowden's extrusion device. Particular attention is given to the velocity along the free surface just as the motion commences. Experiments were conducted on the phenomenon using long air bubbles rising through water in a slender circular tube. The sudden downward acceleration of such a bubble, by means of a rapidly expanding spark bubble created above it, leads to jets closely resembling those discovered by Bowden.

II. FORMULATION AND SOLUTION OF SOME BOUNDARY VALUE PROBLEMS

1. Assumptions and Basic Equations

The fluid will be assumed to be inviscid and incompressible in the theoretical analysis. No experimental evidence has been found to suggest that viscosity plays any important part in the phenomena to be considered. Compressibility, however, must be invoked to explain certain features of the flow and it is neglected in the analysis with the understanding that its effects must ultimately be estimated. In addition, forces due to surface tension and gravity will be neglected as compared with other forces acting on the fluid.

With these simplifications, the equations to be satisfied by the velocity, $\vec{u}(\vec{x}, t)$, and pressure, $p(\vec{x}, t)$, are

$$\nabla \cdot \vec{u} = 0 \tag{1.1}$$

and

$$\frac{D\vec{u}}{Dt} = -\frac{1}{\rho} \nabla p \tag{1.2}$$

where t is the time

ρ is the fluid density

and $\frac{D}{Dt}$ denotes time-differentiation following a fluid element.

Boundary conditions suitable to this pair of equations are

$$\vec{u} \cdot \vec{n} = 0 \qquad \text{on rigid boundaries} \tag{1.3}$$

$$p = 0 \qquad \text{on free surfaces} \tag{1.4}$$

and

$$\vec{u}\cdot\vec{n} \qquad \text{specified} \qquad (1.5)$$

over the remainder, if any, of the surface enclosing the fluid. $\vec{n}$ denotes the outward-pointing normal to this surface. Finally, the kinematic boundary condition

$$\frac{DF}{Dt} = 0 \qquad (1.6)$$

must be satisfied on the free surface $F(\vec{x}, t) = 0$.

Following Lamb, Ref. (16, p. 10), (see also (17)), one assumes that the fluid is subjected to a system of arbitrarily large pressures acting over a vanishingly small interval of time. Integration of the Eulerian equation of motion, (1.2), with respect to the time then yields

$$\vec{u}(\vec{x}, 0^+) = \nabla\omega \qquad (1.7)$$

where

$$\omega(\vec{x}) = -\frac{1}{\rho}\int_{o^-}^{o^+} p\,dt \qquad (1.8)$$

and the flow has been assumed to start from rest. The requirement that $\vec{u}(\vec{x}, 0^+)$ satisfies the continuity equation, (1.1), then becomes

$$\nabla^2\omega = 0 \qquad (1.9)$$

and the boundary conditions (1.3), (1.4), and (1.5) now read

$$\nabla\omega\cdot\vec{n} = 0 \qquad \text{on rigid boundaries} \qquad (1.10)$$

$$\omega = 0 \qquad \text{on free surfaces} \qquad (1.11)$$

and

$$\nabla\omega\cdot\vec{n} \qquad \text{specified} \quad , \qquad (1.12)$$

respectively. Integration of the kinematic boundary condition,

(1.6), leads to

$$F(\vec{x}, 0^+) = 0 \quad .$$

This has no relevance to the problem solved by ω since the free surface at $t = 0^+$ will not be displaced from its initial position.

To the boundary conditions resulting from the conventional formulation, one may add

$$\omega \qquad \text{specified} \tag{1.13}$$

over a portion of the bounding surface. From Eq. (1.8) it is clear that $-\rho\omega$ represents the impulse per unit area acting at any point in the flow.

2. The Solution of an Exact Two-Dimensional Problem

Consider the application of Eqs. (1.9) through (1.12) to the problem depicted in Fig. 1(a). The fluid is confined between infinite, rigid, parallel walls situated at $x = \pm 1$ and the free surface profile is given by

$$\cos \frac{\pi x}{2} \sinh \frac{\pi y_s}{2} = a \tag{2.1}$$

where a is a positive constant and the subscript s denotes a quantity evaluated on the free surface. An impulsive velocity distribution, $V_o(x)$, is specified along $y = 0$, $|x| < 1$. The boundary value problem for ω in the region occupied by fluid is thus

$$\nabla^2\omega = 0 \tag{2.2}$$

$$\frac{\partial \omega}{\partial x} = 0 \quad \text{on} \quad x = \pm 1, \quad y > 0 \tag{2.3}$$

$$\frac{\partial \omega}{\partial y} = V_o(x) \text{ on } \quad y = 0, \quad |x| < 1 \tag{2.4}$$

$$\omega = 0 \quad \text{on} \quad \cos \frac{\pi x}{2} \sinh \frac{\pi y_s}{2} = a \tag{2.5}$$

and $(\nabla\omega)_s$, the velocity at the free surface is sought. All quantities in the theoretical analysis will be assumed dimensionless - - the characteristic length and velocity being the channel half-width and the mean value of V_o, respectively.

Before proceeding with the solution, several properties of the free surface geometry will be mentioned. The equation describing the free surface can be written in the form

$$y_s = \frac{2}{\pi} \sinh^{-1} \frac{a}{\cos \frac{\pi x}{2}} \tag{2.6}$$

It follows that the radius of curvature, R, at the midpoint of the free surface is given by

$$\frac{1}{R} = y_s''(0) = \frac{\pi}{2} \frac{a}{\sqrt{a^2+1}} \tag{2.6'}$$

and thus depends upon the distance d shown in Fig. 1(a). In the important case $a^2 \gg 1$, however, this dependence is largely eliminated and the radius approaches $\frac{2}{\pi}$ or about 0.637 channel half-widths. Equation (2.6) can also be written in the form

$$y_s = \frac{2}{\pi} \log \left[\frac{a}{\cos \frac{\pi x}{2}} + \sqrt{\frac{a^2}{\cos^2 \frac{\pi x}{2}} + 1} \right] ,$$

so it is clear that the free surface height is logarithmically singular near the channel walls. Finally, in case $a^2 \gg 1$, the free surface height measured from $y = d$ can be shown to be

$$y_s - d = - \frac{2}{\pi} \log \cos \frac{\pi x}{2} \quad . \tag{2.7}$$

Equation(2.7) and an experimental free surface are shown in Fig. 2. The radius, R, and d, the column length, are plotted against a in Fig. 3.

Returning now to the problem posed by Eqs. (2.2) through (2.5), let a conformal transformation be defined by

$$\zeta = \sin \frac{\pi z}{2} \tag{2.8}$$

and a complex impulse function by

$$F(\zeta) = \omega(\xi, \eta) + i\bar{\omega}(\xi, \eta)$$

where

$$z = x + iy$$

and

$$\zeta = \xi + i\eta \quad .$$

The mapping defined above transforms the region occupied by the fluid in the z-plane onto the infinite strip $a < \eta < a$ in the ζ-plane. The correspondence between points in the two planes is shown in Fig. 1(b). Since the complex conjugate velocity, u-iv, in the z-plane is

$$u - iv = \frac{dF}{d\zeta}\frac{d\zeta}{dz} = \frac{\pi}{2}\cos\frac{\pi z}{2}\frac{dF}{d\zeta} \quad , \tag{2.9}$$

the problem for ω may be reformulated in the ζ-plane as

$$\nabla^2\omega = 0 \quad \text{in} \quad 0 < \eta < a \tag{2.10}$$

$$\omega = 0 \quad \text{on} \quad \eta = a \tag{2.11}$$

$$\frac{\partial\omega}{\partial\eta} = 0 \quad \text{on} \quad \eta = 0 \quad , \quad |\xi| > 1 \tag{2.12}$$

and

$$\frac{\partial \omega}{\partial \eta} = \frac{2}{\pi} \frac{1}{\cos \frac{\pi x}{2}} V_o(x) \quad \text{on} \quad \eta = 0 \ , \quad |\xi| < 1 \tag{2.13}$$

where x is given implicitly by

$$\xi = \sin \frac{\pi x}{2} \quad \text{along} \quad \eta = 0 \ , \quad |\xi| < 1 \ . \tag{2.14}$$

As conclusions will ultimately be drawn with respect to axially-symmetric flows, consideration will be given only to functions $V_o(x)$ which are even. Furthermore, linearity of the problem permits $V_o(x)$ to be expressed as a Fourier series and the response to each Fourier component computed separately. Thus

$$V_o(x) = \sum_o a_n \cos n\pi x \tag{2.15}$$

since the functions

$$\cos n\pi x$$

form a complete orthogonal set over $-1 \leqslant x \leqslant 1$. The choice $a_o = 1$, corresponding to a mean upward velocity of unity, will be made in the subsequent analysis. Denoting the response to the n^{th} term of this series by ω_n, the problem for ω_n is exactly that given by Eqs. (2.10) through (2.14) with (2.13) modified to read

$$\frac{\partial \omega_n}{\partial \eta} = \frac{2}{\pi} \frac{\cos n\pi x}{\cos \frac{\pi x}{2}} \ . \tag{2.16}$$

The problem in the ζ-plane will be solved using the Fourier cosine transform pair

$$W_n(\eta, k) = \int_o^\infty \omega_n(\xi, \eta)\cos k\xi \, d\xi \tag{2.17}$$

$$\omega_n(\xi, \eta) = \frac{2}{\pi} \int_o^\infty W_n(\eta, k)\cos k\xi \, dk \quad . \tag{2.18}$$

Application of transformation (2.17) to the problem solved by ω_n results in

$$\frac{d^2 W_n}{d\eta^2} - k^2 W_n = 0 \qquad \text{in} \qquad 0 < \eta < a \tag{2.19}$$

$$W_n = 0 \qquad \text{on} \qquad \eta = a \tag{2.20}$$

and

$$\frac{dW_n}{d\eta} = \frac{2}{\pi} \int_o^1 \frac{\cos n\pi x}{\cos \frac{\pi x}{2}} \cos k\xi \, d\xi \qquad \text{on} \qquad \eta = 0 \tag{2.21}$$

where

$$x = \frac{2}{\pi} \sin^{-1} \xi \tag{2.22}$$

as the problem to be solved by W_n. The change of variable

$$\xi = \sin\varphi \quad ,$$

in the integral of Eq. (2.21) gives

$$\frac{dW_n}{d\eta} = \frac{2}{\pi} \int_o^{\pi/2} \cos 2n\varphi \cos(k\sin\varphi) d\varphi \tag{2.23}$$

which is an integral representation of $J_{2n}(k)$, the Bessel function of the first kind and order $2n$. (See, for example, Ref. (18), p. 150).

Now the solution of Eq. (2.19) satisfying boundary condition

(2.20) is

$$W_n(\eta, k) = c_n(k)\sinh k(\eta - a) \tag{2.24}$$

where c_n may be shown to be

$$c_n = \frac{J_{2n}(k)}{k \cosh ka}$$

through use of Eq. (2.23). Finally, inversion by means of Eq. (2.18) gives

$$\omega_n(\xi, \eta) = \frac{2}{\pi} \int_o^\infty \cos k\xi \sinh k(\eta - a) \frac{J_{2n}(k)}{k \cosh ka} \, dk \quad . \tag{2.25}$$

The complex velocity, $u_n - iv_n$, for each of the Fourier components is

$$u_n - iv_n = \frac{dF_n}{dz} = \frac{dF_n}{d\zeta} \frac{d\zeta}{dz}$$

where the expression

$$\begin{aligned} \frac{dF_n}{d\zeta} &= \frac{\partial \omega_n}{\partial \xi} - i \frac{\partial \omega_n}{\partial \eta} \\ &= -i \frac{2}{\pi} \int_o^\infty \frac{\cos k(\zeta - ia)}{\cosh ka} J_{2n}(k) dk \end{aligned} \tag{2.26}$$

follows from Eq. (2.25). If the trigonometric and hyperbolic functions appearing in (2.26) are written in terms of exponential functions and the quantity $\frac{1}{1+e^{-2ka}}$ is expanded in a geometric series, term-by-term integration results in a series of integrals of the form

$$\int_o^\infty J_{2n}(k) e^{-sk} dk$$

where $Re(s) > 0$. These are readily identified with the Laplace

transform of $J_{2n}(k)$:

$$\int_0^\infty J_{2n}(k)e^{-sk}dk = \frac{1}{\sqrt{s^2+1}\ (s+\sqrt{s^2+1})^{2n}}$$

(See, for example, Ref. (19), p. 1027). The result is

$$\frac{dF_n}{d\zeta} = -\frac{2i}{\pi}\left\{\sum_{m=o}^{\infty}(-1)^m \frac{1}{\sqrt{s_m^{\,2}+1}\ (s_m+\sqrt{s_m^{\,2}+1})^{2n}} - \sum_{m=1}^{\infty}(-1)^m \frac{1}{\sqrt{p_m^{\,2}+1}\ (p_m+\sqrt{p_m^{\,2}+1})^{2n}}\right\} \qquad (2.27)$$

where

$$s_m = 2ma - i\zeta$$

$$p_m = 2ma + i\zeta \quad .$$

Although the structure of the solution is by no means evident in general, certain limiting cases are not difficult to examine.

The velocity at the midpoint of the free surface will be considered first. Substitution of $\zeta = ia$ into (2.27) and rearrangement of the summation index in the second sum gives

$$\left.\frac{dF_n}{d\zeta}\right|_{\zeta=ia} = -\frac{4i}{\pi}\sum_{m=o}^{\infty}(-1)^m \frac{1}{\sqrt{c_m^{\,2}+1}\ (c_m+\sqrt{c_m^{\,2}+1})^{2n}}$$

where

$$c_m = (2m+1)a \quad .$$

Since the midpoint of the free surface is $z_1 = id$ in the z-plane, the

velocity there is simply

$$(u_n - iv_n)_{z_1} = \frac{\pi}{2} \cos \frac{\pi z_1}{2} \left. \frac{dF_n}{d\zeta} \right|_{\zeta = ia}$$

$$= \frac{\pi}{2} \sqrt{1+a^2} \left. \frac{dF_n}{d\zeta} \right|_{\zeta = ia} .$$

Thus

$$u_n(0, d) = 0$$

and

$$v_n(0, d) = 2\sqrt{1+a^2} \sum_{m=0}^{\infty} (-1)^m \frac{1}{\sqrt{c_m^2+1}\ (c_m+\sqrt{c_m^2+1})^{2n}} \qquad (2.28)$$

That the tangential component of velocity vanishes along the free surface is evident in general from Eq. (2.25), and is a consequence of the fact that the pressure gradient has no component parallel to the free surface. This result has been shown to hold for a wide class of perturbation flows by Wang and Wu, (Ref. 20). v_n from Eq. (2.28) has been plotted against a for several values of n in Fig. 4. Also shown is the special case $n = \frac{1}{2}$ which will be taken up shortly. The main conclusion to be drawn from this figure is the physically obvious one that when the free surface is several channel-widths or more removed from the plane along which the impulsive velocities are specified, i.e. $a \gg 1$, the details of the velocity distribution are of no importance, knowledge of the mean value (corresponding to $n = 0$) being sufficient to determine the velocity at the free surface.

Returning now to Eq. (2.27), the velocity at points on the plane

tangent to the free surface at its midpoint, will be examined in the limit $a \to \infty$. From Eq. (2.8) it can be shown that in this approximation $\zeta = \zeta_o = iae^{-\frac{i\pi x}{2}}$, so that Eq. (2.27) becomes

$$\left.\frac{dF_o}{d\zeta}\right|_{\zeta=\zeta_o} = -\frac{2i}{\pi a}\left[\sum_{m=o}^{\infty}\frac{(-1)^m}{2m+\gamma(x)} - \sum_{m=1}^{\infty}\frac{(-1)^m}{2m-\gamma(x)}\right]$$

where

$$\gamma(x) = e^{-\frac{i\pi x}{2}}$$

when

$$n = 0 \quad ,$$

and gives

$$\left.\frac{dF_n}{d\zeta}\right|_{\zeta=\zeta_o} = O\left(\frac{1}{a^{2n+1}}\right) \quad \text{when} \quad n = 1, 2, 3, \ldots .$$

Since

$$z = x + i\,\frac{2}{\pi}\sinh^{-1}a$$

for the case in question,

$$\frac{d\zeta}{dz} = \frac{\pi}{2}\cos\frac{\pi z}{2} = \frac{\pi a}{2}e^{-\frac{i\pi x}{2}} \quad \text{when} \quad a \gg 1 \quad ,$$

so the complex velocity in the z-plane along $z = x + id$ is

$$u_o - iv_o = -i\gamma(x)\left[\sum_{m=o}^{\infty}\frac{(-1)^m}{2m+\gamma(x)} - \sum_{m=1}^{\infty}\frac{(-1)^m}{2m-\gamma(x)}\right] \quad . \qquad (2.29)$$

At the point $z = id$, the series in Eq. (2.29) combine to give

$$(u_o - iv_o)_{id} = -2i \sum_{m=o}^{\infty} \frac{(-1)^m}{2m+1} = -\frac{\pi}{2} i \quad .$$

Thus the limiting velocity at the midpoint of the free surface is $\frac{\pi}{2}$ times the mean value of the upward velocity imparted to the column.

The real and imaginary parts of Eq. (2.29) are shown versus x in Fig. 5 together with a polynomial approximation to $u_o(x, d)$ found using the method of least squares (see Appendix A). While these quantities are of little intrinsic interest (except, of course, when $x = 0$); the fact that

$$\omega_o(x, d) = \int_o^x u_o(x', d)dx' \tag{2.30}$$

permits ω_o to be determined along the plane in question. Using the polynomial approximation of Appendix A in Eq. (2.30) gives

$$\omega_o(x, d) = -\sum_{m=1}^{5} A_{2m} x^{2m} \tag{2.31}$$

where

$$A_2 = 1.152$$

$$A_4 = -2.585$$

$$A_6 = 3.533$$

$$A_8 = -2.585$$

$$A_{10} = 0.7522 \quad .$$

This function will play an important role in the later analysis.

Attention will now be given to another special case. As has been

pointed out, the functions $\cos n\pi x$ form a complete orthogonal set in the range $-1 < x < 1$ and thus, once the response to each of these functions is determined; the response to an arbitrary excitation may be found by Fourier analysis. When the excitation is given by

$$V_o(x) = \frac{\pi}{2} \cos \frac{\pi x}{2} \quad , \tag{2.32}$$

however, the solution is particularly simple (the function has been normalized to mean value unity over $-1 < x < 1$).

In this case, boundary condition (2.21) may be integrated in closed form (replacing n with $\frac{1}{2}$) to give

$$\frac{dW_{\frac{1}{2}}}{d\eta} = \frac{\sin k}{k} \qquad \text{on} \qquad \eta = 0$$

so that

$$\omega_{\frac{1}{2}}(\xi, \eta) = \frac{2}{\pi} \int_o^\infty \frac{\sin k \cos k\xi \sinh k(\eta - a)}{k^2 \cosh ka} \, dk$$

from Eq. (2.18).

Solving for the normal velocity along the free surface in the ζ-plane:

$$\left.\frac{\partial \omega_{\frac{1}{2}}}{\partial \eta}\right|_{\eta=a} = \frac{2}{\pi} \int_o^\infty \frac{\sin k \cos k\xi \, dk}{k \cosh ka} \quad .$$

This integral is evaluated in Appendix B and shown to be

$$\left.\frac{\partial \omega_{\frac{1}{2}}}{\partial \eta}\right|_{\eta=a} = \frac{2}{\pi} \tan^{-1} \frac{\sinh \pi/2a}{\cosh \pi\xi/2a} \quad . \tag{2.33}$$

The normal velocity along the free surface in the z-plane is

$$\left(\frac{\partial \omega}{\partial n^{\frac{1}{2}}}\right)_s = \frac{\pi}{2} \cos \frac{\pi z_s}{2} \left.\frac{\partial \omega}{\partial \eta^{\frac{1}{2}}}\right|_{\eta=a}$$

$$= \left(\sinh^2 \frac{\pi y_s}{2} + \cos^2 \frac{\pi x}{2}\right)^{\frac{1}{2}} \tan^{-1} \frac{\sinh \pi/2a}{\cosh \pi\xi/2a} \qquad (2.34)$$

where $(\ )_s$ denotes a quantity evaluated on the free surface in the z-plane, and

$$\xi = \sin \frac{\pi x}{2} \cosh \frac{\pi y_s}{2} \quad .$$

Note that at the midpoint of the free surface in the limit $a \to \infty$,

$$\left(\frac{\partial \omega}{\partial n^{\frac{1}{2}}}\right)_s \to \frac{\pi}{2}$$

and the result found in the more general analysis above is recovered. For comparison with previous results, Eq. (2.34) is plotted in Fig. 4 as a function of a for $x = 0$.

3. A Perturbation of the Exact Solution

In order to examine the sensitivity of the exact solution of Section 2 to small changes in the free surface shape, such a change will be made and the effects upon the velocity at points on the free surface studied. The perturbation problem will be formulated in the ζ-plane of Fig. 1.

Assume first that a zeroth order solution, $\psi_o(\xi, \eta)$, satisfying

$$\nabla^2 \psi_o = 0 \qquad \text{in} \qquad 0 < \eta < a \qquad (3.1)$$

$$\frac{\partial \psi_o}{\partial \eta} = 0 \qquad \text{on} \qquad \eta = 0 \ , \quad |\xi| > 1 \tag{3.2}$$

$$\frac{\partial \psi_o}{\partial \eta} = V(\xi) \qquad \text{on} \qquad \eta = 0 \ , \quad |\xi| < 1 \tag{3.3}$$

and

$$\psi_o = 0 \qquad \text{on} \qquad \eta = a \tag{3.4}$$

is known. This solution, of course, will be some linear combination of the ω_n's determined in Section 2.

Now imagine that the free surface shape in the physical (z) plane is given by

$$y_s' = y_s + h(x) \tag{3.5}$$

where

$$y_s = \frac{2}{\pi} \sinh^{-1} \frac{a}{\cos \frac{\pi x}{2}} \tag{3.6}$$

and $h(x)$ is, in some sense, small compared to y_s. The curve onto which this is mapped by the transformation

$$\zeta = \sin \frac{\pi z}{2} \tag{3.7}$$

will be taken to be

$$\eta_s' = a + g(\xi_s') \tag{3.8}$$

where, again, $g(\xi_s')$ is assumed "small" and the subscript s denotes the free surface.

If the solution to this new problem is $\psi(\xi, \eta)$, then it will satisfy

$$\nabla^2 \psi = 0 \qquad \text{in} \qquad 0 < \eta < a + g(\xi_s') \tag{3.9}$$

$$\frac{\partial \psi}{\partial \eta} = 0 \qquad \text{on} \qquad \eta = 0 \ , \qquad |\xi| > 1 \tag{3.10}$$

$$\frac{\partial \psi}{\partial \eta} = V(\xi) \qquad \text{on} \qquad \eta = 0 \ , \qquad |\xi| < 1 \tag{3.11}$$

and

$$\psi = 0 \qquad \text{on} \qquad \eta = a + g(\xi_s') \tag{3.12}$$

Further, if ψ is assumed to be of the form

$$\psi = \psi_o + \psi_1 \tag{3.13}$$

where $\psi_1 \ll \psi_o$, then ψ_1 must satisfy

$$\nabla^2 \psi_1 = 0 \qquad \text{in} \qquad 0 < \eta < a + g(\xi_s') \tag{3.14}$$

$$\frac{\partial \psi_1}{\partial \eta} = 0 \qquad \text{on} \qquad \eta = 0 \tag{3.15}$$

and

$$\psi_1 = -g(\xi_s') \frac{\partial \psi_o}{\partial \eta} = G(\xi_s') \qquad \text{on} \qquad \eta = a \ . \tag{3.16}$$

Boundary condition (3.12) has been expanded in a Taylor's series about $\eta = a$ and only terms accurate to the first order in the small quantities g and ψ_1 are retained to give Eq. (3.16). Recalling the physical interpretation of ψ, it will be noted that the value of ψ_1 on the boundary $\eta = a$ is $-1/\rho$ times the impulsive reaction per unit area due to the acceleration from rest to a speed $\partial \psi_o / \partial \eta$ of a column of fluid whose height is $g(\xi_s')$ and whose density is ρ.

The problem for ψ_1 may be made somewhat simpler by exploiting the even symmetry of the problem to note that the derivative

$\partial\psi_1/\partial\xi$ must vanish along $\xi = 0$, $0 < \eta < a$. The transformation

$$s = \sigma + i\tau = -\sinh\frac{\pi}{2a}(\zeta - ia) \tag{3.17}$$

will map the semi-infinite strip

$$\xi < 0 \quad , \quad 0 < \eta < a$$

onto the first quadrant in the s-plane with the boundaries transforming as shown in Fig. 6. Denoting the value of ψ_1 along $\sigma > 0$, $\tau = 0$ by $G(\sigma)$, then the continuation of $G(\sigma)$ into $\sigma < 0$ as an even function ensures that the boundary condition along $\sigma = 0$ will be satisfied.

Now the complex function, $F_1(s)$, analytic in the upper-half s-plane, whose real part is $G(\sigma)$ along the real axis is given by the well-known formula

$$F_1(s) = \frac{1}{\pi i}\int_{-\infty}^{\infty}\frac{G(\sigma')d\sigma'}{\sigma' - s} \quad .$$

See, for example, Ref. (21), p. 304. Thus the complex conjugate perturbation velocity is

$$F_1'(s) = \frac{\partial\psi_1}{\partial\sigma} - i\frac{\partial\psi_1}{\partial\tau} = \frac{1}{\pi i}\int_{-\infty}^{\infty}\frac{G(\sigma')d\sigma'}{(\sigma' - s)^2} \tag{3.18}$$

in the s-plane.

The function $G(\sigma')$ will now be calculated assuming $a \gg 1$. Substitution of $z = x + iy$ into the transformation (3.7) gives, after introduction of Eqs. (3.5) and (3.6)

$$\xi'_s = \sin\frac{\pi x}{2}\sqrt{1 + \frac{a^2}{\cos^2\frac{\pi x}{2}}}\cosh h(x) + a\tan\frac{\pi x}{2}\sinh h(x) \tag{3.19}$$

and

$$\eta'_s = a\cosh h(x) + \cos\frac{\pi x}{2}\sqrt{1 + \frac{a^2}{\cos^2\frac{\pi x}{2}}}\,\sinh h(x) \quad . \qquad (3.20)$$

The geometrical relationships prevailing between these quantities are shown in Fig. 7. In the case $a^2 \gg 1$, (3.19) and (3.20) become

$$\xi'_s = a\tan\frac{\pi x}{2}\, e^h \qquad (3.21)$$

and

$$\eta'_s = ae^h \qquad (3.22)$$

respectively. Evidently, then, $g(\xi'_s)$ is simply

$$g(\xi'_s) = a(e^h - 1) \qquad \text{when} \qquad a \gg 1 \quad . \qquad (3.23)$$

For the zeroth order solution, the choice

$$\psi_o(\xi, \eta) = \omega_{\frac{1}{2}}(\xi, \eta)$$

will be made. Hence, from Eq. (2.33),

$$\frac{\partial\psi_o}{\partial\eta}(\xi, a) = \frac{2}{\pi}\tan^{-1}\frac{\sinh\pi/2a}{\cosh\frac{\pi\xi}{2a}}$$

which becomes

$$\frac{\partial\psi_o}{\partial\eta}(\xi, a) = \frac{1}{a}\frac{1}{\cosh\frac{\pi\xi}{2a}} \qquad (3.24)$$

for large a. From Fig. 7 it is clear that ξ'_s is the value of ξ to be used in this equation. Thus, in terms of the variable x, the function G is

$$G(x) = -g(\xi'_s) \frac{\partial \psi_o}{\partial \eta} (\xi'_s, a)$$

$$= - \frac{e^h - 1}{\cosh \frac{\pi \xi'_s}{2a}} \tag{3.25}$$

where $\xi'_s(x)$ is given by Eq. (3.21).

The perturbation velocity at the point $s = 0$, corresponding to $z = id$ in the z-plane, will now be calculated. It is true, in general, that the principle value of the integral in Eq. (3.18) must be taken. For the special case to be considered, however, the function $G(\sigma)$ will have a second-order zero at $\sigma = 0$ so that the expression

$$\left. \frac{\partial \psi_1}{\partial \tau} \right|_{s=o} = \frac{2}{\pi} \int_o^\infty \frac{G(\sigma')}{\sigma'^2} \, d\sigma' \tag{3.26}$$

will converge in the Riemann sense near $\sigma' = 0$. The relation

$$\sigma' = - \sinh \frac{\pi \xi'_s}{2a} \tag{3.27}$$

follows from (3.17) with $\zeta = \xi'_s + ia$. Thus

$$d\sigma' = - \frac{\pi}{2a} \cosh \frac{\pi \xi'_s}{2a} \, d\xi'_s \tag{3.28}$$

where $d\xi'_s$ is

$$d\xi'_s = a e^h \left[h' \tan \frac{\pi x}{2} + \frac{\pi}{2} \frac{1}{\cos^2 \frac{\pi x}{2}} \right] dx \tag{3.29}$$

from Eq. (3.21). Substitution of (3.25), (3.27), (3.28), and (3.29) into (3.26) results in

$$\left.\frac{\partial \psi_1}{\partial \tau}\right|_{s=o} = -\int_o^1 \frac{e^h - 1}{\sinh^2 \frac{\pi \xi'_s}{2a}} e^h \left[h' \tan \frac{\pi x}{2} + \frac{\pi}{2} \frac{1}{\cos^2 \frac{\pi x}{2}} \right] dx \qquad (3.30)$$

where

$$\xi'_s = a \tan \frac{\pi x}{2} e^h \quad .$$

Finally, the perturbation velocity in the z-plane at the point $(0, d)$ is

$$\left.\frac{dF_1}{dz}\right|_{z=id} = \left.\frac{dF_1}{ds}\right|_{s=o} \times \left.\frac{ds}{d\zeta}\right|_{\zeta=ia} \times \left.\frac{d\zeta}{dz}\right|_{z=id}$$

so that

$$\left.\frac{\partial \psi_1}{\partial y}\right|_{(o,d)} = -\frac{\pi^2}{4} \left.\frac{\partial \psi_1}{\partial \tau}\right|_{(o,o)} \quad . \qquad (3.31)$$

The choice of y'_s will be based on experiments performed on bubbles rising in slender circular tubes, see for example Ref. (22), and Ref. (23), p. 235. These indicate that the liquid film thickness along the tube wall varies as $\frac{1}{\sqrt{z}}$ where z is the axial coordinate. This manner of variation can be found analytically through application of the Bernoulli and continuity equations to the liquid film. It is easy to show that the film thickness corresponding to the free surface shape, y_s, used in the two-dimensional problem of Section 2 varies as e^{-y}. In addition, the nose radius of these bubbles is about 0.70 tube radii -- somewhat larger than the value $\frac{2}{\pi} \simeq 0.637$ found in the limiting case $a \gg 1$ of the two-dimensional theory.

One is thus led to assume that

$$y'_s = b\,\frac{\pi}{2}\left[\frac{1}{\sqrt{1-x^2}} - 1\right] + d \tag{3.32}$$

where b is a constant. If $b = 1$, the radii of curvature of y'_s and y_s agree at $x = 0$; while if $b = 0.910$, the radius of curvature of y'_s is 0.700 at $x = 0$. Equation (3.32) is plotted for these values of b in Fig. 8. Also shown is a typical experimental free surface. It is, of course, axially symmetric; however, Eq. (3.32) with $b = 0.910$ is a rather good approximation.

In view of Eqs. (2.7) and (3.6), the perturbation $h(x)$ is

$$h(x) = b\,\frac{\pi}{2}\left[\frac{1}{\sqrt{1-x^2}} - 1\right] + \log\cos\frac{\pi x}{2} \quad . \tag{3.33}$$

Substitution of this into Eq. (3.30) gives, after numerical integration and use of (3.31),

$$\left.\frac{\partial \psi_1}{\partial y}\right|_{(o,d)} = 0.01271 \tag{3.34}$$

when

$$b = 1$$

and

$$\left.\frac{\partial \psi_1}{\partial y}\right|_{(o,d)} = -0.01232 \tag{3.35}$$

when

$$b = 0.910 \quad .$$

Recalling that the case $b = 1$ corresponds only to a perturbation in the free surface shape near the channel walls, it is clear from result (3.34) that the velocity at the midpoint of the free surface is not much affected by such changes. The perturbation velocity there is

only 0.8% of the zeroth order value, $\frac{\pi}{2}$. The decrease in the perturbation velocity when $b = 0.910$ is mainly a consequence of the decrease in the nose radius. In any event, the effects of changes in the free surface shape near the channel walls are negligible in two-dimensions.

Finally, a few remarks seem in order with respect to the validity of this perturbation analysis. Reference is made specifically to the assumptions regarding the smallness of the quantity $h(x)$ and its counterpart in the ζ-plane, $g(\xi'_s)$. It is clear from Eqs. (3.33) and (3.23) that neither is very small for x near ± 1 and ξ'_s large. More fundamental, however, is the assumption that $\psi(\xi'_s; \eta'_s)$ can be approximated by $\psi_1(\xi'_s, a) + g(\xi'_s) \frac{\partial \psi_o}{\partial \eta} (\xi'_s, a)$ (see Eq. (3.16)ff.). This is a rather close approximation; for in the portion of the ζ-plane where g is large, the quantity $\frac{\partial \psi_o}{\partial \eta}$ is quite small. The behavior of the term $g \frac{\partial \psi_o}{\partial \eta}$ can, in fact, be shown from Eqs. (3.21) and (3.25) to be

$$\exp - \frac{e^h}{1-x}$$

near

$$x = 1 \quad .$$

4. The Case of a Nearly Planar Free Surface

Although experimental results will be discussed in detail further on, the major one will be mentioned here in order to motivate the analysis which follows. It has been found experimentally that, in three dimensions, the ratio between the initial velocity at the midpoint of the

free surface and the initial mean velocity imparted to the fluid column is much closer to three than to $\pi/2$. The development in this section suggests that the difference, in part, is attributable to the three-dimensional character of the experimental flow.

Consider a column of liquid accelerated impulsively from below such as that shown in the sketch. The coordinates are (x, y) in two-dimensions and (r, z) in three.

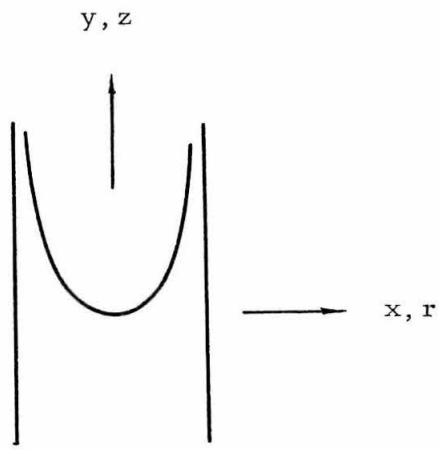

Assume, however, that the free surface very nearly coincides with the plane y (or z) $= 0$; specifically, that the initial free surface height is given by $y = \epsilon f(x)$ in two dimensions and by $z = \delta g(r)$ in the case of axial symmetry, where $\epsilon, \delta \ll 1$.

In the interests of simplicity, the choices

$$\epsilon f(x) = \epsilon[1 - \cos \pi x] \tag{4.1}$$

and

$$\delta g(r) = \delta[1 - J_0(k_1 r)] \tag{4.2}$$

will be made, where $k_1 \tilde{=} 3.832$ is the first positive root of $J_1(k) = 0$.

Further, since the curvature at the origin is

$$\frac{1}{R} = \epsilon f''(o) = \epsilon\pi^2 \qquad \text{from Eq. (4.1)} \tag{4.3}$$

and

$$\frac{1}{R} = \delta g''(o) = \frac{1}{2} k_1^2 \delta \qquad \text{from (4.2)} \quad ; \tag{4.4}$$

the values

$$\epsilon = \frac{1}{2\pi} \simeq 0.1592$$

and

$$\delta = \frac{\pi}{k_1^2} \simeq 0.2140$$

ensure that the radius of curvature at the origin is $2/\pi$, in conformity with that in the limiting case $a \gg 1$ of the exact problem previously solved. The three free surface shapes are plotted together in Fig. 9.

If the column is given a unit impulsive velocity upward, then an impulse function, $\varphi'(x,y)$, may be defined in two-dimensions which solves the following problem:

$$\nabla^2\varphi' = 0 \qquad \text{in} \qquad y < \epsilon f(x) \quad , \quad |x| < 1 \tag{4.5}$$

$$\frac{\partial\varphi'}{\partial x} = 0 \qquad \text{on} \qquad x = \pm 1 \tag{4.6}$$

$$\frac{\partial\varphi'}{\partial y} \to 1 \qquad \text{as} \qquad y \to -\infty \tag{4.7}$$

and

$$\varphi'(x,y) = 0 \quad \text{on} \qquad y = \epsilon f(x) \tag{4.8}$$

Since $\epsilon \ll 1$, boundary condition (4.8) may be written approximately as

$$\varphi'(x,0) + \epsilon f \frac{\partial \varphi'}{\partial y}(x,0) + \frac{1}{2}\epsilon^2 f^2 \frac{\partial^2 \varphi'}{\partial y^2} = 0 \quad . \tag{4.9}$$

Further, if $\varphi'(x,y)$ is assumed to be of the form

$$\varphi'(x,y) = \varphi'_o(x,y) + \epsilon\varphi'_1(x,y) + \epsilon^2\varphi'_2(x,y) + \ldots \tag{4.10}$$

then the system consisting of Eqs. (4.5) through (4.9) becomes (substituting Eq. (4.10) and equating powers of ϵ)

$$\nabla^2\varphi'_o = \nabla^2\varphi'_1 = \nabla^2\varphi'_2 = 0 \quad , \tag{4.11}$$

$$\frac{\partial \varphi'_o}{\partial x} = \frac{\partial \varphi'_1}{\partial x} = \frac{\partial \varphi'_2}{\partial x} = 0 \qquad \text{on} \qquad x = \pm 1 \quad , \tag{4.12}$$

$$\frac{\partial \varphi'_o}{\partial y} \to 1 \qquad \text{as} \qquad y \to -\infty \quad , \tag{4.13}$$

$$\frac{\partial \varphi'_1}{\partial y} = \frac{\partial \varphi'_2}{\partial y} = 0 \qquad \text{as} \qquad y \to -\infty \quad , \tag{4.14}$$

$$\varphi'_o(x,0) = 0 \quad , \tag{4.15}$$

$$\varphi'_1(x,0) = -f(x)\frac{\partial \varphi'_o}{\partial y}(x,0) \quad , \tag{4.16}$$

and

$$\varphi'_2(x,0) = -f(x)\frac{\partial \varphi'_1}{\partial y}(x,0) \quad . \tag{4.17}$$

Consideration of Eqs. (4.11), (4.12), (4.13), and (4.15) leads immediately to

$$\varphi'_o(x,y) = y \tag{4.18}$$

which, when used in (4.16), gives

$$\varphi'_1(x,0) = -f(x) \tag{4.19}$$

for the boundary condition on φ'_1. Recalling that $-\epsilon\rho\varphi'_1$ represents an impulse per unit area, say I'_1, Eq. (4.19) may be written

$$I'_1 = \rho\epsilon f(x)$$

which is just the impulsive reaction per unit area along the plane $y = 0$ which would be calculated from Newton's second law assuming that a rigid column of height $\epsilon f(x)$ and density ρ were suddenly given a unit velocity upward.

Using

$$f(x) = 1 - \cos \pi x$$

in Eq. (4.19), one has

$$\varphi'_1(x, y) = -(1 - \cos \pi x\, e^{\pi y}) \qquad (4.20)$$

so that Eq. (4.17) becomes

$$\varphi'_2(x, 0) = \frac{1}{2}\pi\left[\cos 2\pi x - 2\cos \pi x + 1\right] .$$

Thus the second order solution is

$$\varphi'_2(x, y) = \frac{1}{2}\pi\left[\cos 2\pi x e^{2\pi y} - 2\cos \pi x e^{\pi y} + 1\right] . \qquad (4.21)$$

Discussion of these results will be deferred pending consideration of the analogous problem in three dimensions.

If, in three dimensions, the free surface height and the corresponding impulse function are $\delta g(r)$ and $\chi'(r, z)$, respectively, then the transformations

$$\epsilon \rightarrow \delta \quad , \qquad \varphi'_n \rightarrow \chi'_n \quad ,$$

$$x \rightarrow r \quad , \qquad f \rightarrow g$$

and $y \rightarrow z$,

applied to Eqs. (4.11) through (4.17) give the relevant equations in the case of axial symmetry. The zeroth order solution is readily found to be

$$\chi'_o(r,z) = z \tag{4.22}$$

which, upon substitution into the analog of Eq. (4.16), gives

$$\chi'_1(r,0) = -g(r) \quad . \tag{4.23}$$

Comparison of this with the corresponding result in two dimensions (Eq. (4.19)) shows that, to this order, there is no difference in the impulse distribution caused by the change from two dimensions to three.

Use of the specific expression for $g(r)$ in (4.23), yields

$$\chi'_1(r,z) = J_o(k_1 r)e^{k_1 z} - 1 \quad , \tag{4.24}$$

so that the boundary condition for the second order solution takes the form

$$\chi'_2(r,0) = k_1 J_o^2(k_1 r) - k_1 J_o(k_1 r) \quad . \tag{4.25}$$

Now an harmonic function which satisfies the boundary conditions on $r = 1$ and $z = -\infty$ is

$$\chi'_2(r,z) = k_1 a_o + k_1 \sum_{n=1}^{\infty} a_n J_o(k_n r)e^{k_n z} - k_1 J_o(k_1 r)e^{k_1 z} \quad , \tag{4.26}$$

If the coefficients a_n are chosen by

$$a_n = \frac{2}{J_o^2(k_n)} \int_o^1 r J_o^2(k_1 r) J_o(k_n r) dr \quad , \tag{4.27}$$

then boundary condition (4.25) will also be satisfied. (See Ref. (24), p. 596 or Ref. (25), p. 228).

For $k_n = 0$, Eq. (4.27) may be integrated directly (see Ref. (24), p. 135) to give

$$a_o = J_o^2(k_1) \tilde{=} 0.1622$$

while, for $1 \leqslant n \leqslant 14$, numerical integration results in

$$a_1 = 0.3523$$

$$a_2 = 0.4793$$

$$a_3 = 0.006881$$

and $a_n < 10^{-3}$ for $4 \leqslant n \leqslant 14$; a_{14}, for example, is 6.6×10^{-7}. A rather close approximation, then, involves use of only the first three terms:

$$\chi'_2(r,z) = k_1 [a_2 J_o(k_2 r) e^{k_2 z} - (1-a_1) J_o(k_1 r) e^{k_1 z} + a_o] \tag{4.28}$$

where

$$k_2 \tilde{=} 7.0156 \quad .$$

These approximate results will now be compared with each other and with the exact two-dimensional solution found in Section 2. Recall that the quantities $-\varphi'(x,0)$ and $-\chi'(r,0)$ represent the impulse per unit area, normalized by the fluid density, acting across the plane y (or z) = 0. These, correct to $O(\epsilon^2, \delta^2)$, are given by

$$-\varphi'(x,0) = -\epsilon\varphi_1'(x,0) - \epsilon^2\varphi_2'(x,0) \qquad (4.29)$$

and

$$-\chi'(r,0) = -\delta\chi_1'(r,0) - \delta^2\chi_2'(r,0) \quad . \qquad (4.30)$$

They are shown in Fig.10(a) for the values of ϵ and δ previously chosen. In addition, the polynomial approximation found in Section 2 for $-\omega_o(x,d)$ is shown on the same co-ordinates. This quantity is exact in the sense that no approximations with respect to the smallness of the free surface height were made in obtaining it.

An immediate conclusion from Fig.10(a) is that the two-dimensional perturbation solution is very close to the exact solution out to nearly half the channel half-width. In addition to lending credibility to the approximate solution, this fact suggests that the three dimensional approximate solution may also be fairly accurate near the origin. The decrease in $-\varphi'$ and $-\chi'$ beyond $x, r \tilde{=} 0.7$ is certainly a consequence of the approximations made in obtaining the perturbation solutions, for the exact two dimensional solution shows no such decrease.

Evidently, the impulse calculated in three dimensions is uniformly larger than that in two dimensions - - a notion made more specific by Fig.10(b) wherein the ratio $\chi'(r,0)/\varphi'(x,0)$ is plotted. Near the origin where the perturbation solutions are apt to be valid, the ratio is close to 1.21. It is of interest to note, however, that the ratio is roughly constant over the entire column even though the three-dimensional free surface height at $r = 1$ is some 6% less than the two-dimensional free surface height at $x = 1$. (See Fig. 9).

The velocity at the origin may be calculated in two-dimensions from Eqs. (4.18), (4.20), and (4.21):

$$\frac{\partial \varphi'}{\partial y}(0,0) = 1 + \epsilon\pi + O(\epsilon^3) \tag{4.31}$$

while from Eqs. (4.22), (4.24) and (4.28):

$$\frac{\partial \chi'}{\partial z}(0,0) = 1 + \delta k_1 + \delta^2[k_1 k_2 a_2 - k_1^2(1-a_1)] + O(\delta^3) \tag{4.32}$$

It is more instructive, however, to write these in terms of the radius of curvature, R, of the initial free surface at the origin. Thus

$$\frac{\partial \varphi'}{\partial y}(0,0) = 1 + \frac{1}{\pi R} + O(\epsilon^3) \tag{4.33}$$

and

$$\frac{\partial \chi'}{\partial z}(0,0) = 1 + \frac{2}{k_1 R} + \frac{4}{k_1^2 R^2}\left[\frac{k_2}{k_1} a_2 - (1-a_1)\right] + O(\delta^3) \quad . \tag{4.34}$$

If R is chosen to be $\frac{2}{\pi}$ for comparison with the exact two-dimensional solution, there results

$$\frac{\partial \varphi'}{\partial y}(0,0) = \frac{3}{2} \quad .$$

This should be compared to the value $\pi/2$ of the exact solution. The axially-symmetric problem gives

$$\frac{\partial \chi'}{\partial z}(0,0) \tilde{=} 1.974$$

when $R = \frac{2}{\pi}$.

In the general case, the initial free surface height can be

written

$$\epsilon f(r) = \sum_{1} A_n [\cos n\pi x - 1] \tag{4.35}$$

in two dimensions, and

$$\delta g(r) = \sum_{1} B_n [J_o(k_m r) - 1] \tag{4.36}$$

in three. The results corresponding to (4.31) and (4.32) are easily shown to be

$$\varphi'_y(0,0) = 1 + \sum_{1} n\pi A_n \tag{4.37}$$

and

$$\chi'_z(0,0) = 1 + \sum_{1} k_m B_m \tag{4.38}$$

correct to the first order in the small quantities A_n and B_m. If the free surface heights ϵf and δg are the same, it follows from (4.35) and (4.36) that

$$\frac{1}{R} = \sum_{1} n^2\pi^2 A_n = \frac{1}{2} \sum_{1} k_m^2 B_m \quad .$$

Equations (4.37) and (4.38) may then be written

$$\varphi'_y(0,0) = 1 + \frac{\sum_{1} n\pi A_n}{\sum_{1} n^2\pi^2 A_n} \frac{1}{R}$$

and

$$\chi_z'(0,0) = 1 + \frac{\sum_1 k_m B_m}{\sum_1 k_m^2 B_m} \frac{2}{R}$$

respectively. Hence, the midpoint velocity is related to the free surface curvature in a simple way only when $A_n = B_m = 0$ for all but a single m and n.

Finally, the upward velocities along y and z equal to zero are shown correct to the second order in Fig. 11. The two-dimensional velocity follows from Eqs. (4.18), (4.20), and (4.21), that for the axially-symmetric case was calculated from Eqs. (4.22), (4.24), and (4.28). The curves of Fig. 11 may be interpreted as representing the free surface shape for small time. Note that the two solutions approach one another as the distance from the origin is increased. This suggests that the three-dimensional flow may be approximately two-dimensional near the tube wall.

5. The Exact Solutions of Several Related Problems in Two and Three Dimensions

The exact two-dimensional analysis cannot be carried over into three dimensions; for the powerful tool of conformal mapping is no longer available and application of the boundary condition on the free surface becomes a difficult undertaking indeed.

In order to formulate a problem which can be solved in three dimensions, it is useful to consider a column of liquid (in either two dimensions or three) such as that shown in the sketch in Section 4. If an impulsive velocity upward is imparted to the column across some plane located in y(or z) < 0, a system of impulses must act across horizontal planes caused by the reaction of the fluid above the plane on that below. If this impulse distribution is denoted $I(x, y)$ in two dimensions, the relation between $I(x, y)$ and the impulse function $\omega(x, y)$ used in Section 2 is simply

$$I(x, y) = - \rho\omega(x, y)$$

from Eq. (1.7), with a similar relation in the case of axial symmetry. It is clear, then, that if this impulse were known along $y = 0$, the function $\omega(x, y)$ could be determined in $y < 0$ by solving a boundary-value problem of the sort discussed previously--greatly simplified, of course, in the absence of the free surface. The upward velocity at the midpoint of the free surface would then be the normal derivative of this function evaluated at the origin. Analysis along these lines will begin with a two-dimensional problem.

Representing the impulse function by $\varphi(x, y)$, the problem is

$$\nabla^2\varphi = 0 \qquad \text{in} \qquad y < 0 \ , \ |x| < 1 \tag{5.1}$$

$$\frac{\partial\varphi}{\partial x} = 0 \qquad \text{on} \qquad x = \pm 1 \tag{5.2}$$

$$\frac{\partial\varphi}{\partial y} \to 1 \qquad \text{as} \qquad y \to -\infty \tag{5.3}$$

and

$$\varphi \qquad \text{specified on} \qquad y = 0 \ . \tag{5.4}$$

This is analogous to the exact two-dimensional problem in the limit $a \gg 1$ since the column is assumed to extend to infinity.

It is convenient to assume

$$\varphi(x, y) = y + \varphi_m(x, y) \tag{5.5}$$

where $\varphi_m(x, y)$ describes the effects of an impulse distribution along $y = 0$ given by

$$\varphi_m(x, 0) = -x^m \ , \tag{5.6}$$

and

$$|\nabla\varphi_m| \to 0 \qquad \text{as} \qquad y \to -\infty \ . \tag{5.7}$$

Linearity then permits the construction of more general solutions through the use of superposition. The integer m will be assumed even in view of the symmetry of the problem. The solution of Eq. (5.1) which satisfies boundary conditions (5.2) and (5.7) is

$$\varphi_m(x, y) = \sum_{n=o}^{\infty} B_n(m) \cos n\pi x \, e^{n\pi y} \ . \tag{5.8}$$

Application of (5.6) gives B_n in the form

$$B_n(m) = -2 \int_o^1 x^m \cos n\pi x \, dx \ , \qquad m \text{ even} \ .$$

The details of the integration are left to Appendix C.

Turning now to the velocity at the origin, the expression

$$\frac{\partial \varphi_m}{\partial y}(0,0) = \varphi_{m,y}(0,0) = \sum_{n=1}^{\infty} n\pi B_n(m) \qquad (5.9)$$

follows from Eq. (5.8). The first five of these are, again for m even,

$$\begin{aligned} \varphi_{2,y}(0,0) &= 0.88254 \\ \varphi_{4,y}(0,0) &= 0.36943 \\ \varphi_{6,y}(0,0) &= 0.2437 \\ \varphi_{8,y}(0,0) &= 0.1836 \\ \varphi_{10,y}(0,0) &= 0.148 \quad . \end{aligned} \qquad (5.10)$$

Thus, if $\varphi(x,0)$ is given as a polynomial of the form

$$\varphi(x,0) = -\sum_{m=1}^{5} A_{2m} x^{2m} \quad , \qquad (5.11)$$

the resulting velocity at the origin is just

$$\frac{\partial \varphi}{\partial y}(0,0) = 1 + \sum_{m=1}^{5} A_{2m} \varphi_{2m,y}(0,0) \quad . \qquad (5.12)$$

For example, use of the coefficients A_{2m} corresponding to the impulse found to be acting in the exact two-dimensional case (Eq.(2.31)) results in

$$\frac{\partial \varphi}{\partial y}(0,0) = 1.560 \cong 0.993\ \pi/2$$

- a difference of 0.7% with respect to the exact result.

The three-dimensional analog to this problem will now be solved. If χ_m denotes the analog of φ_m, then it must satisfy

$$\nabla^2 \chi_m = 0 \qquad \text{in} \qquad z < 0 \ , \quad r < 1 \tag{5.13}$$

$$\frac{\partial \chi_m}{\partial r} = 0 \qquad \text{on} \qquad r = 1 \tag{5.14}$$

$$|\nabla \chi_m| \to 0 \qquad \text{as} \qquad z \to -\infty \tag{5.15}$$

and

$$\chi_m = - r^m \qquad \text{on} \qquad z = 0 \ . \tag{5.16}$$

The counterpart of Eq. (5.5) is

$$\chi(r,z) = z + \chi_m(r,z) \ . \tag{5.17}$$

The solution of Eq. (5.13) which satisfies boundary conditions (5.14) and (5.15) is

$$\chi_m(r,z) = \sum_{n=1}^{\infty} C_n(m) J_o(k_n r) e^{k_n z} \tag{5.18}$$

where k_n is the n^{th} positive root of

$$J_o'(k) = 0 \ .$$

The requirement that χ_m satisfy boundary condition (5.16) results in

$$C_n(m) = - \frac{2}{J_o^2(k_n)} \int_o^1 r^{m+1} J_o(k_n r) dr \tag{5.19}$$

which is evaluated in Appendix D.

Differentiation of (5.18) with respect to z yields the velocity

at the origin in the form

$$\frac{\partial \chi_m}{\partial z}(0,0) = \chi_{m,z}(0,0) = \sum_{n=1}^{\infty} k_n C_n(m) \quad . \tag{5.20}$$

Evaluation of this for the first five even values of m gives

$$\begin{aligned} \chi_{2,z}(0,0) &= 1.5392 \\ \chi_{4,z}(0,0) &= 0.70714 \\ \chi_{6,z}(0,0) &= 0.4876 \\ \chi_{8,z}(0,0) &= 0.3777 \\ \chi_{10,z}(0,0) &= 0.311 \end{aligned} \tag{5.21}$$

Thus, if $\chi(r,0)$ is known in terms of a polynomial approximation

$$\chi(r,0) = -\sum_{m=1}^{5} D_{2m} r^{2m} \quad , \tag{5.22}$$

then the velocity at the origin is given by

$$\frac{\partial \chi}{\partial z}(0,0) = 1 + \sum_{m=1}^{5} D_{2m} \chi_{2m,z}(0,0) \quad . \tag{5.23}$$

The question now, of course, is the value of D_{2m}. Alternatively, one may seek the amount and character of the difference between the impulse per unit area, $-\rho\varphi(x,0)$, acting in two dimensions and the analogous quantity, $-\rho\chi(r,0)$, in three. Some guidance in this matter can be had through consideration of the perturbation problem of Section 4.

In view of the results of that analysis, the approximation chosen

is

$$\chi(r, 0) = 1.21\ \omega_o(r, d)$$

where $\omega_o(r, d)$ is the impulse function found for the two-dimensional exact solution of Section 2 with x replaced by r. Since a polynomial approximation to this function is known in the form

$$\omega_o(r, d) = -\sum_{1}^{5} A_{2m} r^{2m}$$

where the A_{2m}'s are given in Eq. (2.31), the D_{2m}'s of Eq. (5.22) are simply

$$D_{2m} = 1.21\ A_{2m} \quad .$$

Substitution of these, together with $\chi_{2m,z}(0, 0)$ from Eq. (5.21), in Eq. (5.23) gives

$$\frac{\partial \chi}{\partial z}(0, 0) = 1 + (1.21)(0.9259) = 2.12 \quad ; \qquad (5.24)$$

an increase of 36% over the corresponding result in two dimensions. Note that a portion of the increase is due solely to the fact that the response at the origin to a given impulse is greater in three-dimensions than in two, i.e. $\chi_{2m,z}(0, 0) > \varphi_{2m,y}(0, 0)$, while the remainder is due to the increase of the impulse: $|D_{2m}| > |A_{2m}|$.

6. The Effect of Finite Column Length

It has been found in Section 2 that the flow produced in a column of fluid by a non-uniform velocity applied impulsively at one end will, in general, depend upon the column length. Specifically, the analysis shows that non-uniformities in the applied velocity may be important

when the column length is less than half its width. The results of Section 2 are of little value for columns shorter than this, however, because of the dependence of the initial free surface curvature, $1/R$ upon the column length, d, (see Eq. (2.6') and Fig. 3).

The phenomena peculiar to short fluid columns will be examined using the axially-symmetric perturbation model of Section 4. Suppose that the initial free surface shape is given by

$$\delta g(r) = \delta[\,1 - J_o(k_1 r)] \quad , \tag{6.1}$$

where $\delta \ll 1$ as before, and that a non-uniform velocity, $1 + u_o(r)$, is applied impulsively across the plane $z = -d$. If $\Omega(r, z)$ denotes the resulting impulse function, then it must satisfy

$$\nabla^2\Omega = 0 \qquad \text{in} \qquad r < 1 \quad , \quad -d < z < \delta g(r) \quad , \tag{6.2}$$

$$\Omega_r = 0 \qquad \text{on} \qquad r = 1 \quad , \tag{6.3}$$

$$\Omega = 0 \qquad \text{on} \qquad z = \delta g(r) \quad , \tag{6.4}$$

and

$$\Omega_z = 1 + u_o(r) \qquad \text{on} \qquad z = -d \tag{6.5}$$

where the subscripts denote partial differentiations.

The solution of this system will be assumed to have the form

$$\Omega(r,z) = z + \Omega_o(r, z) + \delta\Omega_1(r,z) \tag{6.6}$$

where Ω_o represents the flow produced by the non-uniform velocity at $z = -d$ and $\delta\Omega_1$ is a small perturbation due to the non-planar free surface. Substituting (6.6) into (6.2) through (6.5) and equating powers

of δ results in the following system to be satisfied by Ω_o and Ω_1:

$$\nabla^2\Omega_o = 0 \qquad \text{in} \qquad r < 1\ , \quad -d < z < 0\ ,$$

$$\Omega_{o,r} = 0 \qquad \text{on} \qquad r = 1\ , \tag{6.7}$$

$$\Omega_o = 0 \qquad \text{on} \qquad z = 0\ , \tag{6.8}$$

$$\Omega_{o,z} = u_o(r) \qquad \text{on} \qquad z = -d\ , \tag{6.9}$$

$$\nabla^2\Omega_1 = 0 \qquad \text{in} \qquad r < 1\ , \quad -d < z < 0\ ,$$

$$\Omega_{1,r} = 0 \qquad \text{on} \qquad r = 1\ , \tag{6.10}$$

$$\Omega_1 = -g(r)[1+\Omega_{o,z}] \qquad \text{on} \qquad z = 0\ , \tag{6.11}$$

and

$$\Omega_{1,z} = 0 \qquad \text{on} \qquad z = -d\ . \tag{6.12}$$

As in Section 4, the free surface boundary condition (6.4), has been expanded about $z = 0$ to give Eqs. (6.8) and (6.11). Finally, it will prove convenient to write

$$u_o(r) = \sum_{n=1}^{\infty} D_n J_o(k_n r) \tag{6.13}$$

where the k_n's are the roots of

$$J_o'(k) = 0\ .$$

In view of (6.13), the harmonic function satisfying (6.7), (6.8), and (6.9) is

$$\Omega_o(r,z) = \sum_{n=1}^{\infty} D_n \frac{\sinh k_n z}{k_n \cosh k_n z} J_o(k_n r)\ . \tag{6.14}$$

Using this and (6.1) in (6.11) gives

$$\Omega_1(r,0) = [J_o(k_1 r)-1]\left[1+\sum_{n=1}^{\infty} \frac{D_n}{\cosh k_n d} J_o(k_n r)\right] \quad . \tag{6.15}$$

Now for all but the smallest values of d, the series in Eq. (6.15) will be dominated by its first term. For example, if d is one-half the radius of the cylinder, the series begins with

$$\Omega_{o,z} = \frac{D_1}{3.48} J_o(k_1 r) + \frac{D_2}{16.58} J_o(k_2 r) + \ldots .$$

Thus

$$\Omega_1(r,0) \simeq J_o(k_1 r) + D_1 \operatorname{sech} k_1 d[a_2 J_o(k_2 r) - (1-a_1)J_o(k_1 r)] \quad ,$$

where the additive constants have been dropped and the approximation

$$J_o^2(k_1 r) = a_o + a_1 J_o(k_1 r) + a_2 J_o(k_2 r)$$

with

$$a_1 = 0.3523$$

$$a_2 = 0.4793$$

has been used (see Eq. (4.27) ff.). Invoking boundary condition (6.12), it is clear that

$$\Omega_1(r,z) \simeq \frac{\cosh k_1(z+d)}{\cosh k_1 d} J_o(k_1 r)$$
$$+ D_1 \operatorname{sech} k_1 d\left[a_2 \frac{\cosh k_2(z+d)}{\cosh k_2 d} J_o(k_2 r) - (1-a_1) \frac{\cosh k_1(z+d)}{\cosh k_1 d} J_o(k_1 r)\right] \tag{6.16}$$

where the sign of approximate equality indicates that terms of the order $D_2 \operatorname{sech} k_2 d$ have been neglected in comparison to $D_1 \operatorname{sech} k_1 d$.

Solving for the upward velocity at the midpoint of the free surface from (6.6), (6.14), and (6.16):

$$\Omega_z(0,0) = 1 + \frac{2}{k_1 R} \tanh k_1 d$$

$$+ D_1 \operatorname{sech} k_1 d \left[1 + \frac{2}{k_1 R} \left(a_2 \frac{k_2}{k_1} \tanh k_2 d - (1-a_1) \tanh k_1 d \right) \right] \qquad (6.17)$$

where the relation

$$\delta = \frac{2}{k_1^2 R}$$

from Eq. (4.4) has been used. Note that in the limit $d \to \infty$,

$$\Omega_z(0,0) = 1 + \frac{2}{k_1 R}$$

in agreement, to the first order, with Eq. (4.34).

The results of this section are summarized in Fig. 12 where $\Omega_z(0,0)$ from Eq. (6.17) is plotted against d for $R = 2/\pi$ and several values of D_1. Figure 12 may be compared to Fig. 4 where the mid-point velocity is shown for the exact two-dimensional solution. The axially-symmetric solution for $D_1 = 0$ (uniform applied velocity) reaches its asymptotic value at $d \simeq 0.6$. This does not occur in the two-dimensional case $n = 0$ until $a \simeq 3$, corresponding to $d \simeq 1.12$ and $R \simeq 1.05 \frac{2}{\pi}$. The approximations made in obtaining (6.17) are equivalent to assuming that

$$u_o(r) = D_1 J_o(k_1 r)$$

so at the tube centerline, the impressed velocity exceeds the mean value by the factor $(1+D_1)$. The curve for $D_1 = 0.571 \simeq \pi/2 - 1$ thus

corresponds to the case $n = 1/2$ in Fig. 4 for which the impressed velocity is $\frac{\pi}{2} \cos \frac{\pi x}{2}$. The peaks occur at $d \simeq 0.19$ and $d \simeq 0.24$ in two and three-dimensions, respectively; however, the radius of curvature in two-dimensions is $1.94 \frac{2}{\pi}$ or almost double the value used in the axially-symmetric solution.

The existence of a peak in the velocity as the column length increases from zero is a consequence of the non-uniformity in the applied velocity interacting with the free surface curvature to produce a velocity at the origin greater than either could produce alone.

7. A Solution Valid for Finite Time

The previous analysis has been concerned with the flow in a suddenly accelerated body of liquid just after the start of motion. The evolution of this motion for a short time after its impulsive start will now be taken up. The solutions previously studied are in this case just initial values.

It will be convenient to deal with the velocity potential $\varphi(x, y, t)$ in two dimensions. The problem to be solved will be that of liquid confined between rigid walls, extending to negative infinity with a free surface in the finite part of the xy-plane. If the free surface height is taken to be $y = \eta(x, t)$, then the problem for φ and η is given by

$$\nabla^2 \varphi = 0 \qquad \text{in} \qquad y < \eta \quad , \quad |x| < 1 \qquad (7.1)$$

$$\varphi_x = 0 \qquad \text{on} \qquad x = \pm 1 \qquad (7.2)$$

and

$$\varphi_y \to 1 \qquad \text{as} \qquad y \to -\infty \quad . \tag{7.3}$$

In addition, the requirement that the pressure vanishes on the free surface leads to

$$\varphi_t + \frac{1}{2}(\varphi_x^2 + \varphi_y^2) = F(t) \qquad \text{on} \qquad y = \eta(x,t) \tag{7.4}$$

where $F(t)$ is an arbitrary function of the time. The kinematic boundary condition,

$$\frac{D}{Dt}(\eta - y) = 0$$

on the free surface, reads

$$\eta_t = \varphi_y - \varphi_x \eta_x \qquad \text{on} \qquad y = \eta(x,t) \quad . \tag{7.5}$$

Finally, initial values

$$\eta(x, 0^+) = \eta_o(x)$$

and

$$\nabla\varphi(x, y, 0^+) = \nabla\varphi_o(x, y)$$

must be specified.

In view of the nonlinear character of Eqs. (7.4) and (7.5), approximations with respect to the free surface height will be made in order to obtain a solution. It will be assumed that the free surface is very nearly planar and that, for small time, its shape may be approximated by

$$\eta(x,t) = \eta_o(x) + t[1 + \eta_1(x)] + t^2\eta_2(x) \tag{7.6}$$

where η_o, η_1 and η_2 are characterized by some parameter $\epsilon \ll 1$. This assumption permits any quantity, $f(x, y, t)$, to be evaluated on

$y = \eta(x,t)$ by means of the approximation

$$f(x,\eta,t) \simeq f(x,0,t) + \eta(x,t)\,\frac{\partial f}{\partial y}\,(x,0,t) \quad . \tag{7.8}$$

It will also be assumed that the potential, φ , may be expressed in the form

$$\varphi(x,y,t) = y + \varphi_o(x,y) + t\varphi_1(x,y) \quad , \tag{7.9}$$

valid for small time, where φ_o and φ_1 are small in a sense to be defined below.

Substitution of Eqs. (7.6) and (7.9) into the set (7.1) through (7.4) and use of approximation (7.8) results in the following system correct to the second order in the small quantities φ_o, φ_1 and η_o:

$$\nabla^2\varphi_1 = 0 \tag{7.10}$$

$$\varphi_{1,x} = 0 \qquad \text{on} \qquad x = \pm 1 \tag{7.11}$$

$$\varphi_{1,y} \to 0 \qquad \text{as} \qquad y \to -\infty \tag{7.12}$$

and

$$\varphi_1 + \eta_o\varphi_{1,y} + \frac{1}{2}\,\varphi_{o,x}^2 + \frac{1}{2}\,\varphi_{o,y}^2 + \varphi_{o,y} + \eta_o\varphi_{o,yy} = 0 \quad \text{on} \quad y = 0 \quad . \tag{7.13}$$

The fact that the flow at infinity is independent of time has been used to eliminate $F(t)$. The free surface height follows from (7.5) in the form

$$\eta_1 = \varphi_{o,y} + \eta_o\varphi_{o,yy} - \eta_{o,x}\varphi_{o,x} \qquad \text{on} \qquad y = 0 \tag{7.14}$$

and

$$\eta_2 = \frac{1}{2}\left[\varphi_{1,y} + \varphi_{o,yy} + \eta_o\varphi_{1,yy} + \eta_1\varphi_{o,yy} - \eta_{o,x}\varphi_{1,x} - \eta_{o,x}\varphi_{o,xy} - \eta_{1,x}\varphi_{o,x} + \eta_o\varphi_{o,yyy}\right] \qquad \text{on } y = 0 \quad . \tag{7.15}$$

For simplicity, the initial values $\eta_o(x)$ and $\varphi_o(x,y)$ will be assumed to be those found in Section 4. Thus

$$\eta_o(x) = \epsilon f(x) \tag{7.16}$$

where $f(x) = 1 - \cos \pi x$ and $\epsilon \ll 1$. From Eqs. (4.10), (4.18), (4.20), and (4.21) it is clear that, with an obvious change in notation, φ_o may be written

$$\varphi_o(x,y) = \epsilon \varphi_o^{(1)}(x,y) + \epsilon^2 \varphi_o^{(2)}(x,y) \tag{7.17}$$

where

$$\varphi_o^{(1)}(x,y) = \cos \pi x \, e^{\pi y} - 1 \tag{7.18}$$

$$\varphi_o^{(2)}(x,y) = \frac{\pi}{2} \left[\cos 2\pi x \, e^{2\pi y} - 2 \cos \pi x \, e^{\pi y} + 1 \right] . \tag{7.19}$$

The first order correction to the free surface height follows readily from Eqs. (7.14), (7.16), and (7.17) as

$$\eta_1(x) = \epsilon \pi \cos \pi x + O(\epsilon^3) \tag{7.20}$$

so that

$$\eta(x,t) = \epsilon(1 - \cos \pi x) + t\left[1 + \epsilon \pi \cos \pi x\right] + O(t^2 \epsilon)$$

from Eq. (7.6). At the origin this becomes

$$\eta(0,t) = t(1 + \epsilon \pi) + O(t^2)$$

which is simply the upward velocity at the origin found in Section 4, Eq. (4.31), multiplied by the time.

A solution of the form

$$\varphi_1 = \epsilon\varphi_1^{(1)} + \epsilon^2\varphi_1^{(2)}$$

will now be sought. Using this and Eq. (7.16) in Eqs. (7.10) through (7.13) and equating coefficients of powers of ϵ gives

$$\nabla^2\varphi_1^{(1)} = \nabla^2\varphi_1^{(2)} = 0$$

$$\varphi_{1,x}^{(1)} = \varphi_{1,x}^{(2)} = 0 \qquad \text{on} \qquad x = \pm 1$$

$$\varphi_{1,y}^{(1)}\ ,\quad \varphi_{1,y}^{(2)} \to 0 \qquad \text{when} \qquad y \to -\infty$$

$$\varphi_1^{(1)} + \varphi_{o,y}^{(1)} = 0 \qquad \text{on} \qquad y = 0 \qquad (7.21)$$

and

$$\varphi_1^{(2)} + f\varphi_{1,y}^{(1)} + \frac{1}{2}\varphi_{o,x}^{(1)^2} + \frac{1}{2}\varphi_{o,y}^{(1)^2} + \varphi_{o,y}^{(2)} + f\varphi_{o,yy}^{(1)} = 0 \quad \text{on } y=0\ . \quad (7.22)$$

If Eq. (7.18) is used in (7.21), the solution for $\varphi_1^{(1)}$ is clearly

$$\varphi_1^{(1)} = -\pi\cos\pi x\, e^{\pi y}\ .$$

Substitution of this into (7.22) gives

$$\varphi_1^{(2)}(x,0) = -\pi^2\left[\frac{1}{2} + \cos 2\pi x - \cos\pi x\right]$$

so that

$$\varphi_1^{(2)}(x,y) = -\pi^2\left[\frac{1}{2} + \cos 2\pi x\, e^{2\pi y} - \cos\pi x\, e^{\pi y}\right]\ .$$

It follows, then, from (7.15) that the second order correction to the free surface height is

$$\eta_2 = \frac{1}{2}\pi^3\epsilon^2\cos 2\pi x\ .$$

Thus the free surface height at $x = 0$ is

$$\eta(0,t) = t(1+\epsilon\pi) + \frac{1}{2}\, t^2\epsilon^2\pi^3 + O(t^3\epsilon^3) \qquad (7.23)$$

from Eqs. (7.6) and (7.20).

It will be convenient to have an expression for the velocity of the free surface at its midpoint in terms of the displacement there. Inversion of Eq. (7.23) gives

$$t = \frac{\eta}{1+\epsilon\pi}$$

correct to the first order in η. The velocity, $\eta_t(0,t)$, then follows from (7.23) as

$$\eta_t(0,t) = 1 + \epsilon\pi + \epsilon^2\pi^3\eta + O(\epsilon^3\eta^2) \quad . \qquad (7.24)$$

In addition, the time-average velocity, $\overline{\eta}_t(0,t)$, is readily found to be

$$\overline{\eta}_t(0,t) = \frac{\eta}{t} = 1 + \epsilon\pi + \frac{1}{2}\,\epsilon^2\pi^3\eta + O(\epsilon^3\eta^2) \quad .$$

Writing $\epsilon\pi = \dfrac{1}{\pi^2 R} = \dfrac{1}{2\pi}$, these become

$$\eta_t = \frac{3}{2}\left[1 + \frac{\pi}{6}\,\eta\right]$$

and

$$\overline{\eta}_t = \frac{3}{2}\left[1 + \frac{\pi}{12}\,\eta\right]$$

respectively. The time-average velocity is the quantity of physical interest, for it is the result of the velocity calculated from the free surface displacement measured at two instants in time. As an example, if $\eta = 0.5$ (a free surface displacement of one-fourth the channel width) the mean velocity is increased by about 13% over its initial instantaneous value.

8. Effects Due to Compressibility

Application of even approximately impulsive forces to any real fluid will, in general, result in a system of pressure waves arising as a consequence of compressibility. The effects produced at a free surface by such waves will now be considered in the acoustic limit.

To fix ideas, consider an axially-symmetric column of liquid with a free surface having the shape shown in Fig. 13 and suppose an acoustic wave is incident upon the free surface from below. The hemispherical cap has radius R and the radius of the circular column will be taken as the unit of length.

Several results from the theory of acoustics will be needed. First, for an acoustic wave moving with speed c into fluid at rest, the result

$$v_o = \frac{p_o}{\rho c} \tag{8.1}$$

can be shown to hold. Here, v_o is the velocity behind the wave, p_o the pressure jump across it, and ρ is the fluid density. It can also be shown that an acoustic wave incident upon a plane free boundary will cause a jump in velocity there, v_s normal to the free surface, given by

$$v_s = \frac{2p_o}{\rho c} \cos \alpha \tag{8.2}$$

where α is the angle between the normal to the wave and the normal to the free surface.

For a curved free surface, assume that, locally, the flow is described by (8.2); then for the case in question, the velocity, v_n

along the free surface just after passage of the wave will be

$$v_n = \frac{2p_o}{\rho c} \cos\theta \tag{8.3}$$

where v_n is everywhere normal to the initial free surface and θ is the polar angle shown in Fig. 13. Note that no flow normal to the free surface will occur when the wave propagates parallel to the free boundary. This is a prediction of acoustic theory; however, it does not seem possible that a wave could propagate at all if it were required to travel parallel to a free surface. It should be borne in mind also that a complicated system of reflected waves will arise due to the curved free surface and that Eq. (8.3) neglects any effects due to this system.

Now suppose that subsequent to the passage of the wave, the flow is that of an incompressible fluid. Conservation of mass may then be expressed as

$$\int_S q_n dS = 0 \tag{8.4}$$

where S is a closed surface within the fluid and q_n the normal component of velocity at each point of S. Define the mean axial velocity, $\bar{v}$, by

$$\bar{v}A = \int_{S_\infty} q_n dS \tag{8.5}$$

where S_∞ is a surface far below the free surface in Fig. 13 and A is the column cross-sectional area. Applying Eq. (8.4) to a control volume formed of the column walls and the free surface, S_f, gives

$$\bar{v} = \frac{1}{A} \int_{S_f} v_n dS \quad . \tag{8.6}$$

Thus, if the column cross-section is circular and of unit radius, use of Eq. (8.3) results in

$$\bar{v} = \frac{4p_o R^2}{\rho c} \int_o^{\pi/2} \cos\theta \sin\theta \, d\theta = \frac{2p_o}{\rho c} R_o^2 \quad . \tag{8.7}$$

Appealing now to Eq. (8.2), the ratio of the velocity, v_c, at the mid-point of the free surface to the mean velocity defined in (8.7) is found to be

$$\frac{v_c}{\bar{v}} = \frac{1}{R^2} \tag{8.8}$$

or 2.04 if $R = 0.7$ tube radii and 2.47 if $R = 0.637$.

In the light of the analysis assuming complete incompressibility, it would seem that the velocity, $p_o/\rho c$, of the fluid behind the wave should be used as the reference value, $\bar{v}$, in computing the ratio $v_c/\bar{v}$. This is probably a better approximation to the "mean velocity imparted to the column" in the sense in which the phrase was applied to incompressible flow. Note that this would exactly double the ratios calculated above. The quantity $\bar{v}$ given by (8.6) is, however, more easily estimated experimentally. If the acoustic wave is assumed to travel past the hemispherical cap instantaneously then the expression

$$A\Delta t \bar{v} = \int_{S_f} v_n \Delta t \, dS$$

is merely the volume of fluid displaced at the free surface in a time

Δt measured from the instant the wave passes.

9. Summary of Theoretical Analysis

The most important results of the preceding analysis will now be collected and compared with one another. First, from the exact two-dimensional solution of Section 2, it has been found that when a liquid column having a rather special free surface shape is accelerated impulsively, the resulting jump in the velocity at the free surface midpoint is close to $\pi/2$ times the mean velocity imparted to the column. The jump in velocity on the free surface is everywhere normal to that surface and is given for a long column by Eq. (2.34) in the form

$$\frac{\partial \omega}{\partial n}^{\frac{1}{2}} = \frac{\pi}{2} \sec \frac{\pi x}{2} \operatorname{sech}\left(\frac{\pi}{2} \tan \frac{\pi x}{2}\right) \tag{9.1}$$

if Eq. (2.1) is used and the limit as $a \to \infty$ is taken. This formula permits the free surface shape a short time after the start of the motion to be found from

$$\Delta = \frac{\partial \omega}{\partial n}^{\frac{1}{2}} t + O(t^2)$$

where Δ is the displacement measured normal to the initial free surface and t is the time.

Evidence has been adduced to show that the fluid located near the walls of the channel has a negligible effect on the jump in velocity experienced near the middle of the free surface. The most convincing demonstration is that of Section 4 wherein a perturbation analysis was carried out based on the assumption that the free surface is

nearly planar. The jump in velocity at the midpoint of the free surface was found, in two-dimensions, to be only 4% less than that calculated from the exact analysis when the two free surfaces had the same curvature at the center of the channel. Figure 9 shows the free surfaces in the two cases to be vastly different near the channel walls. This insensitivity is also apparent from the results of Section 3. These show that the jump in the velocity at the free surface midpoint is changed a negligible amount when the manner in which the free surface height becomes infinite near the channel wall is changed.

In the case of very long fluid columns, evidence has been found to suggest a relationship between the two-dimensional results discussed above and the case of axial symmetry. Recall that the assumption of a nearly plane free surface led, in Section 4, to

$$\varphi'_y(0, 0) = 1 + \frac{1}{\pi R} \tag{9.2}$$

for the jump in velocity at the origin in two-dimensions, and to

$$\chi'_z(0, 0) = 1 + \frac{2}{k_1 R} \tag{9.3}$$

in three. R is the radius of curvature of the free surface at its midpoint and $k_1 = 3.832$ is the first positive root of $J_1(k) = 0$. Note that these are strictly valid only when the second term is small compared to unity; however, in two dimensions the expression has been shown to be quite close to the exact result when the second term is as large as one-half.

Since the column of liquid was assumed to have been given an upward speed of unity, it is clear that the second term in each of the equations above represents a sort of "amplification" due to the curvature of the free surface. It will be seen from (9.2) and (9.3) that this "amplification", $\frac{2}{k_1 R}$ in three dimensions, exceeds the analogous quantity, $\frac{1}{\pi R}$ in two dimensions, by the factor

$$\frac{2\pi}{k_1} = 1.640$$

for all values of R. Using results (4.33) and (4.34), which are correct to the second order in the small quantities $\frac{1}{\pi R}$ and $\frac{2}{k_1 R}$, gives

$$\frac{0.974}{1/2} = 1.95$$

for this factor when $R = 2/\pi$.

A similar comparison can be made between the quantities $\varphi_{2m,y}(0,0)$ and $\chi_{2m,z}(0,0)$ calculated in Section 5. From Eqs. (5.12) and (5.23), it is evident that these, too, represent an "amplification". In this case, however, the free surface shape is not necessarily the same in two and three dimensions. Rather, the impulse acting across the plane tangent to the free surface at its midpoint is assumed to have the same functional dpendence upon the horizontal coordinate. That is, $\varphi_{2m,y}(0,0)$ and $\chi_{2m,z}(0,0)$ represent the velocity induced at the origin by the non-uniform impulses x^{2m} and r^{2m}, respectively. The ratio

$$\beta_{2m} = \frac{\chi_{2m,z}(0,0)}{\varphi_{2m,y}(0,0)}$$

is a measure, then, of the effectiveness of a given impulse in

accelerating the fluid at the free surface midpoint in three dimensions as compared to two. The table below shows the first five β_{2m}'s calculated from the results of Section 5.

m	β_{2m}
1	1.744
2	1.914
3	2.000
4	2.057
5	2.10

Evidently, an impulse r^{2m} in three dimensions leads to a velocity about double that produced by an impulse x^{2m} in two dimensions. This compares favorably with the value 1.95 found above from the second order perturbation analysis based on the assumption that the free surfaces have the same curvature at their midpoints.

Summarizing the results for long, axially-symmetric columns, the first order perturbation of Section 4 predicts an upward velocity equal to 1.82 times the mean velocity imparted to the column, while the solution correct to the second order gives 1.97. The independent calculation of Section 5, in which the impulse found to be acting in the exact two-dimensional case was applied without change to the axially-symmetric problem, gives 1.926. If the impulse is increased by 21% as suggested by the results of the perturbation analysis, the midpoint velocity is found to be 2.12 times the mean velocity (see Eq. (5.24)).

The effects of a non-uniform velocity applied to a circular liquid column are shown in Section 6 to be important at the free surface only when the column length is less than its radius. For very short columns, however, the interaction between a curved free surface and non-uniformities in the applied velocity can lead to velocities at the free surface midpoint much higher than one might expect intuitively, see Fig. 12 . This also indicates that the free surface shape at points remote from its midpoint is not important in determining the magnitude of the jump in velocity there. The greatest interaction occurs when $d \simeq 0.2$ - - corresponding to a column whose diameter is ten times its length. In these circumstances, it seems unlikely that the free surface shape near the cylinder walls could have any significant effect on the velocity near the center; the free surface curvature, however, has pronounced effects.

The solution of Section 7, valid for finite (but still small) time and a nearly planar free surface, shows that in two dimensions the midpoint velocity increases only slightly as the free surface moves away from its initial position. Writing $\epsilon = \frac{1}{\pi^2 R}$, the result from Eq. (7.24) is

$$\frac{\partial \eta}{\partial t}\,(0,t) = 1 + \frac{1}{\pi R} + \frac{1}{\pi R^2}\,\eta(0,t)$$

where $\eta(0,t)$ is the displacement of the free surface midpoint measured with respect to the origin. Hence, when this point is displaced half the channel half-width ($\eta = 0.5$), its instantaneous velocity is increased by about 26% if $R = 2/\pi$. The time-average velocity, however, will increase only about 13%.

Finally, the analysis of Section 8 relevant to the impingement of an acoustic wave upon the free surface indicates that the velocity, v_c, at the free surface midpoint should be related to the mean velocity, $\bar{v}$, by Eq. (8.8):

$$\frac{v_c}{\bar{v}} = \frac{1}{R^2}$$

where $\bar{v}$ is based upon the volume of fluid displaced at the free surface shortly after the passage of the wave, see Eq. (8.6). Note that the dependence upon the free surface curvature differs from that found subject to the assumption of incompressibility. The results for $R = 2/\pi$ differ by about 20%; the acoustic approximation giving 2.47, while the results of the analysis assuming incompressibility are in the range 1.93 - 2.12.

III. EXPERIMENTAL INVESTIGATION

10. Apparatus and Procedure

The experiments to be described were performed on bubbles rising in a circular glass tube nominally 7/16" in diameter. Such bubbles, when more than a tube diameter in length, have the property that their upper free surfaces are quite steady and very nearly hemispherical in shape, see, e.g., Taylor (22). The sudden downward acceleration of a bubble of this kind by means of a spark discharge in the liquid above it leads to the formation of a jet resembling those studied by Bowden and his students, (1), (2), (3), (8).

A sketch of the apparatus appears in Fig.14. A bubble was formed by a burst of air at a pressure of about 10 psig. admitted at the bottom of the water-filled tube. Approximately 18 in. above was a two-inch long working-section on which a high-speed camera was focused. Immediately above this was an aluminum fitting which held a quartz-crystal pressure transducer. Finally, into the glass tube extending above the fitting was inserted a spark gap. As the bubble rose into the working-section, the spark gap was triggered - - creating a spark bubble which, as it grew, drove the liquid beneath it downward. The result was a jet emanating from the apex of the spherical-cap bubble.

The photographic system consisted of a Beckman-Whitley model 224 rotating-drum camera used in conjunction with a strobe system. The bubbles were back-lighted by a xenon flashlamp. Typically, the

system was operated at a repetition rate of about 7000 pictures per second, with a total running time of about 8 ms. The interval between pictures was measured with a Beckman-Berkeley timer accurate to 0.1 μs.

The spark gap incorporated 0.030 in. diameter tungsten electrodes with a gap of about 0.005 in. supported by 3/32 in. brass rods pressed into holes drilled lengthwise through a three-quarter inch long acrylic cylinder which served to position the assembly within the tube. Two extra holes in the acrylic electrode holder allowed water to flow into the tube above the spark gap assembly as air was admitted at the bottom of the tube to form a bubble. The brass electrode supports were connected by means of shielded cable to a thyratron switch which, when triggered, discharged a capacitor across the spark gap. The energy of the discharge was typically one-half Joule - - the 0.01 mfd. capacitor having been charged to 10 kV.

Pressure histories within the tube were taken with a Kistler model 601A quartz transducer. This device has a circular active surface nominally one-eighth inch in diameter and a resonant frequency of about 130 kHz. Its signal was fed to a Kistler charge amplifier, the output of which was displayed on a Tektronix 551 oscilloscope and photographed.

Photographs of one experiment are shown in Fig. 15. The undeformed spherical-cap bubble appears in the first picture. Near the top edge of all the pictures is the spark gap with its holder just outside the camera field. A portion of a small air bubble trapped

beneath the holder is visible at the edge of the first frame. The spark gap was triggered a few microseconds after the first picture and a spark bubble approximately 0.6 tube diameters in size is visible in the following frame. Note that the air bubble beneath the spark gap holder has suffered a partial collapse. Subsequent pictures show the spark bubble collapsing and the formation of a jet at the apex of the now-deformed spherical-cap bubble. Note the cavitation arising in the fifth frame, after the collapse of the spark bubble.

In this particular sequence, the small bubble beneath the spark gap holder is of interest, for it seems to be the cause of the sheet of water which began to form at the base of the jet in frame ten. As this bubble collapsed and rebounded, successive sheets were formed; the next one begins at about 3.2 ms. followed by a third shown in the final series.

11. Reduction of the Data

The practice among investigators of bubbles rising through liquid in circular tubes has been, usually, to provide a flat-sided enclosure around the tube filled with a liquid having the same refractive index as the cylindrical tube. This largely eliminates refractive distortion in planes perpendicular to the tube axis and permits accurate measurements to be made directly from photographic negatives. For examples of this technique, see (22), (26), or (27). In at least one case, (28), a grid ruled on a small glass plate was inserted in the tube, photographed, and the resulting pattern used to

determine the distortion caused by the circular tube.

In the present study, the use of a water-filled box was found to be inconvenient. This was a consequence of the fact that experimentation was conducted in nearly complete darkness in deference to the camera; whose shutter, opened and closed by hand, was open for a relatively long period of time during any given experiment. Admission of sufficient external light through the box to fix the position of a bubble as it rose and still not fog the film proved to be a major problem.

Distortion was ultimately measured rather than eliminated. This was accomplished by inserting a carefully made gage into the tube and photographing it. The apparent horizontal position of each of twelve points along the gage, measured from the photograph, was compared to the true position of each point. The comparison showed that the true distance between two points on the same horizontal plane was the overall scale of the photograph multiplied by 0.763 times the apparent distance between the points. This ratio was constant to within 2% out to three-quarters of the true tube radius.

A check upon this quantity was made by measuring the apparent dimensions of the spark gap for experiments in which it was in the camera field. This permitted independent calculation of the ratio mentioned above. Agreement was found usually to within 2%, and to 5% in every case.

In addition to refractive distortion in horizontal planes caused by the circular tube, the curved free surface near the apex of the

spherical-cap bubble led to distortion in vertical planes. This prevented accurate measurement of the displacement of the jet tip in its early stages of formation; it also accounted for the fact that the jet seemed to issue from a point in space somewhat below the apex of the bubble.

The photographic data were reduced using a machinist's microscope accurate to 0.0001 in. The negative was aligned on the movable table of the microscope to make the axis of symmetry of the bubble coincide as closely as possible with one direction of table travel. This direction is termed z'' in the following discussion. For each value of z'', the radial position, r''_+ and r''_-, of two points on the bubble free surface were read - - one point on either side of the axis of symmetry. The bubble centerline was determined by averaging r''_+ and r''_- for each z'' then averaging the results to find a single number for each photograph. Knowing this, and the value of z'' at the apex of the bubble, the coordinate system was translated to the apex. The vertical coordinates, z', of the points in this system were multiplied by the scale of the photograph, F, and the horizontal coordinates, r', by sF to give the true physical dimensions. s is, of course, the factor 0.763 discussed above. F was determined from the apparent size of the spark gap assembly for those experiments in which it was within the camera field. In all the experiments, care was taken not to disturb the relative position of the camera and the tube, so the value of F was nearly constant at 1.57. The physical dimensions were finally rendered dimensionless by the tube radius,

$R_t = 0.223$ in.

In addition, coordinates of points on the spark bubble surface were determined by a scheme analogous in all respects to that described above. The origin of the coordinate system was, in this case, taken at the spark gap. Finally, the displacement of the jet tip was determined for several frames subsequent to its formation.

For comparison with the theoretical results of Part II, the value of the mean velocity imparted to that portion of the water column between the spark gap and the spherical-cap bubble is of major importance. This quantity was determined in two ways. The most accurate, when it could be applied, was to calculate the volume of the spark bubble. The mean velocity was then taken to be one-half the change in this quantity divided by the corresponding time interval and the cross-sectional area of the tube. The calculation was made relatively simple by the fact that the spark bubble was very nearly spherical even when its diameter was close to half that of the tube.

The other method for determining the mean velocity exploits the continuity equation in the form (8.6) of Part II to find the mean velocity, $\bar{v}_f$, in terms of the volume of liquid displaced at the free surface in the time between successive frames. Let (r_n', z_n') denote the value of (r', z') for the n^{th} point on one side of the axis of symmetry (n=0 denotes the point at the bubble apex). The volume of liquid, Q, bounded by the free surface, the plane $z' = 0$, and the cylinder whose radius is r_N' may then be approximated by

$$Q = 2\pi \frac{s^2 F^3}{R_t^3} S(r'_n, z'_n, N)$$

in units of cubic tube radii, where R_t is the tube radius and

$$S(r'_n, z'_n, N) = \sum_{n=1}^{N} \Delta r'_n \bar{r}'_n \bar{z}'_n$$

with

$$\Delta r'_n = r'_n - r'_{n-1}$$

$$\bar{r}'_n = \frac{1}{2}(r'_n + r'_{n-1})$$

$$\bar{z}'_n = \frac{1}{2}(z'_n + z'_{n-1}) \quad .$$

Since two values of r'_n are known for each z'_n, the volume can be determined twice to afford a check. Note that the primed variables refer to distances measured on the actual photograph.

If the volume, Q, is determined for two consecutive photographs (using the value of z''_o found for the apex of the bubble in the first as the reference in both cases), to give Q_1 and Q_2, then the mean velocity, $\bar{v}$, of the liquid column is just

$$\bar{v} = \frac{Q_2 - Q_1}{\pi t}$$

in units of tube radii per second if t is the time in seconds between the two photographs. Denoting by z'_c the displacement of the midpoint of the free surface in successive frames, the centerline velocity, v_c, is

$$v_c = \frac{F z'_c}{R_t t}$$

tube radii per second. The quantity $\frac{v_c}{\bar{v}}$ given by

$$\frac{v_c}{\bar{v}} = 2z'_c \frac{R_t^2}{s^2F^2} \frac{1}{S_2 - S_1}$$

is to be compared to the results of the analysis of Part II. Note that this ratio is not likely to be determined particularly accurately -- containing, as it does, the difference between two quantities which in practice are often within 15 per cent of one another. In addition, the factors s and F appear to the second power so that errors contained in them will be approximately doubled when the ratio is formed.

The effects of errors in the factor s upon the calculated radius of curvature of one of these bubbles can be made clear by considering an ellipse given by

$$\frac{r^2}{a^2} + \frac{z^2}{b^2} = 1 \quad ,$$

for which it can be shown that the radius of curvature, R, evaluated at r = 0 is

$$R = \frac{a^2}{b^2} z(0) \quad .$$

Now, a small change in the horizontal semi-axis of length a corresponds to a small change in the factor s which accounts for distortion in horizontal planes. Since a appears to the second power, it is clear that the uncertainty in R will be approximately double the uncertainty in s.

The accuracy of the photographic measurements depended upon the dimension being estimated. For example, the apparent diameter of the well-defined electrodes was determined to within 2% or less.

Measurements on the bubble free surface were repeatable to about 0.0005 in. Since differences were taken, this cannot be given in terms of a percentage; however, measurements were repeated on one of the spark bubbles and the results for its mean radius found to agree within 1.6%. Hence, the volume in this case was determined to within 5%.

12. Experimental Results

Initial free surface shapes of three representative bubbles are shown in Fig. 16 together with arcs of radius 0.65 for comparison. The bubble profile was not found to vary in any systematic way with the dimensionless distance, d_s, to the spark gap, nor were any variations found to occur when experiments were performed using a dilute solution of a high molecular weight polymer instead of tap water. Radii of curvature were obtained at the bubble apexes by averaging values calculated for the coordinates of points on the free surfaces. The values so obtained agreed with estimates determined by plotting the points and estimating the radii graphically.

The initial downward velocities of the apexes of the bubbles were found, with a few exceptions, to be in the range 20 - 50 feet per second while the jets were observed to travel at speeds slightly higher. An intimate relation does not necessarily exist between these quantities since the spark bubble often continued to expand after the time at which the velocity of the free surface midpoint was calculated. Table I summarizes the results for the nose radii, the initial midpoint velocities, and the ultimate velocities attained by the jets. The scatter in the values for the radius, R, is apt to be a consequence of errors in the factors s and F as discussed in Section 11.

Mean radii for several spark bubbles are shown in Fig. 19. These were determined by averaging values calculated for about 20 points on the bubble surface; error bars in the figure indicate the maximum and minimum values for the individual points. The spark bubbles

were invariably elongated in the direction of the tube axis, although the opposite seems true in the photographs due to distortion in horizontal planes.

Figure 20(a) shows the history of a spark-produced pressure wave in the apparatus of Fig. 14. Electrical disturbances created as a result of the spark discharge were responsible for the initial transient. Following a quiescent period, there can be seen a low-level excitation caused by disturbances propagating within the tube wall, subsequent to this was a pulse due to the passage of the first wave in the water. The frequency of the oscillation following the pressure pulse was approximately the natural frequency of the transducer and so it is not likely to represent the pressure field behind the first wave.

The record shown in Fig. 20(a) was made with no bubble in the tube; however, the presence of a bubble did not change the pressure history in any essential way, nor did the character of the trace vary with the distance between the transducer and the spark gap. Pressure measurements were also made with the transducer mounted in the wall of a 12 in. diameter tank containing about 11 in. of water. A spark-produced pressure wave incident normally upon the transducer was observed to produce a history closely resembling that shown in Fig. 20(a). The peak pressure was, in this case, in the neighborhood of 300 psig. when the spark gap was brought to within 1/4 in. of the transducer and fell rapidly as the distance was increased. The risetime and pulse width did not vary significantly, however.

That the wave system behind the initial pressure front is quite

complicated is shown by the schlieren photographs of Fig. 20(b). The pictures are of several pressure waves with varying amounts of delay introduced into the photographic apparatus. Note the rarefaction waves ahead of the main compression wave in the photograph taken 12μs. after the spark was triggered, these are doubtless a consequence of the compliance of the glass tube. What appear to be two compression waves converging toward the tube axis can be seen in the photograph taken at 15μs. Note also that the thickness of the initial front is much smaller than the tube diameter. Since the pressure transducer was about a fourth of the tube diameter in size, it seems unlikely that even the maximum pressure was determined accurately.

The speed of the photographic system did not permit the waves reflected upward from the surface of the spherical-cap bubble to be viewed; however, widespread cavitation was often observed in the water column after a time sufficient for the compression wave to be reflected - - an example is the experiment shown in Fig. 21(a). This is convincing evidence that the reflected system was predominately tension as one would expect.

IV. DISCUSSION AND COMPARISON WITH THE THEORY

The radii at the apexes of the bubbles used in these experiments were observed to be less than that found by other investigators for bubbles rising in somewhat larger tubes. Table I shows the value 0.66 tube radii to be typical of the bubbles examined in the course of the present study; that given by other authors is 0.70 - 0.71, see (23), (26), and (29). The discrepancy seems to be an effect of surface tension. Though no detailed studies of its effects upon the nose radii of these bubbles have been made, the work of Zukoski, (30), shows that surface tension will affect their rate of rise.

Define the surface tension parameter, Σ, by

$$\Sigma = \frac{\sigma}{\rho g R_t^2}$$

where

σ = surface tension constant (73 c.g.s. units for water at room temperature)

ρ = density of liquid for a gas bubble rising through liquid

g = acceleration due to gravity

and

R_t = tube radius = 0.223 in. = 0.565 cm.

Using the room temperature properties of water gives $\Sigma = 0.23$, which has been found by Zukoski (see Fig. 2 of his paper) to be sufficiently high to slow the upward velocity of a long bubble by about 17% compared to a similar bubble rising in the absence of surface tension.

Dumitrescu, (27), studied long bubbles rising through water in tubes of various diameters and found that the apexes of those which rose in a tube 0.99 cm. in diameter were slightly more pointed than those observed in larger tubes. He gives no values for the radii of curvature at the apexes, but suggests that surface tension is responsible for the difference in shape. Goldsmith and Mason, (26),found that surface tension decreased the nose radii of bubbles rising through viscous liquids, and while they investigated air bubbles rising in water-filled tubes of approximately the diameter of that used in the present work, gave no values for the nose radii. Although the work of Dumitrescu and of Goldsmith and Mason is largely qualitative with respect to the effects of surface tension upon the radius of curvature, there is none which contradicts the present finding that the radius is in the neighborhood of 0.66 tube radii.

The volume calculations described in Section 11 yield results such as those shown in Fig. 17 for a typical case. The ordinate is the volume, in units of the tube radius cubed, within the confines of the free surface, the horizontal plane through the apex of the undeformed bubble, and the cylinder whose radius is the abscissa. The difference between the ordinates for $r = r_1$, say, represents the volume displaced at the free surface for $r \leqslant r_1$ in the time between the frames from which the calculations were made. This difference is shown in Fig. 18 to the same scale as Fig. 17. It will be seen that the difference, at its maximum, is about 30% of the volume shown in the preceding figure and that it becomes roughly constant for $r \simeq 0.6$. In

reducing the data, the displaced volume was determined at five or six points in the range $0.65 < r < 0.80$ and upper and lower limits established for each side of the bubble - - a total of four values. Linear interpolation was used to find the volume for values of r differing from those for which it had been calculated.

The ratio of the initial velocity at the free surface midpoint v_c to the initial mean velocity, $\bar{v}_f$, based upon the volume of fluid displaced at the free surface, is shown in Fig. 22 for each of the bubbles listed in Table I. Also shown is the ratio $v_c/\bar{v}_s$, where $\bar{v}_s$ is the mean velocity calculated from the spark bubble volume. Error bars in the case of $\bar{v}_f$ indicate the highest and lowest values among the four from which each of the averages (summarized in Table II) was obtained. It will be seen in Fig. 22 that these ratios are rather broadly scattered around three for all values of d_s, and so exceed by about 50% the value predicted from the incompressible analysis. The estimate of Bowden and McOnie (Ref. 1), for the ratio of jet velocity to mean velocity was two or three for jets moving at speeds in the neighborhood of 6000 feet per second. They gave no values for the initial curvature, however.

The ratios $v_c/\bar{v}_f$ and $v_c/\bar{v}_s$ agreed within 20% for all but two of the experiments; these exceptional cases are indicated in Table II by question marks adjacent to the entries. In the absence of cavitation, conservation of mass requires that the volume displaced by the lower portion of the spark bubble must appear as a displacement at the free surface or that flow must occur across the horizontal

plane through the electrodes. Flow parallel to the tube wall in the liquid film below the bubble apex seems less likely. Differences between $\bar{v}_s$ and $\bar{v}_f$ for a single experiment are not attributable to any phenomena associated with compressibility because displacements were measured after a time sufficient for the system of pressure waves to undergo many reflections and be dissipated. Finally, the data were reduced assuming axial symmetry, so any deviation of the spark bubble from this condition leads to errors in $\bar{v}_s$.

Cavitation was not observed in experiments having $d_s < 1.61$, and in this case, shown in Fig. 15, the cavities were of negligible extent. The experiment in which d_s was 2.15 featured cavitation in significant amounts and a very irregular spark bubble, hence the approximate agreement between $\bar{v}_s$ and $\bar{v}_f$ is simply coincidence. This experiment was exceptional in that a small jet had formed in the time between the first two frames of the photographic record preventing precise measurement of the midpoint displacement.

The pressure maxima from histories exemplified by that of Fig. 20(a) were observed to vary unpredictably from 200 psig. to beyond 400 psig.; however, the average taken over 30 - 35 consecutive experiments performed at a single value of the spacing between the spark gap and the transducer was found consistently to be in the interval 290 - 350 psig. with a standard deviation of 30 - 40 psig. Using 350 psig., it follows from Eq. (8.1): $v_o = p_o/\rho_c$, that the velocities behind the first wave were of the order of 5 feet per second. If this were doubled at the free surface as predicted by simple acoustic theory, the resulting increase at the free surface

midpoint would be about 25% of the initial midpoint velocity for many of the bubbles studied. It is likely, however, that the acoustic waves were stronger than indicated by the pressure traces for the reasons mentioned earlier. Hence the possibility remains open that the complete removal of compressibility effects would lead to satisfactory agreement.

Discrepancies due to the finite displacement of the free surface do not seem to be important. The displacement used to calculate v_c was typically less than 0.3 tube radii (see Table III), hence one would expect the midpoint velocity to be affected by less than 15%, based upon the two-dimensional analysis of Section 7. The experimental evidence does not warrant the drawing of definite conclusions, though, since effects of this magnitude would not make themselves apparent when the data scatter to the extent indicated by Fig. 22.

The analysis of Section 5 indicates that, for a column whose length is less than its radius, the effects of non-uniformities in the applied velocity will be of importance in predicting the velocity at the free surface. These non-uniformities may be characterized by the coefficient D_1 introduced in Section 6 and can be estimated for the experiments in the following way: First, suppose that the spark bubble can be idealized as an expanding sphere, then when its radius and radial velocity are R_s and $\dot{R}_s$, respectively, the axial component velocity, v_z, on the spherical surface is

$$v_z = \dot{R}_s \cos\theta$$

where θ is the polar angle. Now if one assumes that this velocity acts across a horizontal plane, the Fourier-Bessel coefficients, D_n, follow in the form

$$D_n = \frac{2\dot{R}_s}{J_o^2(k_n)} \int_o^{R_s} J_o(k_n r) r \cos\theta \, dr$$

since $v_z = 0$ when $r > R_s$.

Making the substitution $r = R\sin\theta$, there results

$$D_n = \frac{2R_s^2\dot{R}_s}{J_o^2(k_n)} \int_o^{\pi/2} J_o(k_n R \sin\theta)\sin\theta \cos^2\theta \, d\theta$$

which can be shown (see Ref. (24), p. 373, for instance) to be

$$D_n = \frac{2R_s^2\dot{R}_s}{J_o^2(k_n)} \frac{1}{k_n R_s}\sqrt{\frac{\pi}{2k_n R_s}}\, J_{3/2}(k_n R_s) \quad .$$

The requirement that the mean velocity, D_o, be unity gives

$$R_s^2\dot{R}_s = \frac{2}{\sqrt{\pi}}$$

so that, finally, $D_1 = 3.15$ and $D_2 = 1.68$ for the typical case $R_s = 0.5$. This is certainly an overestimate for D_1 since the approximation used for the axial velocity contains a physically unrealistic

discontinuity in its slope.

Now the effective column length, d, is apt to be somewhat less than the distance, d_s, to the spark gap due to the presence of the spark bubble, so from Fig. 12 one would expect the midpoint velocity for the experiments with the lowest values (d_s = 0.73, 0.83) to exceed, by possibly more than 50%, the same quantity for experiments with larger values of d_s. Reference to Fig. 22, shows, however, no compelling evidence to suggest that this occurred in the experiments. The midpoint velocity does indeed increase with respect to the mean velocity based upon the spark bubble volume, however, the trend is not confirmed by the other ratio.

The experiments shown in Figs. 15 and 21(a) are typical of some thirty-five of which photographs were made. In two cases, however, a very different behavior was observed. One of these is shown in Fig. 21(b) where it will be seen that a small jet, much less well-defined than the others, was formed. This experiment and a similar one (d_s = 1.01 in Table I) are characterized by very low initial midpoint velocities, which suggests that the stabilizing forces due to surface tension were nearly sufficient to prevent the formation of a jet.

No accurate estimates have been made of the relation between the maximum mean velocity imparted to the column and the ultimate jet velocity. For experiments in which the motion was slow enough to permit accurate estimates of the maximum spark bubble size to be made, the corresponding velocities were sufficiently low that surface tension was likely to have been important, conversely, when the

velocities were high enough to render surface tension effects negligible, the temporal resolution of the camera permitted only very approximate estimates of the maximum spark bubble size. Briefly, the jet velocity was found to be only slightly greater than the maximum mean velocity at the lowest speeds and increased to about 4 times this quantity at the highest.

The theoretical analysis is only indicative with respect to the final jet velocity; however, if a steady flow of this kind exists, it is easy to show that the steady jet velocity should exceed the mean velocity by a factor of two in either two or three dimensions. This may be seen by considering the flow as it appears to an observer moving with the mean velocity. Such an observer will perceive that fluid approaches along the free surface near the walls with unit velocity, say, turns through 180°, and leaves with unit velocity along the jet free surface. Thus to an observer with respect to whom the fluid at infinity is at rest, the velocity of the jet will be two units.

The process of jet formation in these experiments may be understood in the context of Taylor instability, for as the spark bubble collapsed, the liquid beneath it was accelerated upward, creating a situation at the free surface conducive, by Taylor's criterion, to the growth of small perturbations in the velocity or displacement there.

Finally, the free surface shape just after the start of motion is shown for one case in Fig. 23, and for comparison a theoretical curve determined from the exact two-dimensional analysis of Section

2. The exact solution was continued from the experimental free surface rather than the corresponding theoretical shape shown in Fig. 2. The disagreement is, of course, rather severe near the centerline, where three-dimensional effects are likely to be significant; closer to the tube wall, however, where these phenomena are of lesser importance, the theoretical and experimental shapes are somewhat closer. The two-dimensional midpoint displacement, $(\Delta_c)_2$, was determined for Fig. 23 by the relation

$$(\Delta_c)_2 = \frac{(v_c/\bar{v})_2}{(v_c/\bar{v}_f)_3} \quad (\Delta_c)_3$$

where the subscripts 2 and 3 refer to two and three dimensions, respectively, and $(v_c/\bar{v})_2$ is the theoretical value, $\pi/2$.

V. SUMMARY

Several mathematical models have been propounded to account for the jet observed to form at the curved free surface of a column of liquid subjected to a rapid acceleration. The fluid has been assumed inviscid throughout and incompressible in most of the analyses. A two-dimensional problem was solved exactly for small time and forms the standard against which the results of more approximate theories were tested for reasonableness. This solution predicts that the element of fluid situated at the midpoint of a rather special curved free surface should suffer a jump in velocity equal to $\pi/2$ times the mean velocity applied impulsively to the column. Further, the theory predicts that the velocity jump elsewhere on the free surface is less - - suggesting the possibility of jet formation.

Several perturbation analyses have been carried out in Section 4 based upon the assumption that the initial free surface is nearly planar. The results for the midpoint velocity of a two-dimensional problem of this kind were found to agree within 5% with those for a special case of the exact problem, while those of the corresponding three-dimensional problem predict a jump in velocity at the free surface midpoint in the neighborhood of twice the mean velocity imparted to the column. In both cases, the increment in velocity at the free surface midpoint was found to be proportional to the curvature of the initial free surface and to be greater there than at other points on the free surface, see Eqs. (4.33), (4.34), and Fig. 11.

An attack on the axially-symmetric problem has also been

made by assuming that the system of impulses acting across the horizontal plane through the midpoint of the free surface is the same as - - or closely related to - - the analogous quantity found to be acting in the two-dimensional problem which was solved exactly. Though no firm basis exists for such an assumption, the results to which it leads are not unreasonable in view of those found in two-dimensions, and they do tend to confirm the results of the axially-symmetric perturbation analysis.

Experiments employing slender bubbles rising in a circular tube were conducted upon the phenomenon. The apex radii of these bubbles, listed in Table I, were found to be within a few per cent of that used in the theory, and when accelerated rapidly downward, were observed to deform in a manner resembling that predicted theoretically, see Fig. 23. Quantitatively, however, the midpoint velocity was found to be systematically in excess of that predicted by the three-dimensional perturbation analysis. It is likely that the approximations made in obtaining the solution of the axially-symmetric problem are to blame for a portion of the discrepancy; however, one is led to speculate that effects associated with compressibility are also of importance.

The effects peculiar to very short columns subject to non-uniformly-applied impulsive velocities have been examined for an axially-symmetric column with a nearly planar free surface. It was concluded that the jump in velocity experienced by the free surface is affected to a negligible extent, even by strong non-uniformities, unless the column's length is smaller than its radius. This finding was not

borne out conclusively by the experiments, however.

A solution valid for slightly longer times than were those discussed above was found for a simplified two-dimensional problem. The results indicate that the velocity of the fluid element at the free surface midpoint should increase as the motion proceeds; however, the increase is slight and no manifestations of the phenomenon were observed in the experiments.

Finally, effects associated with compressibility were considered in a very approximate way and the conclusion reached that the impingement of a plane acoustic wave upon a hemispherical free surface should lead to effects qualitatively similar to those arising in the various incompressible analyses. Specifically, the velocity at the midpoint of the free surface was found to exceed the velocity at other points situated thereon - - again suggesting a jet. The factor by which the velocity at this point exceeds the mean velocity (based upon the volume of fluid displaced at the free surface) depends strongly upon the behavior of the acoustic waves as they propagate past the bubble apex; however, and no experimental evidence was obtained to justify any assumptions in this regard.

References

(1) F. P. Bowden, M. P. McOnie, "Cavities and Micro Munro Jets in Liquids: Their Role in Explosion," Nature, 206, 380 (1965).

(2) F. P. Bowden, J. H. Brunton, "The Deformation of Solids by Liquid Impact at Supersonic Speeds," Proc. Roy. Soc., A, 263, 433, (1961).

(3) J. H. Brunton, "The High-Speed Photography of Liquid/Solid Impact," Proc. 5th Int. Cong. on High-Speed Photography, 1960, J. S. Courtney-Pratt, Ed., Soc. Mot. Pic. Telev. Eng., New York, p. 503, (1962).

(4) R. W. Watson, F. C. Gibson, "Jets from Imploding Bubbles," Nature, 204, 1296, (1964).

(5) C. F. Naude, A. T. Ellis, "On the Mechanism of Cavitation Damage by Nonhemispherical Cavities Collapsing in Contact with a Solid Boundary," Trans. ASME, J. Basic Eng., 83, 648, (1961). (See also C. F. Naude, PhD Thesis, Calif. Inst. of Tech., 1960).

(6) T. B. Benjamin, A. T. Ellis, "The Collapse of Cavitation Bubbles and the Pressures Thereby Produced Against Solid Boundaries," Phil. Trans. Roy. Soc., A, 260, 221, (1966).

(7) N. D. Shutler, R. B. Mesler, "A Photographic Study of the Dynamics and Damage Capabilities of Bubbles Collapsing Near Solid Boundaries," Trans. ASME, J. Basic Eng., 87, 511, (1965).

(8) F. P. Bowden, "The Formation of Microjets in Liquids Under the Influence of Impact or Shock," Phil. Trans. Roy. Soc., A, 260, 94, (1966).

(9) Warren, Price, Photograph submitted to a discussion on liquid impact by A. V. Smith, Phil. Trans. Roy. Soc., A, 260, 279, (1966).

(10) G. Birkhoff, D. P. MacDonald, E. M. Pugh, G. I. Taylor, "Explosives with Lined Cavities," J. Appl. Physics, 19, 563, (1948).

(11) S. P. Kozirev, "On Cumulative Collapse of Cavitation Cavities," Trans. ASME, J. Basic Eng., 90, 116, (1968).

(12) G. Birkhoff, T. E. Caywood, "Fluid Flow Patterns," J. Appl. Phys., 20, 646, (1949).

(13) N. Curle, "Unsteady Two-Dimensional Flows with Free Boundaries," Proc. Roy. Soc., A, 325, 375, (1956).

(14) F. H. Harlow, W. E. Pracht, "Formation and Penetration of High-Speed Collapse Jets," Physics of Fluids, 9, 1951, (1966).

(15) F. H. Harlow, J. P. Shannon, "The Splash of a Liquid Drop," J. Appl. Phys., 38, 3855, (1967).

(16) H. Lamb, Hydrodynamics, 6th Ed., Dover Publications, Inc. New York, (1945).

(17) G. Birkhoff, "Induced Mass with Free Boundaries," Quart. Appl. Math., 10, 81, (1952).

(18) E. Jahnke, F. Emde, Tables of Functions with Formulae and Curves, 4th Ed., Dover Publications, Inc., New York, (1945).

(19) M. Abramowitz, I. A. Stegun, Eds., Handbook of Mathematical Functions with Formulas, Graphs, and Mathematical Tables, 5th Printing, U.S. Dept. of Commerce, Washington, D.C., (1966).

(20) D. P. Wang, T. Yao-tsu Wu, "Small-Time Behavior of Unsteady Cavity Flows," Calif. Inst. of Tech., Hydrodynamics Lab., Rep. No. 97-3, March, (1963).

(21) N. I. Muskhelishvili, Some Basic Problems of the Mathematical Theory of Elasticity, 2nd English ed., P. Noordhoff, Ltd., Groningen, The Netherlands, (1962).

(22) R. M. Davies, G. I. Taylor, "The Mechanics of Large Bubbles Rising through Extended Liquids and through Liquids in Tubes," Proc. Roy. Soc., A, 200, 375, (1950).

(23) G. Birkhoff, E. H. Zarantonello, Jets, Wakes, and Cavities, Academic Press, New York, (1957).

(24) G. N. Watson, A Treatise on the Theory of Bessel Functions, 2nd Ed., Cambridge University Press, (1966).

(25) F. B. Hildebrand, Advanced Calculus for Applications, 5th Printing, Prentice-Hall, Englewood Cliffs, N.J. (1965).

(26) H. L. Goldsmith, S. G. Mason, "The Movement of Single Large Bubbles in Closed Vertical Tubes," J. Fluid Mech., 14, 42, (1962).

(27) D. T. Dumitrescu, "Stromung an einer Luftblase in Senkrechten Rohr," ZAMM, 23, 139, (1943).

(28) S. P. Lin, "Velocity of a Bubble Rising in Liquid along the Axis of a Circular Tube," Phys. of Fluids, 10, 2283, (1967).

(29) R. Collins, "The Effect of a Containing Cylindrical Boundary on the Velocity of a Large Gas Bubble in a Liquid," J. Fluid Mech., 28, 97, (1967).

(30) E. E. Zukoski, "Influence of Viscosity, Surface Tension, and Inclination Angle on Motion of Long Bubbles in Closed Tubes," J. Fluid Mech., 25, 821, (1966).

TABLE I

Summary of Nose Radii and Velocities

d_s	R	v_c	v_j
0.73	0.65	46.3	66.6
0.83	0.66	39.6	59.9
0.98	0.62	37.4	57.1
1.01	0.68	23.2	3.79
1.02	0.66	30.2	37.8
1.04	0.68	28.1	35.0
1.30	0.67	18.7	6.70
1.61	0.67	33.2	43.2
*2.15	0.67	72.4	136.2
*3.18	†	34.3	49.0
*3.26	0.62	44.2	54.3
3.67	0.66	23.2	22.0
*7.46	0.66	48.5	86.8
23.4	0.62	33.9	58.4

d_s = distance from spark gap to bubble apex, tube radii

R = radius of curvature of undeformed bubble, tube radii; cf $R = 2/\pi \simeq 0.64$ used in theoretical analysis.

v_c = initial midpoint velocity, feet per second

v_j = ultimate jet velocity, feet per second

*indicates 50 ppm. polyethylene dioxide solution

† indicates photograph of undeformed bubble was unviewable, initial shape was taken to be that of bubble for which $d_s = 3.26$.

TABLE II

Summary of Velocity Ratios

d_s	$v_c/\bar{v}_f$	$v_c/\bar{v}_s$
0.73	3.11	3.62
0.83	3.12	3.88
0.98	3.47	3.56
1.01	2.62	2.56
1.02	3.14	5.14 (?)
1.04	2.93	2.62
1.30	3.18	3.30
1.61	3.36	2.10 (?)
*2.15	2.53	2.84
*3.18	3.22	
*3.26	3.26	
3.67	3.56	
*7.46	2.92	
23.4	2.96	

d_s = distance from spark gap to bubble apex, tube radii

v_c = initial midpoint velocity

$\bar{v}_f$ = mean velocity based on volume displaced at free surface

$\bar{v}_s$ = mean velocity based on spark bubble volume

* indicates 50 ppm polyethylene dioxide solution.

TABLE III

Summary of Spark Bubble Radii and Initial Free Surface Displacement

d_s	Δ_c	R_s	t
0.73	0.242	0.46	0.096
0.83	0.260	0.46	0.122
0.98	0.320	0.51	0.160
1.01	0.170	0.32	0.139
1.02	0.200	0.39	0.122
1.04	0.200	0.48	0.127
1.30	0.122	0.38	0.122
1.61	0.292	0.59	0.161
*2.15	0.593	0.68	0.150
*3.18	0.159		0.099
*3.26	0.311		0.150
3.67	0.202		0.166
*7.46	0.392		0.150
23.4	0.118		0.150

d_s = distance from spark gap to bubble apex, tube radii

t = time in ms. from spark discharge

Δ_c = free surface displacement at midpoint with respect to initial position

R_s = mean spark bubble radius, tube radii

* indicates 50 ppm polyethylene dioxide solution.

APPENDIX A

Polynomial Approximation to $\omega_o(x, d)$

The real part of Eq. (2.29) can be shown to be

$$u_o = - U(x) \sin \frac{\pi x}{2}$$

where

$$U(x) = \sum_{m=1}^{\infty} (-1)^m \frac{2m}{4m^2+1+4m \cos \frac{\pi x}{2}}$$

$$- \sum_{m=1}^{\infty} (-1)^m \frac{2m}{4m^2+1-4m \cos \frac{\pi x}{2}} \quad . \qquad \text{(A-1)}$$

In finding the least squares approximation to u_o, Eq. (A-1) was evaluated for $-1 < x < 1$ at intervals of 0.05. The approximation was then weighted in favor of points near the origin (the neighborhood of greatest interest) by counting twice the values of u_o at $x = \pm 0.05, \pm 0.10, \pm 0.15, \pm 0.20, \pm 0.25,$ and ± 0.30.

The final approximation is

$$u_o(x, d) = \sum_{m=1}^{5} b_{2m-1} x^{2m-1} \qquad \text{(A-2)}$$

where

$$b_1 = -2.3049$$

$$b_3 = 10.340$$

$$b_5 = -21.199$$

$$b_7 = 20.681$$

$$b_9 = -7.5220 \quad .$$

This may be integrated according to Eq. (2.30) to give

$$A_{2m} = \frac{b_{2m-1}}{2m}$$

where the A_{2m}'s are given with Eq. (2.31)

APPENDIX B

Evaluation of

$$I(\xi) = \int_0^\infty \frac{\cos k\xi \sin k}{k \cosh ka} \, dk$$

It is convenient to examine the integral obtained by differentiation with respect to ξ:

$$I'(\xi) = -\int_0^\infty \frac{\sin k\xi \sin k}{\cosh ka} \, dk$$

which may be written in the form

$$I'(\xi) = \frac{1}{4} \, \mathrm{Re} \int_{-\infty}^{\infty} \frac{e^{i(1+\xi)k} - e^{i(1-\xi)k}}{\cosh ka} \, dk \quad . \qquad (B\text{-}1)$$

Now consider

$$\int_{-\infty}^{\infty} \frac{e^{i\alpha k}}{\cosh ka} \, dk \quad , \quad \alpha \text{ real.}$$

This may be found in Ref. (B-1), p. 30 to be

$$\frac{\pi}{a} \frac{1}{\cosh \frac{\pi\alpha}{2a}} \quad .$$

Use of this result, with $\alpha = 1 \pm \xi$, in Eq. (B-1) leads to

$$I'(\xi) = \frac{\pi}{4a} \left[\frac{1}{\cosh \frac{\pi}{2a}(1+\xi)} - \frac{1}{\cosh \frac{\pi}{2a}(1-\xi)} \right] \quad .$$

A little manipulation gives

$$I'(\xi) = -\frac{\pi}{2a} \frac{\sinh \frac{\pi}{2a} \sinh \frac{\pi\xi}{2a}}{\sinh^2 \frac{\pi}{2a} + \cosh^2 \frac{\pi\xi}{2a}}$$

which may be integrated to yield

$$I(\xi) = \tan^{-1} \frac{\sinh \frac{\pi}{2a}}{\cosh \frac{\pi\xi}{2a}} + \text{const} \quad . \tag{B-2}$$

Now recall that $I(\xi)$ is the normal derivative, along $\eta = a$, of the harmonic function $\omega_{\frac{1}{2}}(\xi, \eta)$. This permits a fundamental property of functions of this type to be invoked to evaluate the constant. Specifically,

$$\oint_C \frac{\partial \omega_{\frac{1}{2}}}{\partial n} \, d\ell = 0$$

where the integral is taken over the boundary of the region occupied by fluid in the ζ-plane. The contribution to this integral along $\eta = 0$ is -2 in view of the normalization chosen in Eq. (2.32). Since the first term of the expression (B-2) is positive-definite, the constant must be set equal to zero to ensure convergence along $\eta = a$. Note that the velocity must be at least finite at infinity, precluding all but finite contributions to the integral from the portions of the contour at infinity.

Reference

(B-1) A. Erdelyi, ed. Tables of Integral Transforms, Vol. 1, Calif. Inst. of Tech. Bateman Manuscript Project, McGraw-Hill, 1954.

APPENDIX C

Calculation of $B_n(m)$ and Related Sums

Integration by parts of the right side of the equation

$$B_n(m) = -2\int_o^1 x_m \cos n\pi x \, dx$$

results in

$$B_n(m) = (-1)^{n+1}\frac{2m}{(n\pi)^2} - \frac{m(m-1)}{(n\pi)^2} B_n(m-2) \qquad (C-1)$$

$B_n(2)$ is readily shown to be

$$(-1)^{n+1}\frac{2\ 2}{(n\pi)^2} \quad .$$

Mathematical induction can then be used to show that, in general,

$$B_n(2m) = \frac{2(-1)^{m+n+1}}{(n\pi)^2}\sum_{k=1}^{m}\frac{(2m)!\ (-1)^k}{(2k-1)!(n\pi)^{2m-2k}} \quad , \qquad m > 1 \quad .$$

The first five of these are

$$B_n(2) = (-1)^{n+1}\frac{2\cdot 2}{(n\pi)^2}$$

$$B_n(4) = (-1)^{n+1}\frac{2\cdot 4}{(n\pi)^2}\left[1 - \frac{3!}{(n\pi)^2}\right]$$

$$B_n(6) = (-1)^{n+1}\frac{2\cdot 6}{(n\pi)^2}\left[1 - \frac{4\cdot 5}{(n\pi)^2} + \frac{5!}{(n\pi)^4}\right]$$

$$B_n(8) = (-1)^{n+1}\frac{2\cdot 8}{(n\pi)^2}\left[1 - \frac{6\cdot 7}{(n\pi)^2} + \frac{4\cdot 5\cdot 6\cdot 7}{(n\pi)^4} - \frac{7!}{(n\pi)^6}\right]$$

$$B_n(10) = (-1)^{n+1}\frac{2\cdot 10}{(n\pi)^2}\left[1 - \frac{8\cdot 9}{(n\pi)^2} + \frac{6\cdot 7\cdot 8\cdot 9}{(n\pi)^4} - \frac{4\cdot 5\cdot 6\cdot 7\cdot 8\cdot 9}{(n\pi)^6} + \frac{9!}{(n\pi)^8}\right] .$$

The sums

$$\varphi_{m,y}(0,0) = \sum_{n=1}^{\infty} n\pi B_n(m)$$

are then, for the first five even values of m,

$$\varphi_{2,y}(0,0) = 2\lambda_1$$

$$\varphi_{4,y}(0,0) = 4(\lambda_1 - 3!\lambda_3)$$

$$\varphi_{6,y}(0,0) = 6(\lambda_1 - 4\cdot 5\lambda_3 + 5!\lambda_5) \qquad \text{(C-2)}$$

$$\varphi_{8,y}(0,0) = 8(\lambda_1 - 6\cdot 7\lambda_3 + 4\cdot 5\cdot 6\cdot 7\lambda_5 - 7!\lambda_7)$$

$$\varphi_{10,y}(0,0) = 10(\lambda_1 - 8\cdot 9\lambda_3 + 6\cdot 7\cdot 8\cdot 9\lambda_5 - 4\cdot 5\cdot 6\cdot 7\cdot 8\cdot 9\lambda_7 + 9!\lambda_9)$$

where the λ_p's are given by

$$\lambda_p = 2\sum_{n=1}^{\infty} \frac{(-1)^{n+1}}{(n\pi)^p} \quad .$$

The first few of these are tabulated below for p odd.

p	λ_p
1	4.4127×10^{-1}
3	5.8152×10^{-2}
5	6.3533×10^{-3}
7	6.5728×10^{-4}
9	6.6966×10^{-5}

Substitution of these in Eqs. (C-2) gives Eqs. (5.8). Note that the calculation of $\varphi_{2m,y}(0,0)$ involves the difference between rather large numbers as m increases. Consequently, the accuracy of this quantity is somewhat less than the five figures retained in λ_p. This fact is

reflected in Eqs. (5.8).

APPENDIX D

Calculation of $C_n(m)$ and Related Sums

The equation for $C_n(m)$ may be written

$$C_n(m) = - \frac{2}{k_n^{m+2} J_o^2(k_n)} \int_o^{k_n} \eta^{m+1} J_o(\eta)\, d\eta$$

after an obvious change of variable. Two integrations by parts gives

$$C_n(m) = - \frac{2m}{k_n^2 J_o(k_n)} - \frac{m^2}{k_n^2} C_n(m-2) \qquad \text{(D-1)}$$

where the relations

$$J_1(0) = J_1(k_n) = 0$$

$$\int \eta J_o(\eta)\, d\eta = \eta J_1(\eta)$$

and

$$\int J_1(\eta)\, d\eta = - J_o(\eta)$$

have been used. The recursion relation (D-1) connecting $C_n(m)$ and $C_n(m-2)$ is the same as that derived in Ref. (24), p. 581. $C_n(0)$ can easily be shown to vanish so the other C_n's follow from (D-1).

As in the two-dimensional case discussed in Appendix C, it is possible to find a general expression for $C_n(2m)$. The formula

$$C_n(2m) = \frac{4(-1)^{m+1}}{k_n^2 J_o(k_n)} \sum_{\ell=1}^{m} \frac{(-1)^\ell (m!)^2}{\ell!\,(\ell-1)!} \left(\frac{2}{k_n}\right)^{2m-2\ell}$$

can be shown to hold by means of mathematical induction. It follows that

$$C_n(2) = -\frac{2\cdot 2}{k_n^2 J_o(k_n)}$$

$$C_n(4) = -\frac{2\cdot 4}{k_n^2 J_o(k_n)}\left[1 - \frac{2\cdot 4}{k_n^2}\right]$$

$$C_n(6) = -\frac{2\cdot 6}{k_n^2 J_o(k_n)}\left[1 - \frac{4\cdot 6}{k_n^2} + \frac{2\cdot 4^2\cdot 6}{k_n^4}\right]$$

$$C_n(8) = -\frac{2\cdot 8}{k_n^2 J_o(k_n)}\left[1 - \frac{6\cdot 8}{k_n^2} + \frac{4\cdot 6^2\cdot 8}{k_n^4} - \frac{2\cdot 4^2\cdot 6^2\cdot 8}{k_n^6}\right]$$

$$C_n(10) = -\frac{2\cdot 10}{k_n^2 J_o(k_n)}\left[1 - \frac{8\cdot 10}{k_n^2} + \frac{6\cdot 8^2\cdot 10}{k_n^4} - \frac{4\cdot 6^2\cdot 8^2\cdot 10}{k_n^6} + \frac{2\cdot 4^2\cdot 6^2\cdot 8^2\cdot 10}{k_n^8}\right]$$

The sums

$$\chi_{m,z}(0,0) = \sum_{n=1}^{\infty} k_n C_n(m)$$

then may be written, for $m = 2, 4, 6, 8,$ and $10,$

$$\chi_{2,z}(0,0) = 2\alpha_1$$

$$\chi_{4,z}(0,0) = 4(\alpha_1 - 2\cdot 4\alpha_3)$$

$$\chi_{6,z}(0,0) = 6(\alpha_1 - 4\cdot 6\alpha_3 + 2\cdot 4^2\ 6\alpha_5) \qquad \text{(D-2)}$$

$$\chi_{8,z}(0,0) = 8(\alpha_1 - 6\cdot 8\alpha_3 + 4\cdot 6^2\cdot 8\alpha_5 - 2\cdot 4^2\cdot 6^2\cdot 8\alpha_7)$$

$$\chi_{10,z}(0,0) = 10(\alpha_1 - 8\cdot 10\alpha_3 + 6\cdot 8^2\cdot 10\alpha_5 - 4\cdot 6^2 8^2 10\alpha_7 + 2\cdot 4^2\cdot 6^2\cdot 8^2\cdot 10\alpha_9)$$

where the α_p's are

$$\alpha_p = -2\sum_{n=1}^{\infty} \frac{1}{k_n^p J_o(k_n)} \quad .$$

The quantity $-\frac{1}{2}\alpha_1$, may be found in Ref. (D-1), p. 166. The others have been calculated using the values of k_n and $J_o(k_n)$ in Ref. (D-2). The results for $p = 1, 3, 5, 7,$ and 9 are shown in the following

table:

p	α_p
1	7.6958×10^{-1}
3	7.4099×10^{-2}
5	5.6774×10^{-3}
7	4.0212×10^{-4}
9	2.7734×10^{-5}

Use of these values in Eqs. (D-2) gives (5.20). Note that the terms in the expressions for $\chi_{2m,z}(0,0)$ become rather large with increasing m - - the last two terms in $\chi_{10,z}(0,0)$, for example, are -36.734 + 20.263. Thus, even though five figures have been retained in α_p, the final result is accurate only to three figures.

References

(D-1) E. Jahnke, F. Emde, Tables of Functions with Formulae and Curves, 4th Ed., Dover, New York (1945).

(D-2) F. W. J. Olver, ed. Roy. Soc. Math. Tables, 7, Bessel Functions, Part III, Zeros and Associated Values, Cambridge Univ. Press, (1960).

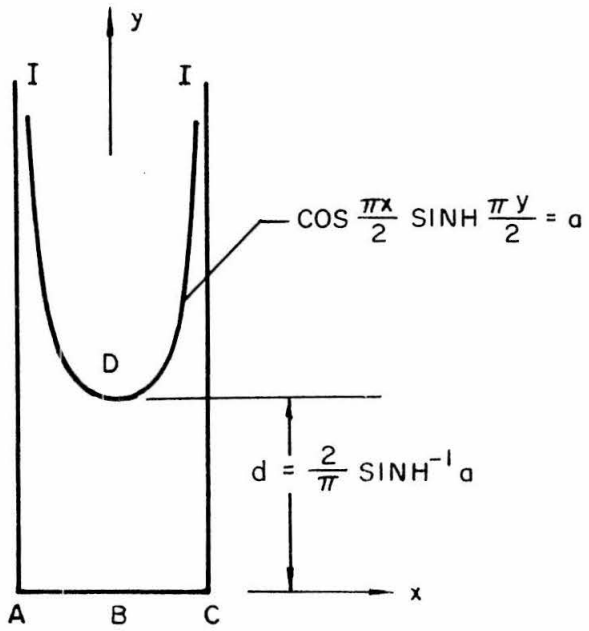

Fig. 1(a): Region of z-plane occupied by fluid

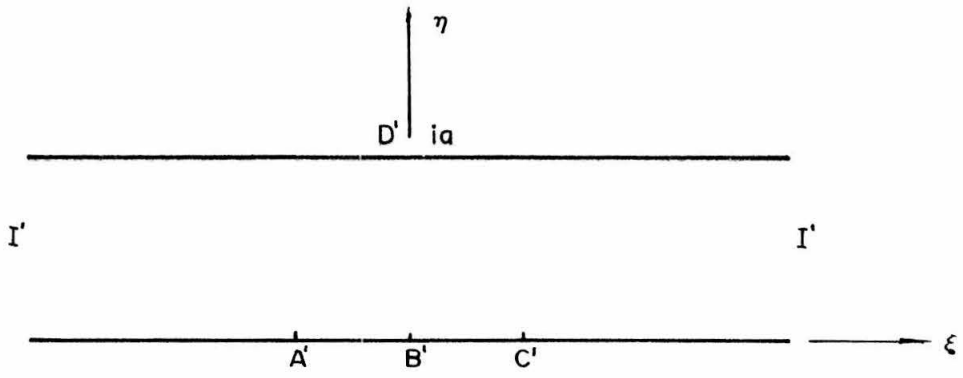

Fig. 1(b): Correspondence between points in the z-plane and ζ-plane under the transformation $\zeta = \sin \frac{\pi z}{2}$.

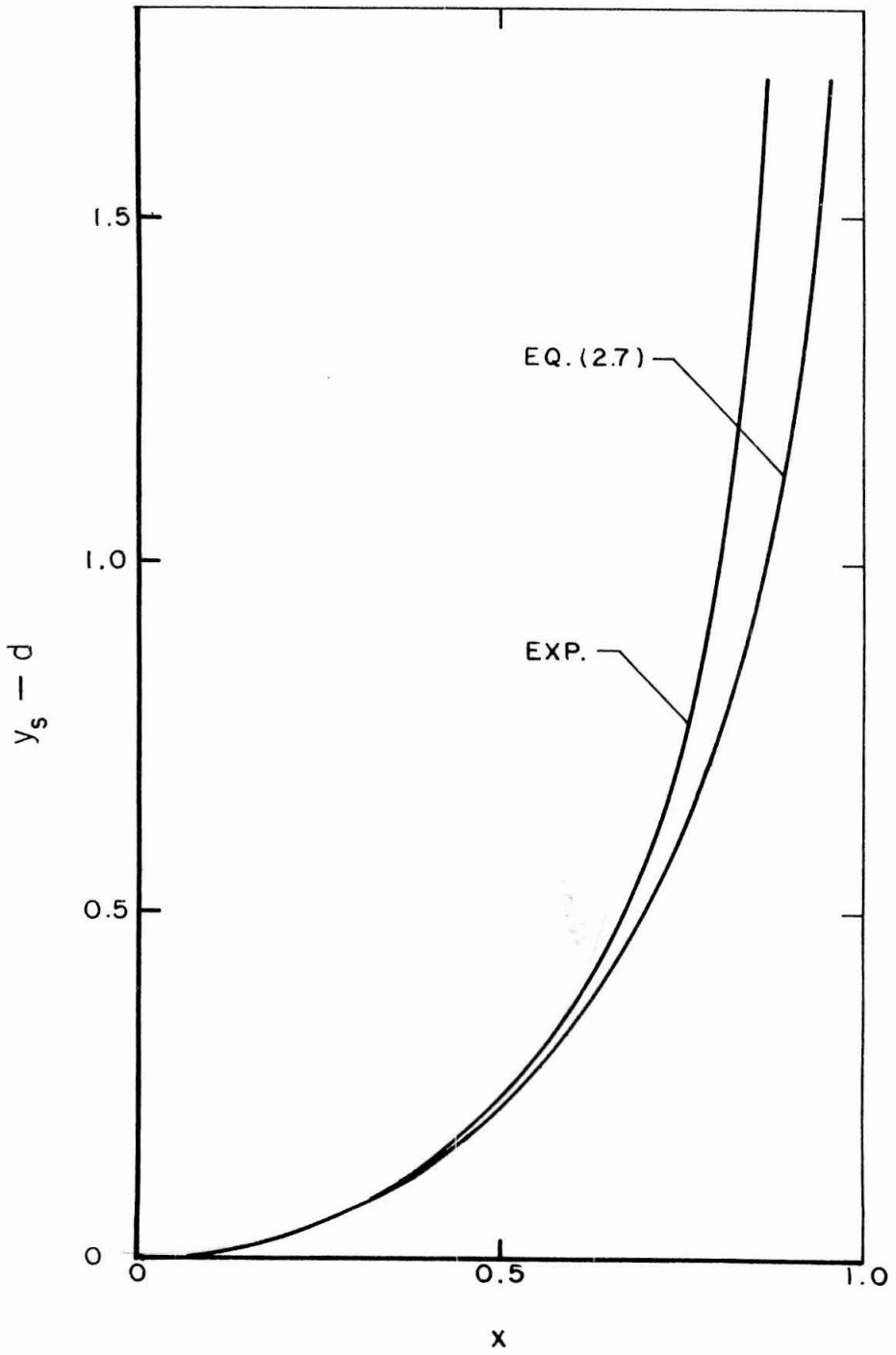

Fig. 2: Comparison of free surface required for exact two-dimension solution with an axially-symmetric free surface observed experimentally.

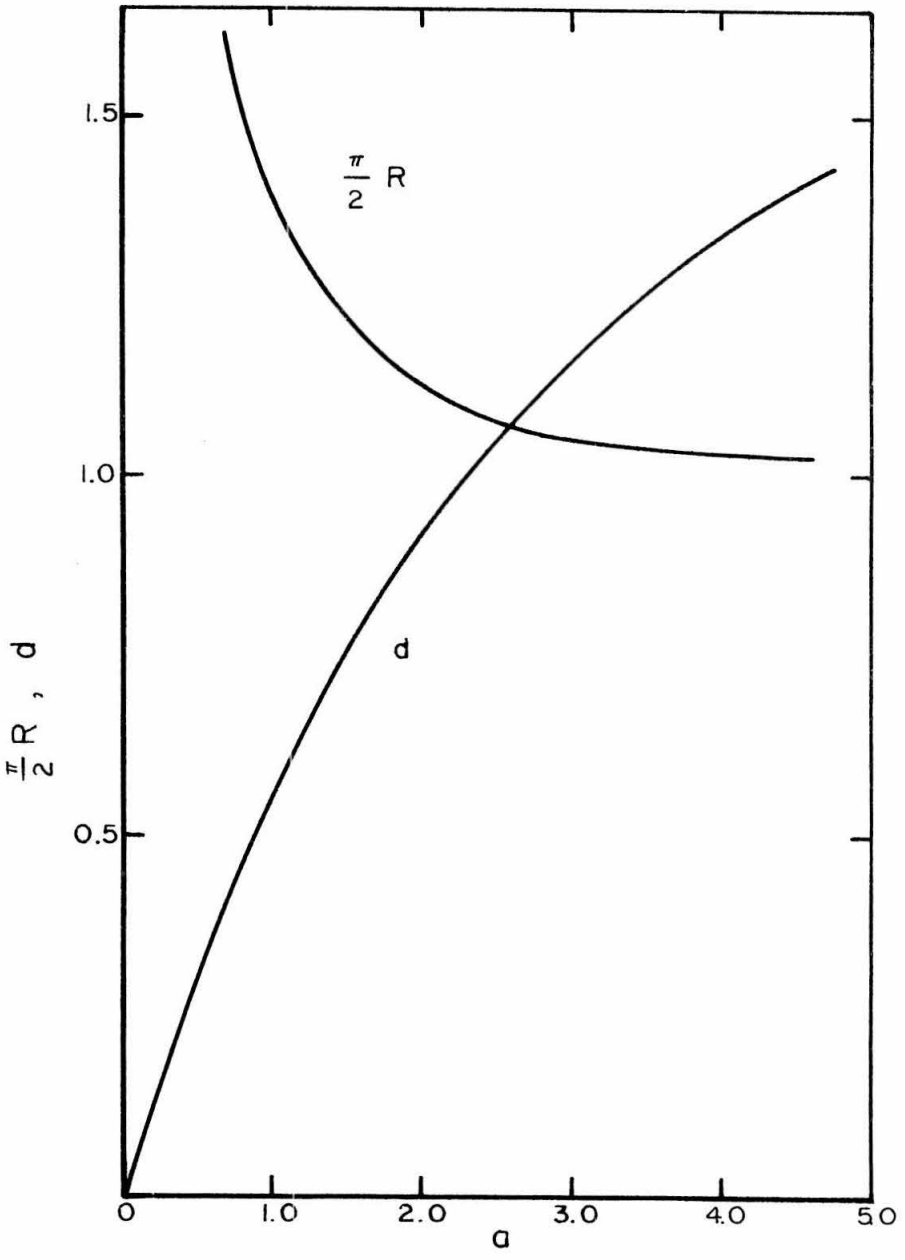

Fig. 3: Variation of free surface curvature R, and column length, d, with the parameter, a.

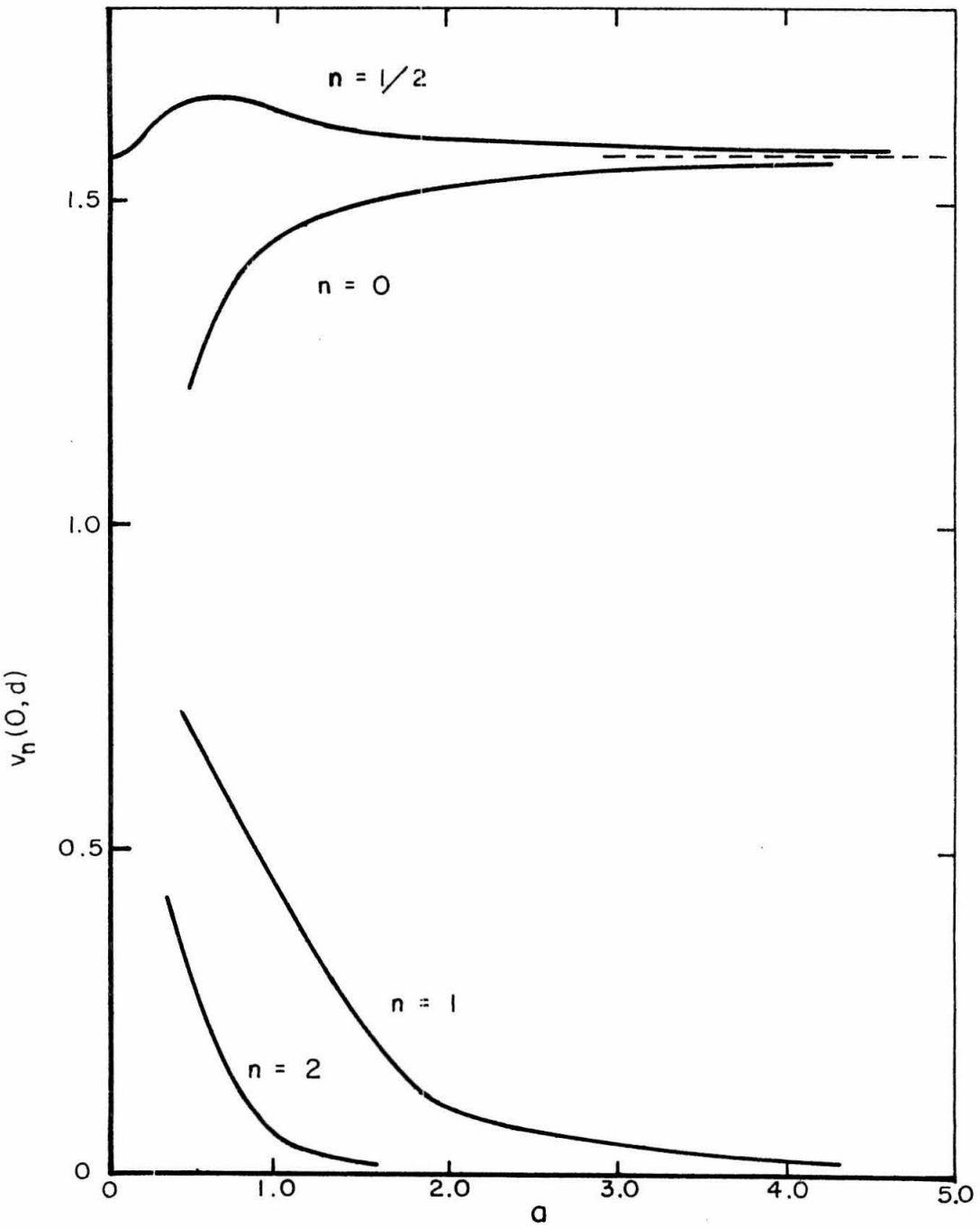

Fig. 4: Midpoint velocity for exact two-dimensional solution, n = 0, 1, 2 from Eq. (2.28), n = 1/2 from Eq. (2.34).

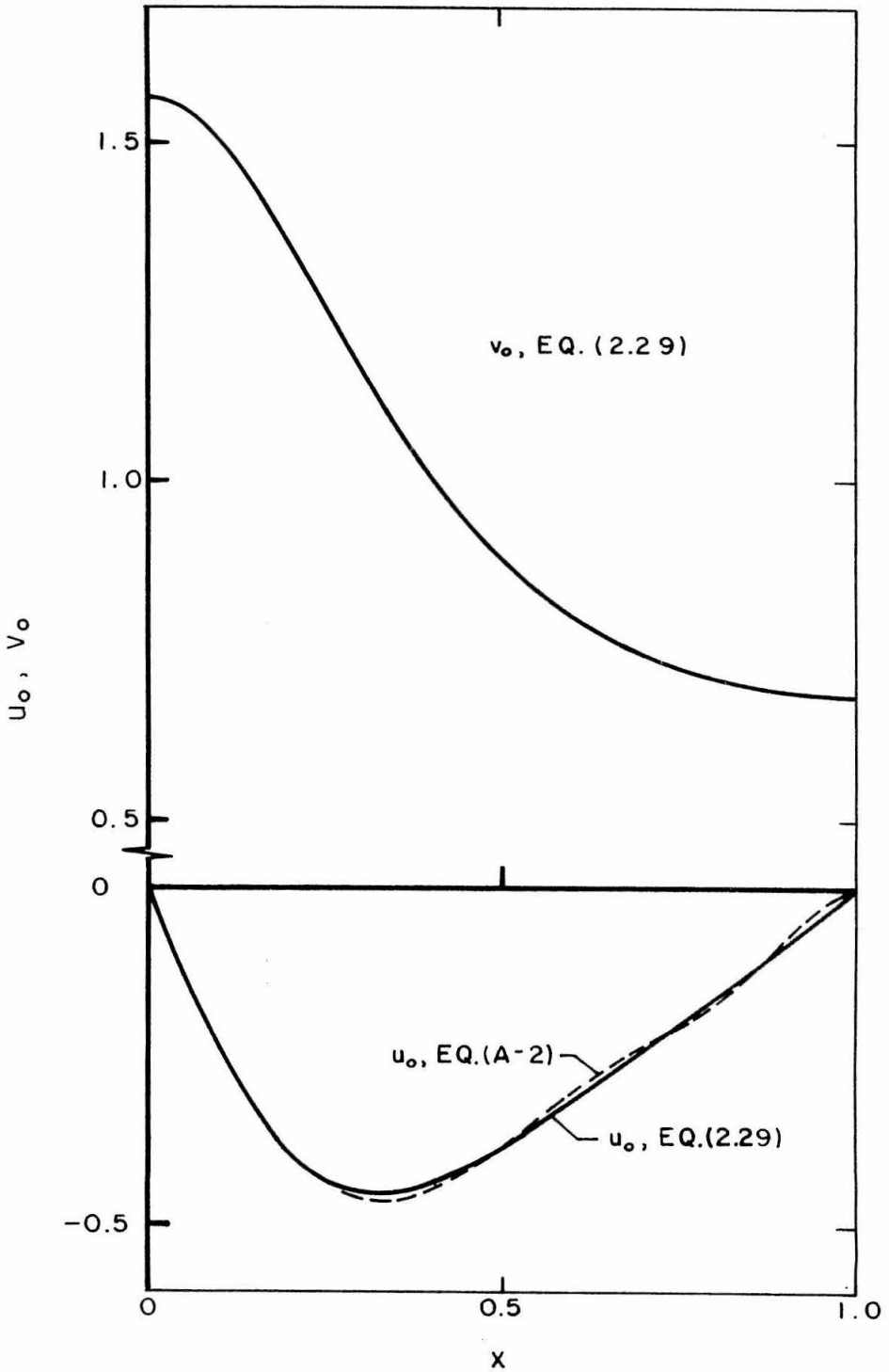

Fig. 5: Velocities along y = d from exact two-dimensional theory, a » 1. Eq. (A-2) is ninth order polynomial approximation to u_o.

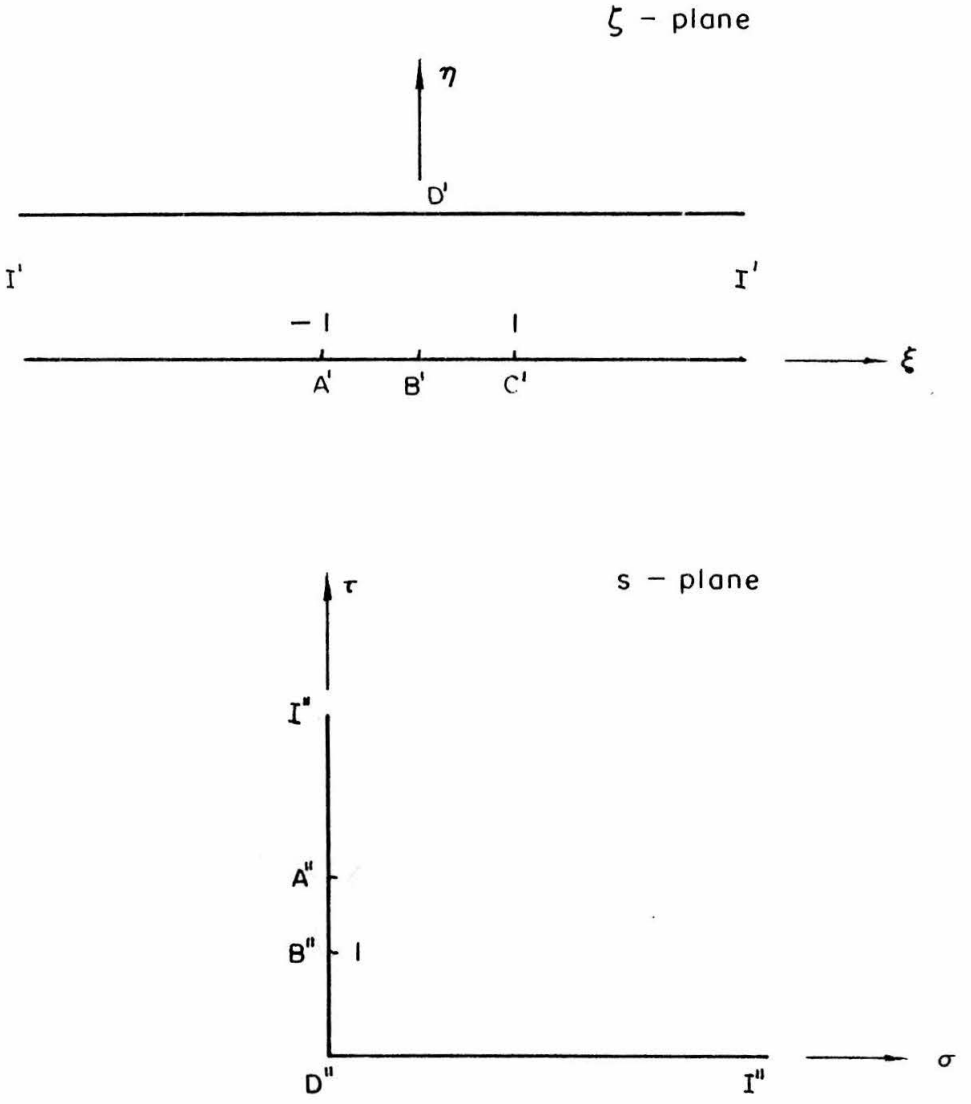

Fig. 6: Correspondence between points in the ζ-plane and s-plane under the transformation $s = -\sinh \pi/2a(\zeta - ia)$.

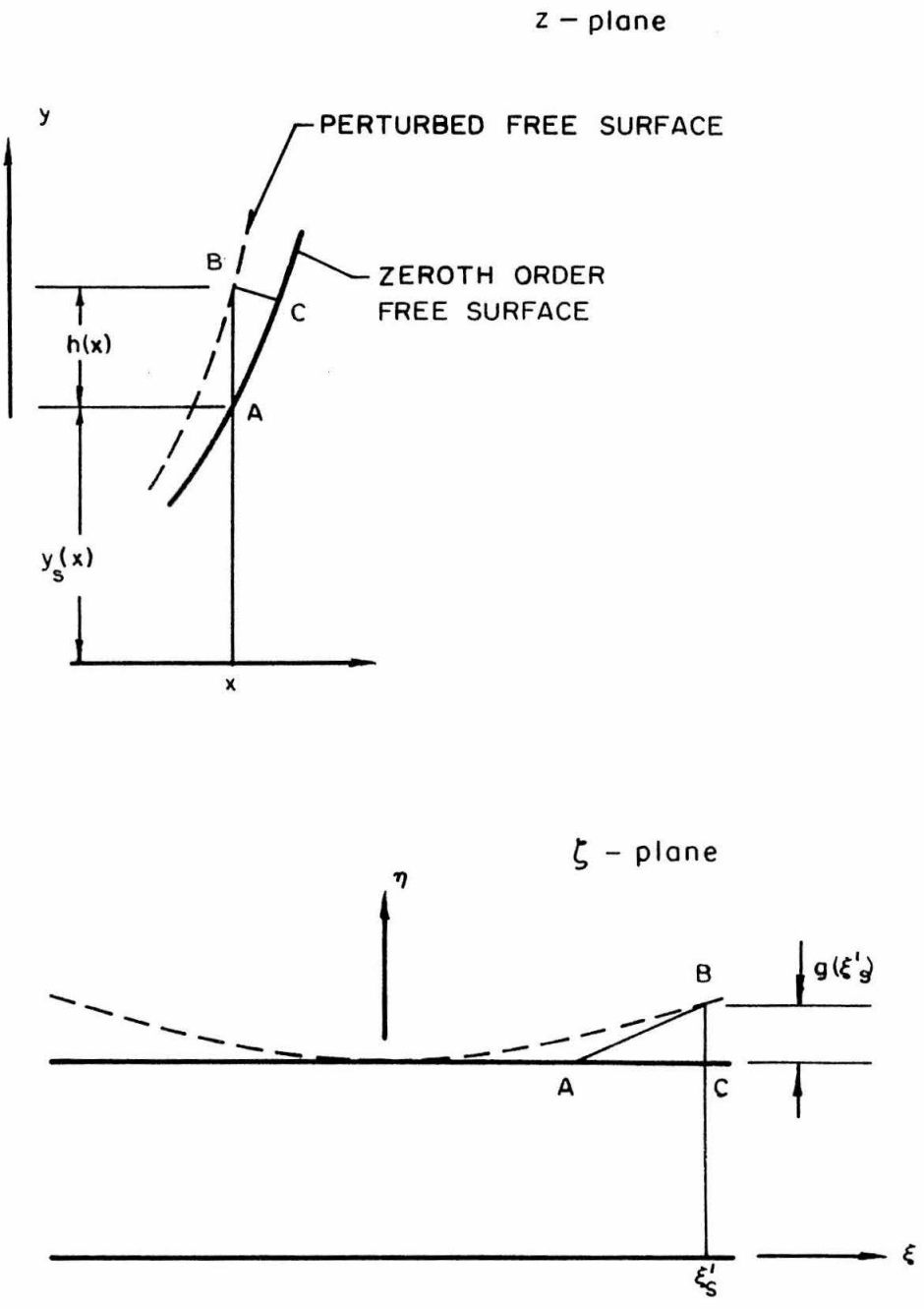

Fig. 7: Geometry of perturbed free surface in z-plane and ζ-plane.

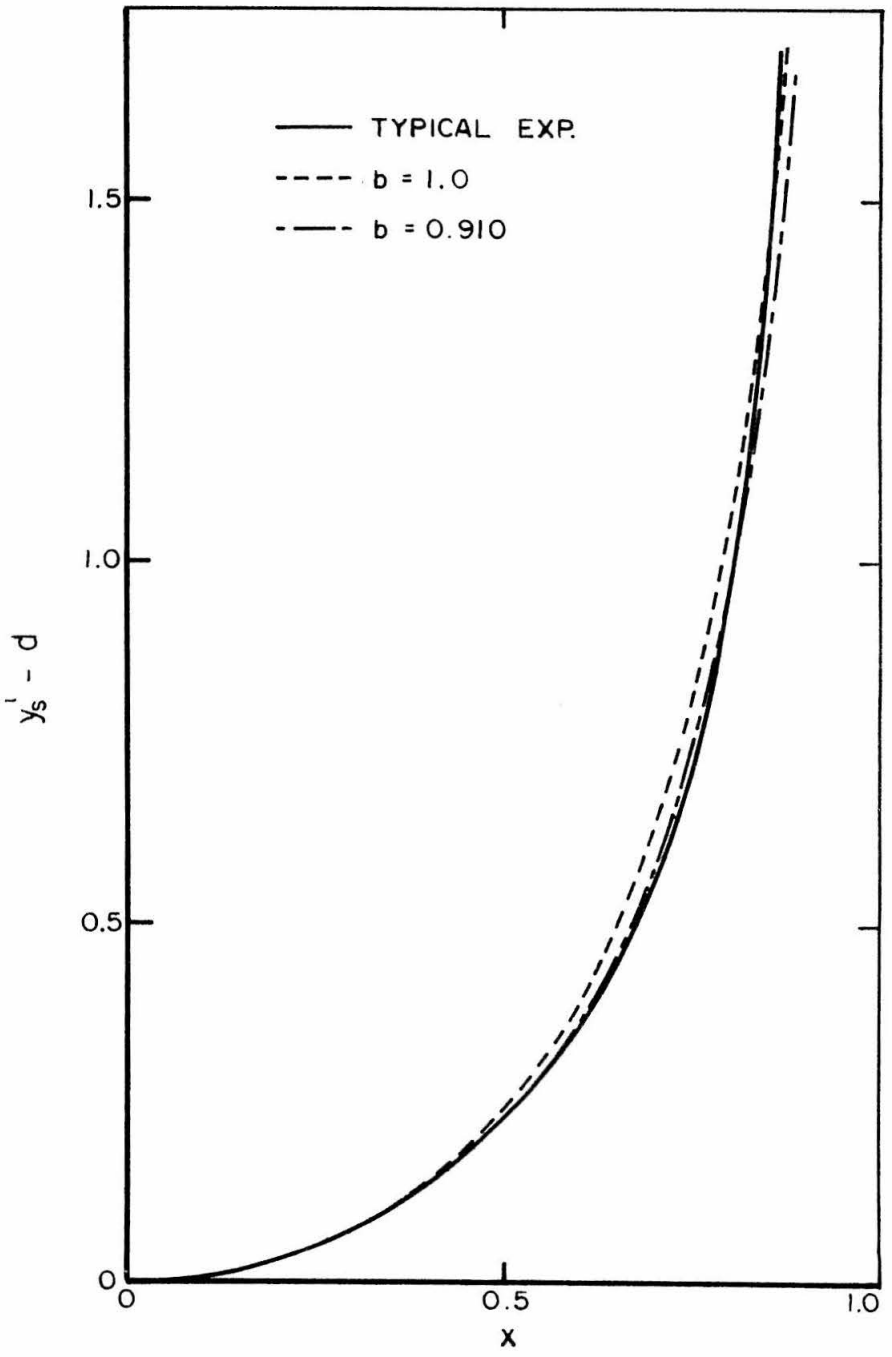

Fig. 8: Showing typical experimental free surface shape and surface shapes used in perturbation solution from Eq. (3.32).

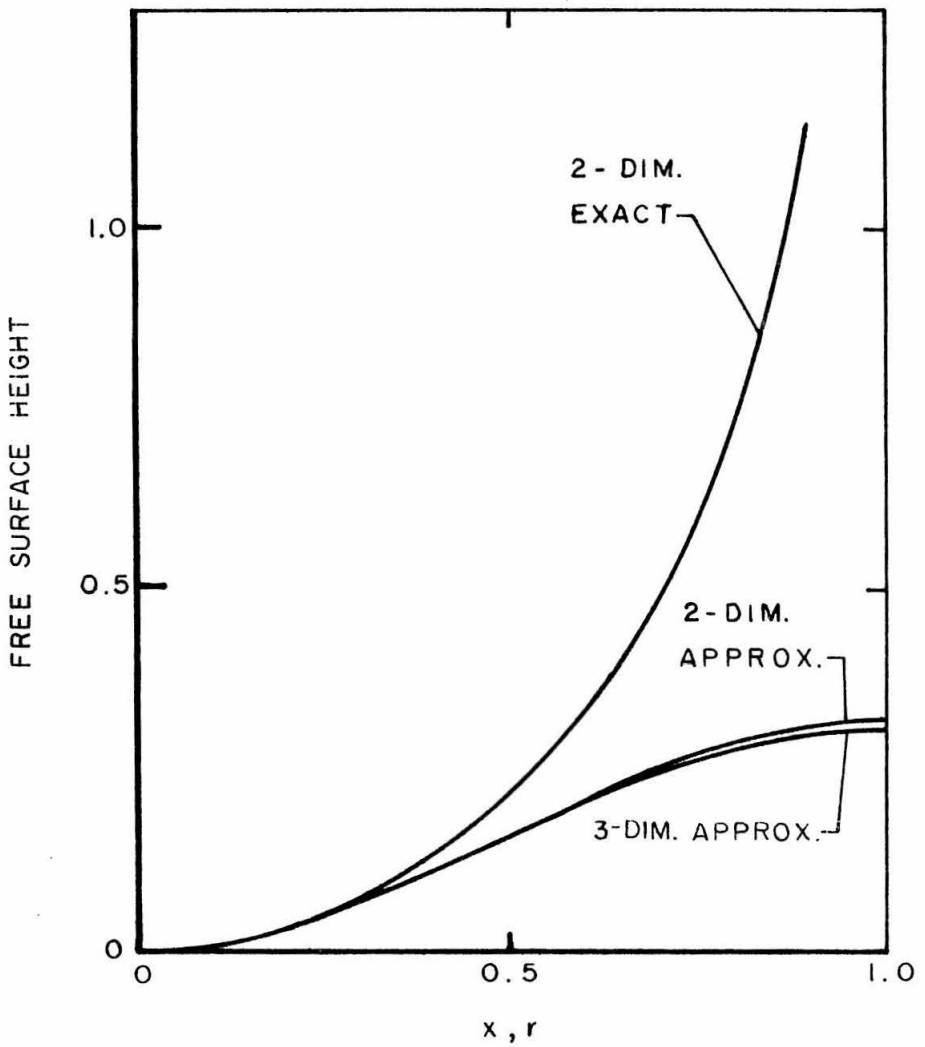

Fig. 9: Comparison of free surface heights for exact and approximate theories. Two-dimensional exact from Eq. (2.7), two-dimensional approximate from Eq. (4.1), and three-dimensional approximate from Eq. (4.2).

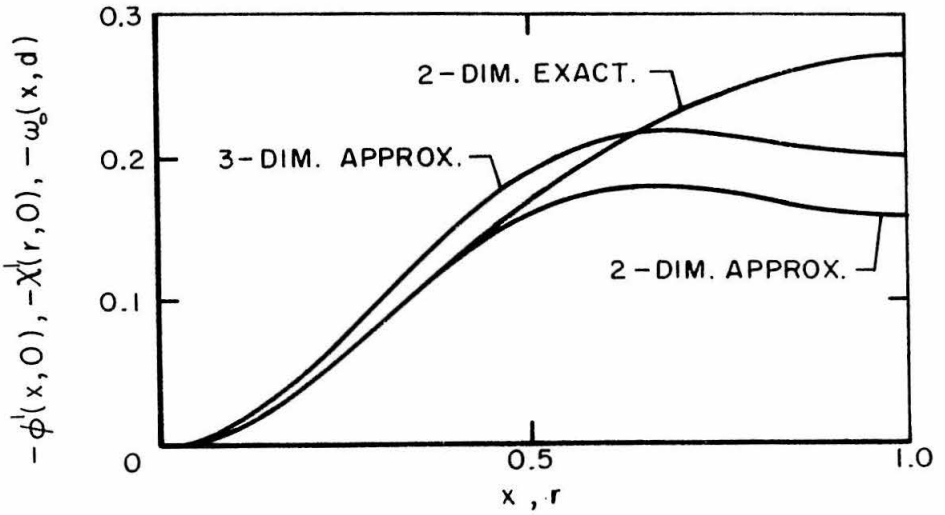

Fig. 10(a): Comparison of exact and approximate theories; exact two-dimensional impulse, $-\omega_0(x,d)$, from Eq. (2.31), approximate two-dimensional impulse, $-\varphi'(x,0)$, from Eq. (4.29), and approximate three-dimensional impulse from Eq. (4.30).

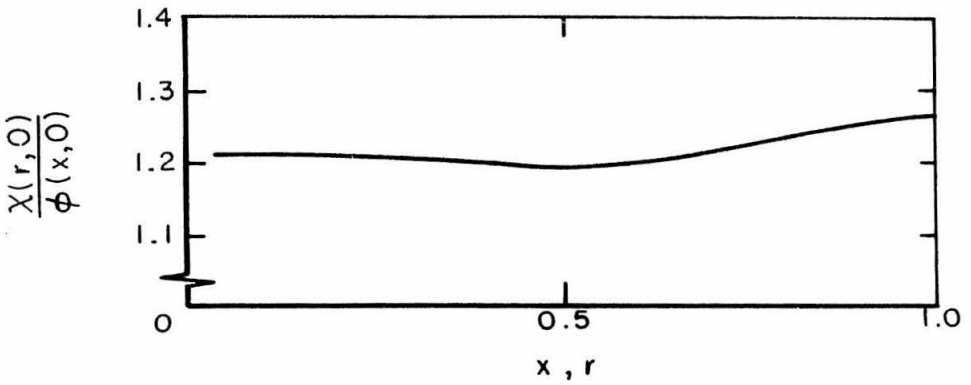

Fig. 10(b): Comparison of approximate theories: ratio of three-dimensional impulse, $-\chi'(r,0)$, to two-dimensional impulse, $-\varphi'(x,0)$.

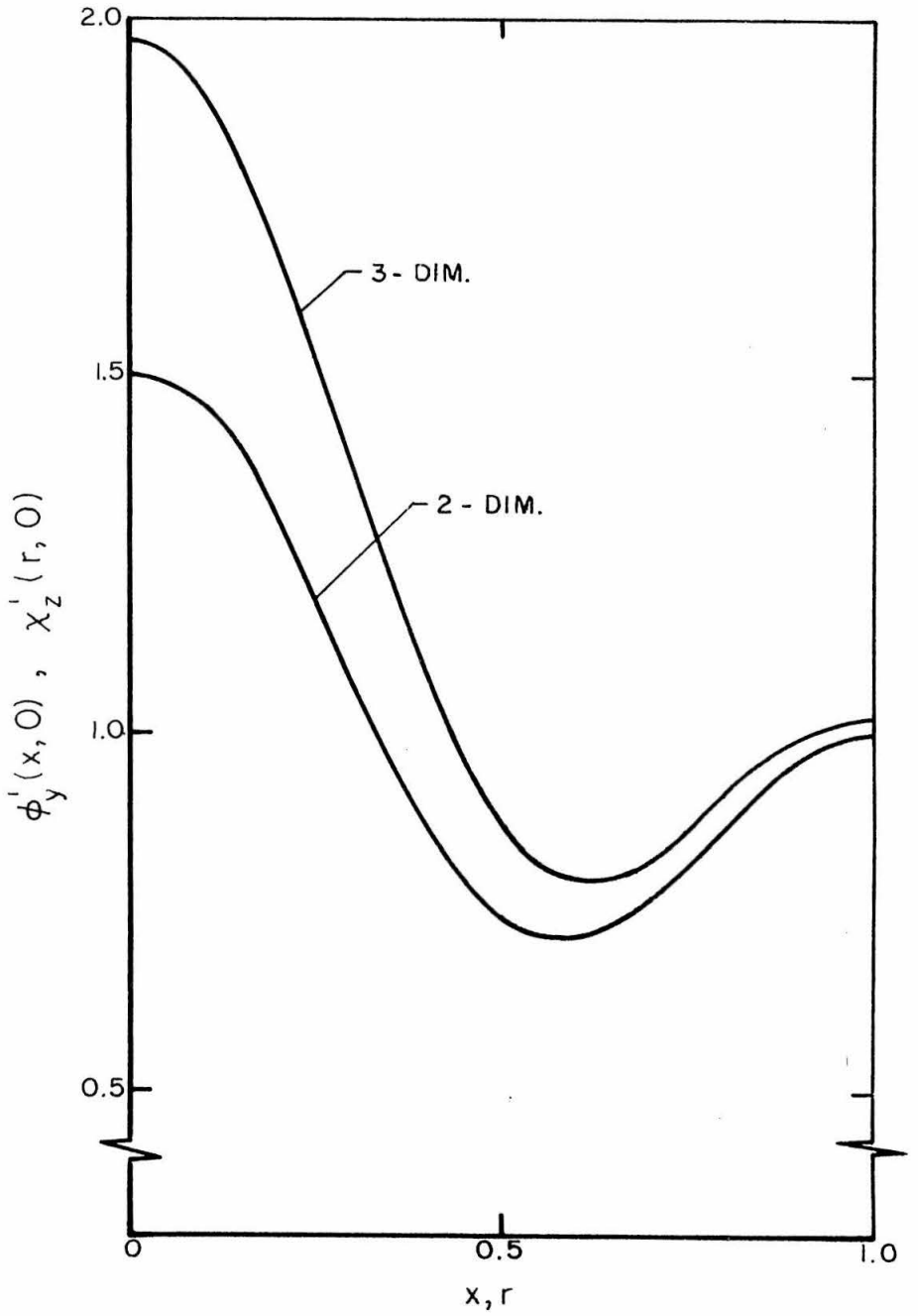

Fig. 11: Velocities along y = 0, z = 0 for nearly plane free surface.

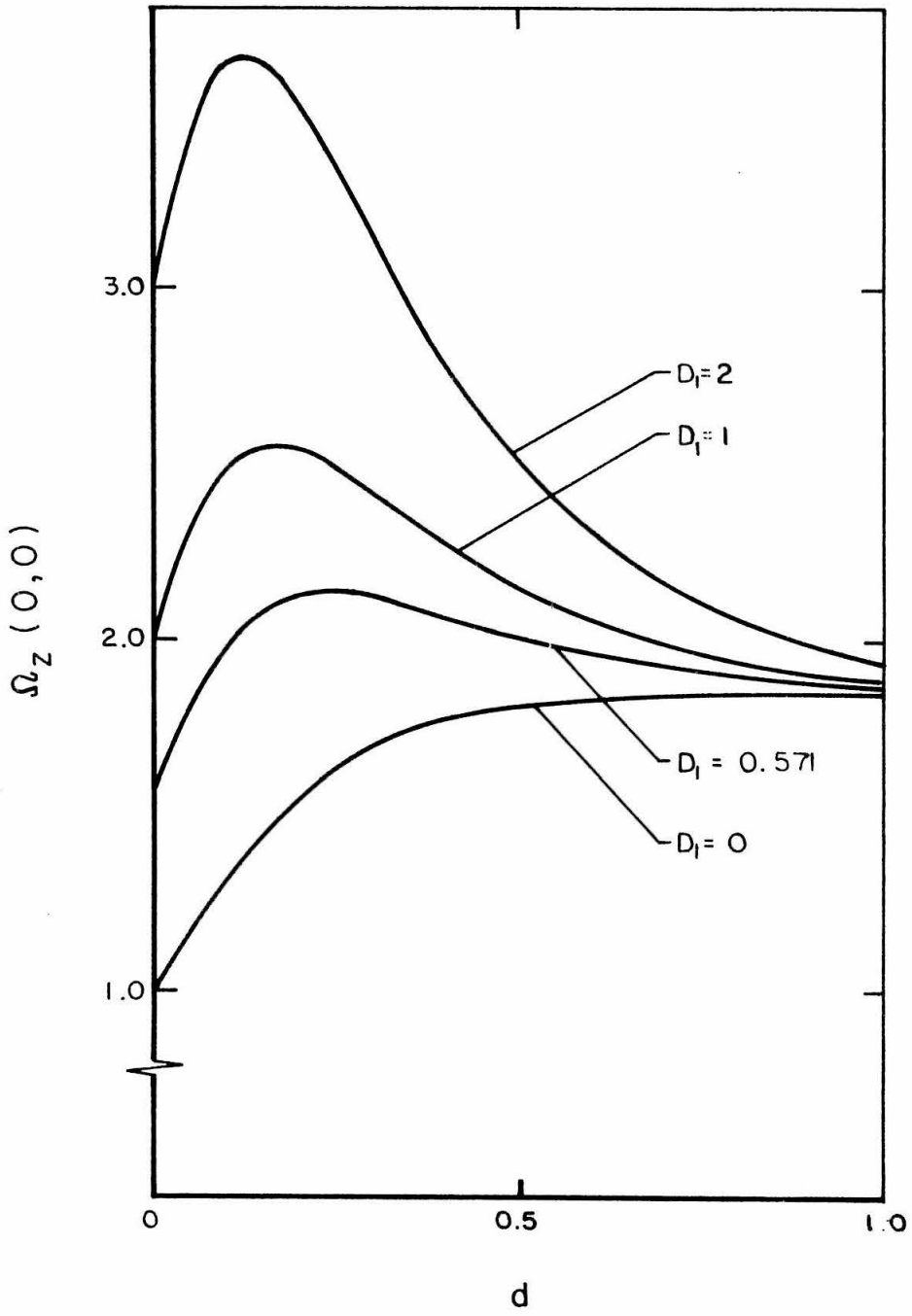

Fig. 12: Effect of finite column length on the velocity at the free surface midpoint in the case of axial symmetry.

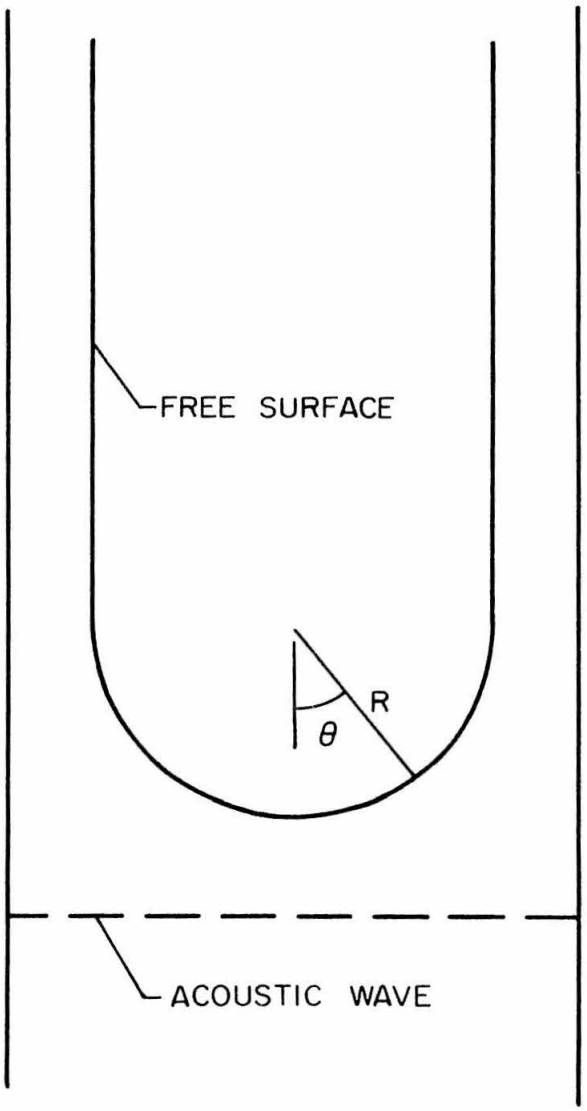

Fig. 13: Acoustic wave incident upon a curved free surface.

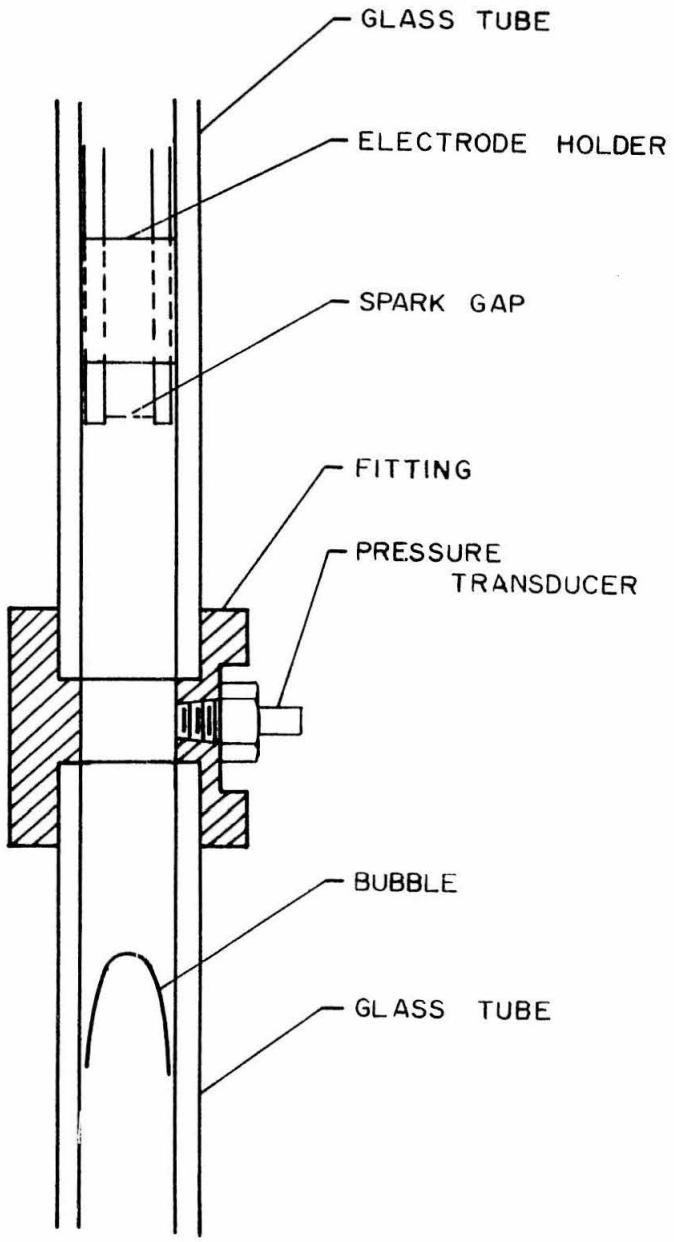

Fig. 14: Experimental apparatus.

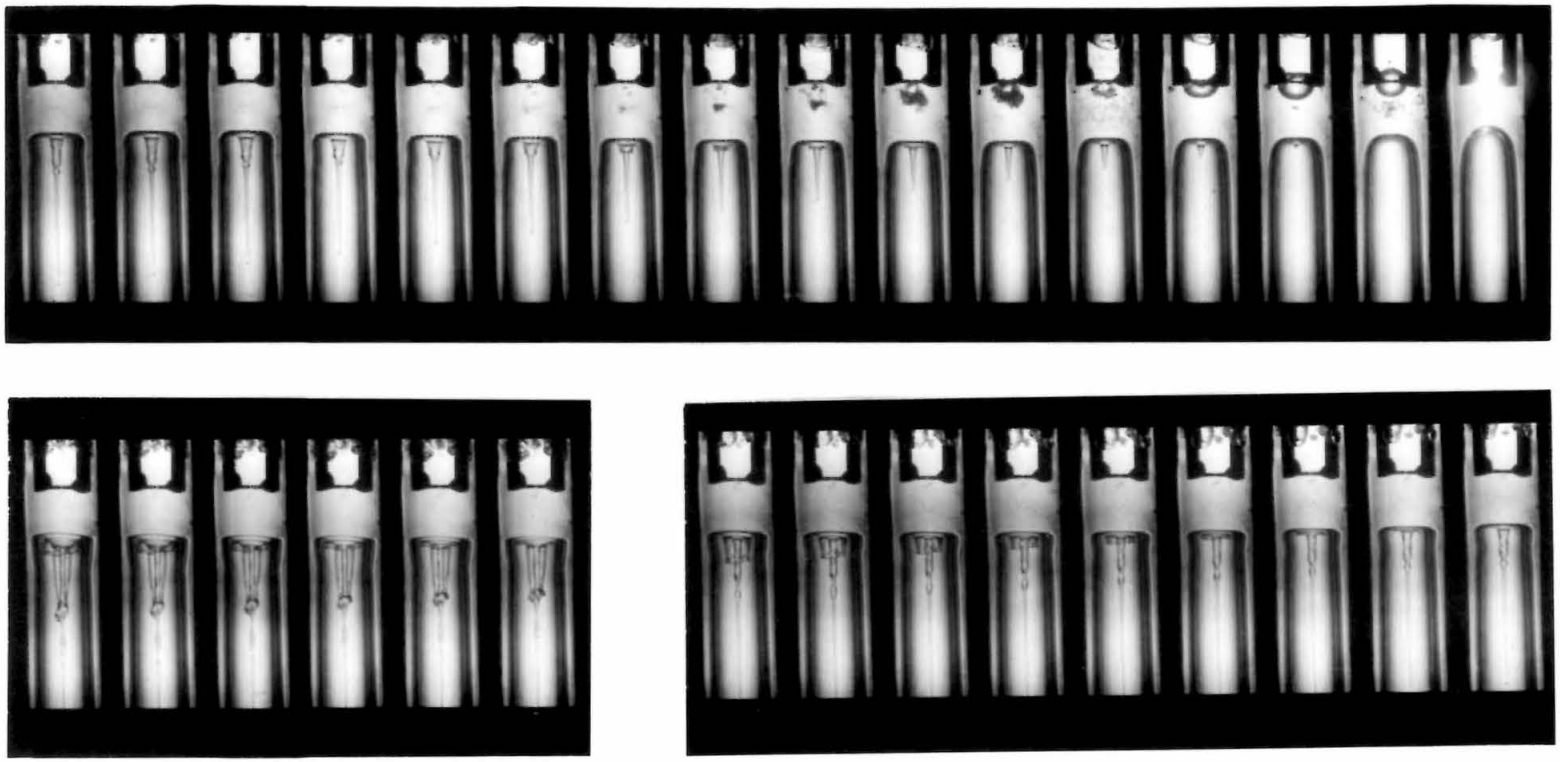

Fig. 15: Photographs of typical experiment, time increasing from right to left and top to bottom. Note cavitation in second and fifth frames and sheet jets in subsequent photographs. Top series, 0 - 2.64 ms.; rightmost strip in lower series, 2.64 - 4.12 ms; final series 5.44 - 6.44 ms. Pictures within each series 0.165 ms. apart, $d_s = 1.61$ tube radii.

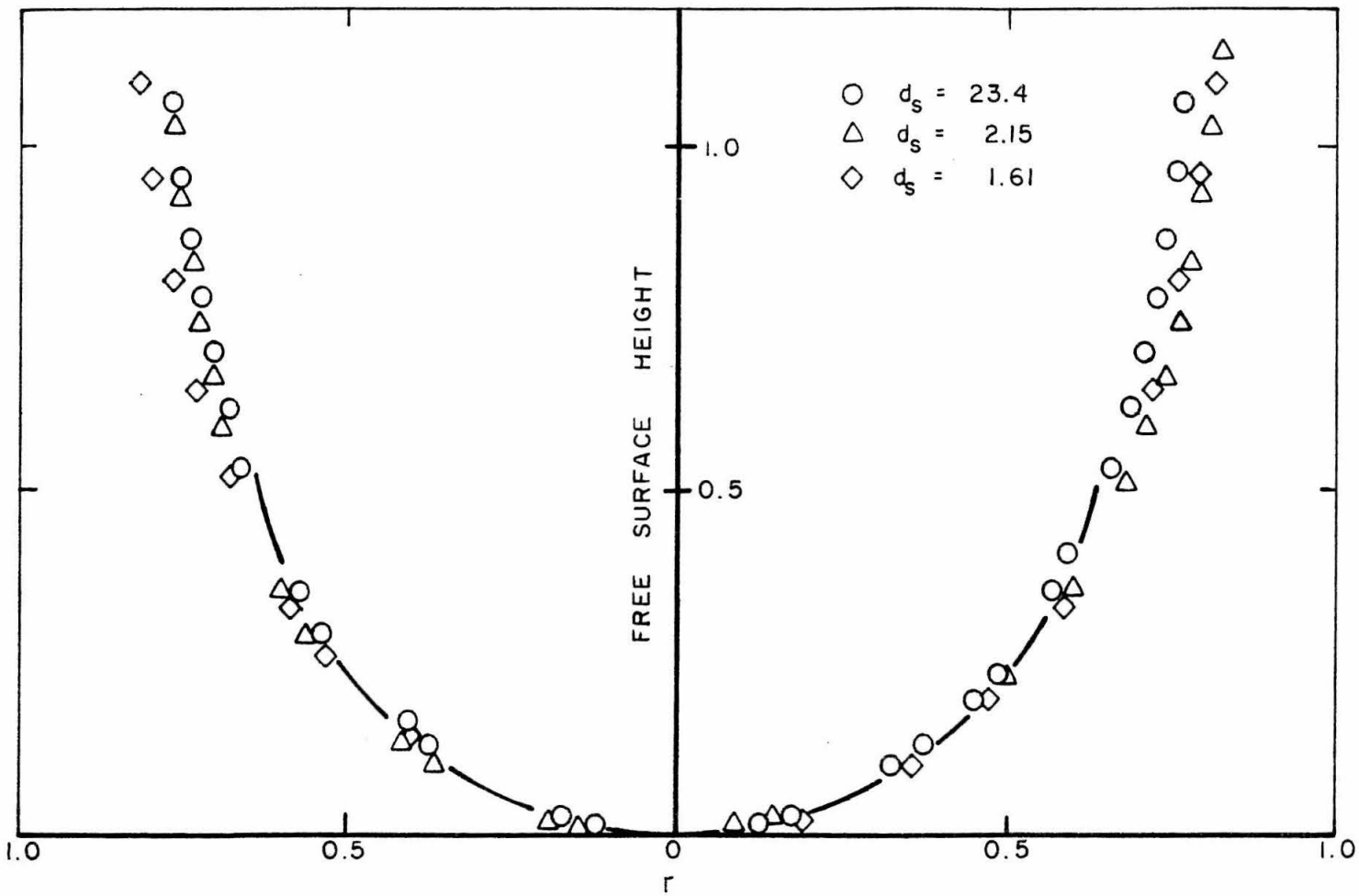

Fig. 16: Experimental free surface shapes for three typical bubbles; the arcs are of radius 0.65.

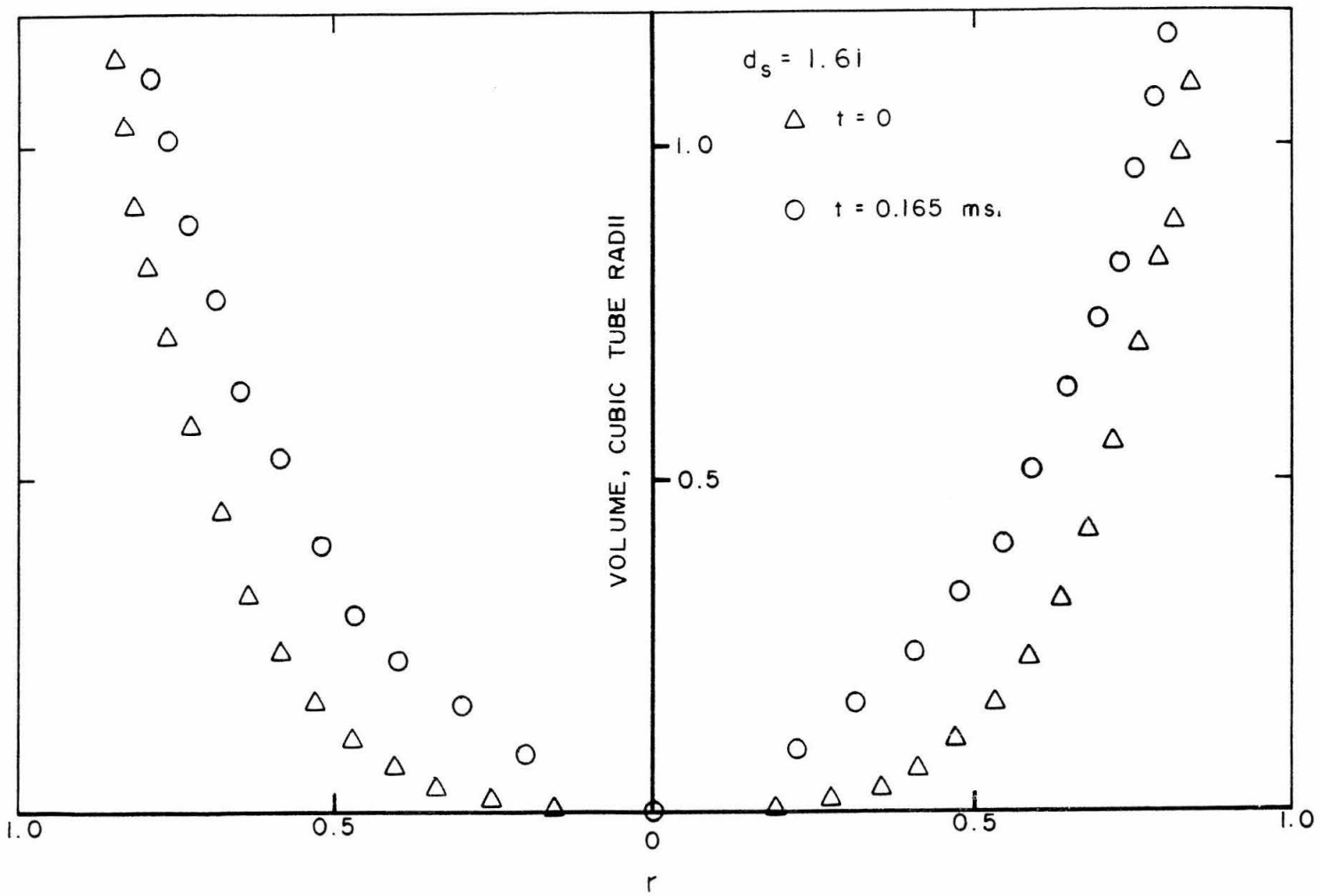

Fig. 17: Results of volume calculation in a typical case.

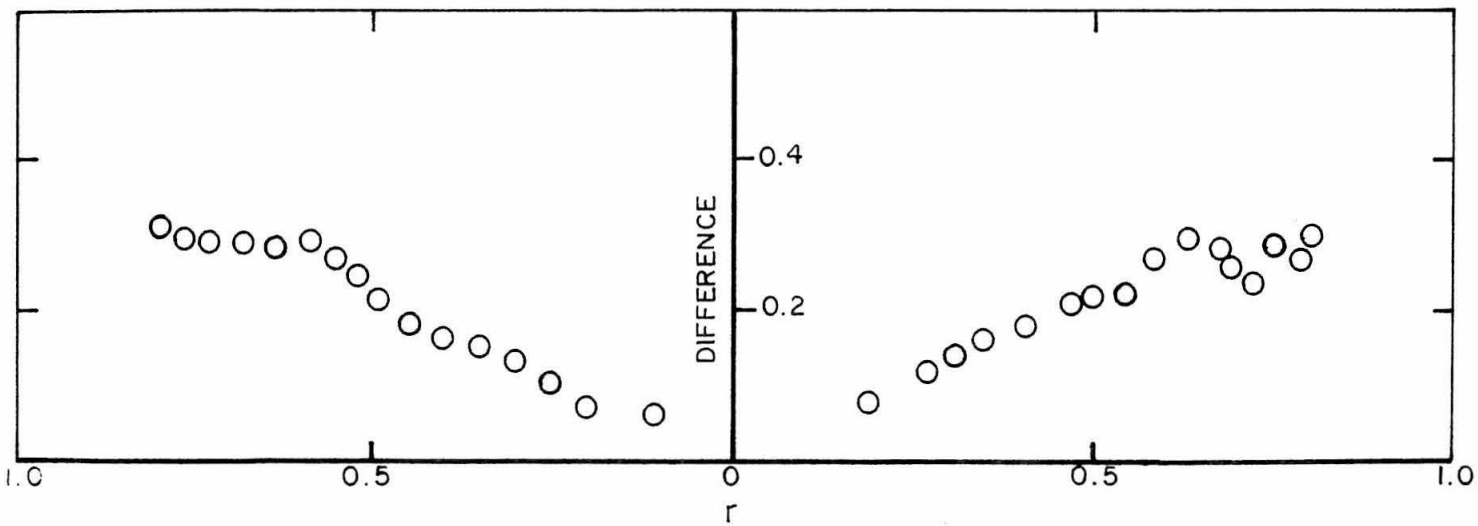

Fig. 18: Displaced volume for bubble of Fig. 17.

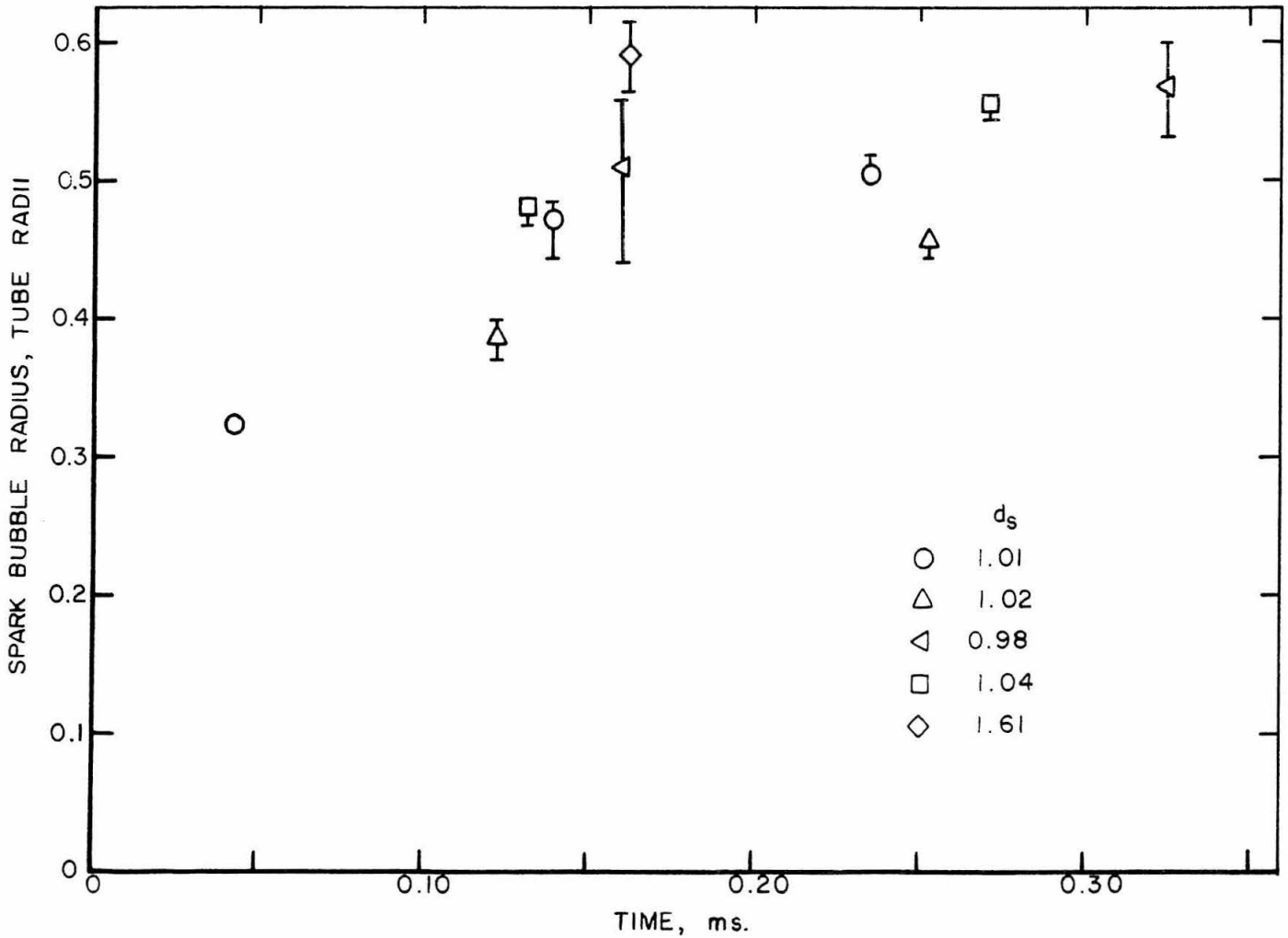

Fig. 19: Mean radii for typical spark bubbles, d_s is distance in tube radii between bubble apex and spark gap.

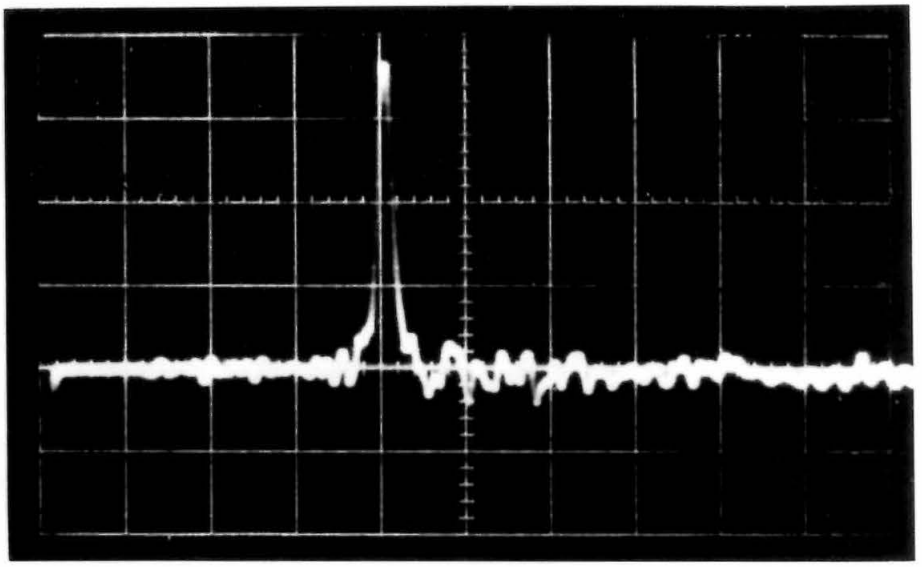

Fig. 20(a): Typical pressure history, horizontal scale: 50μs per large division, vertical scale: 100 psig per large division, spark gap 44.7 tube radii above transducer.

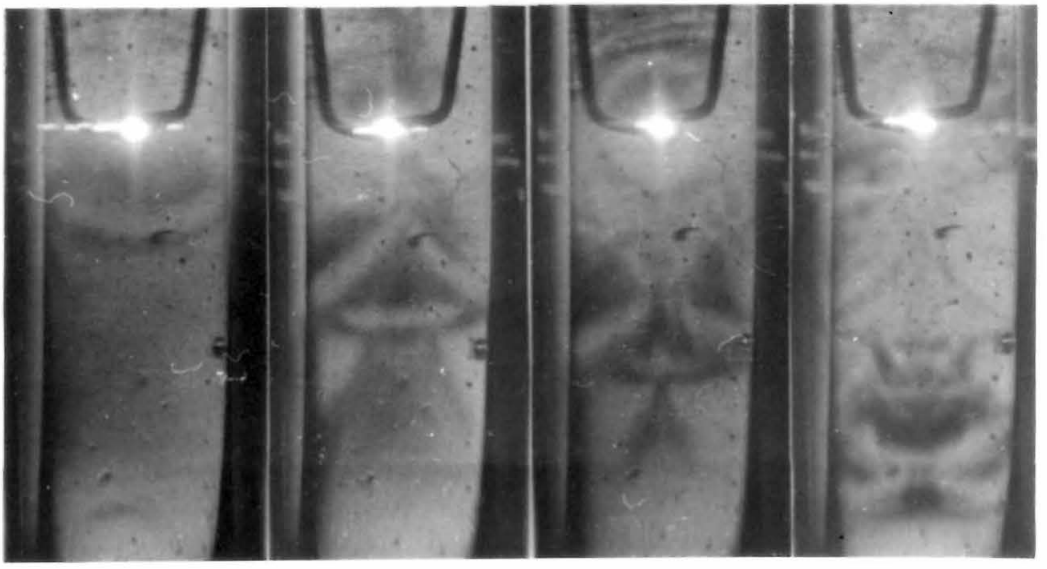

Fig. 20(b): Schlieren photographs of spark-produced pressure waves, delays are 6, 12, 15, and 25μs. with respect to spark, scale is approximately twice actual size.

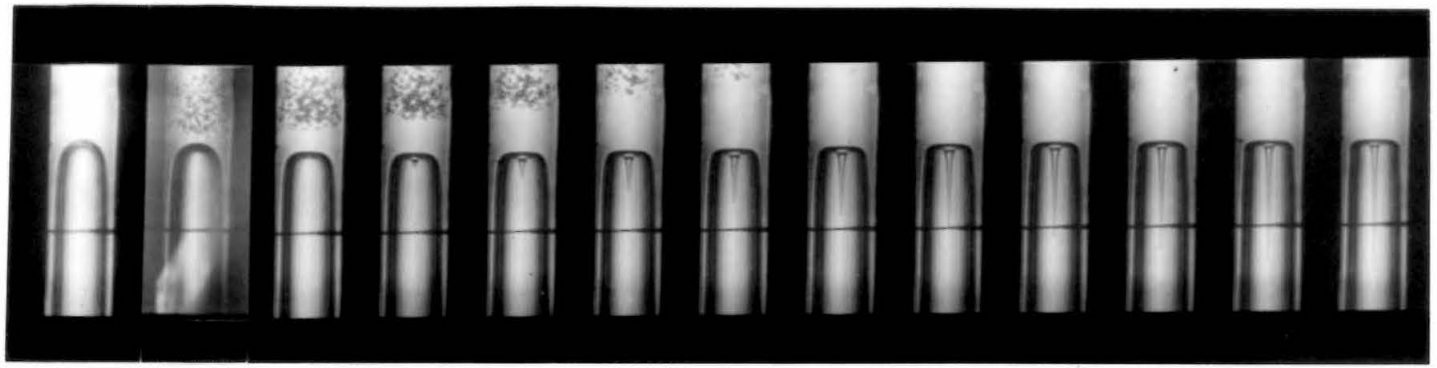

Fig. 21(a): Cavitation caused by compression wave reflection at bubble free surface, time between frames: 0.150 ms., $d_s = 23.4$.

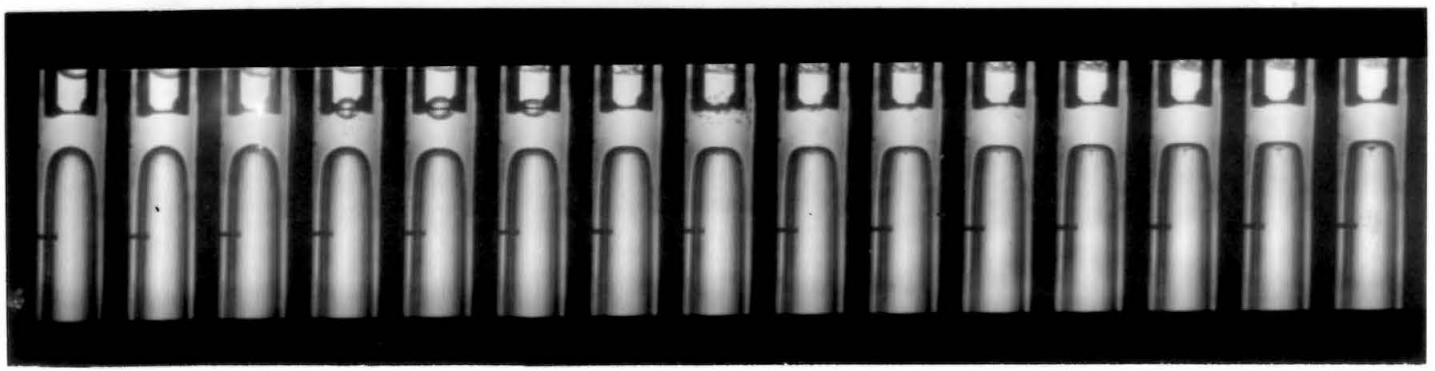

Fig. 21(b): Very small jet produced by weak acceleration, time between frames: 0.130 ms., $d_s = 1.30$.

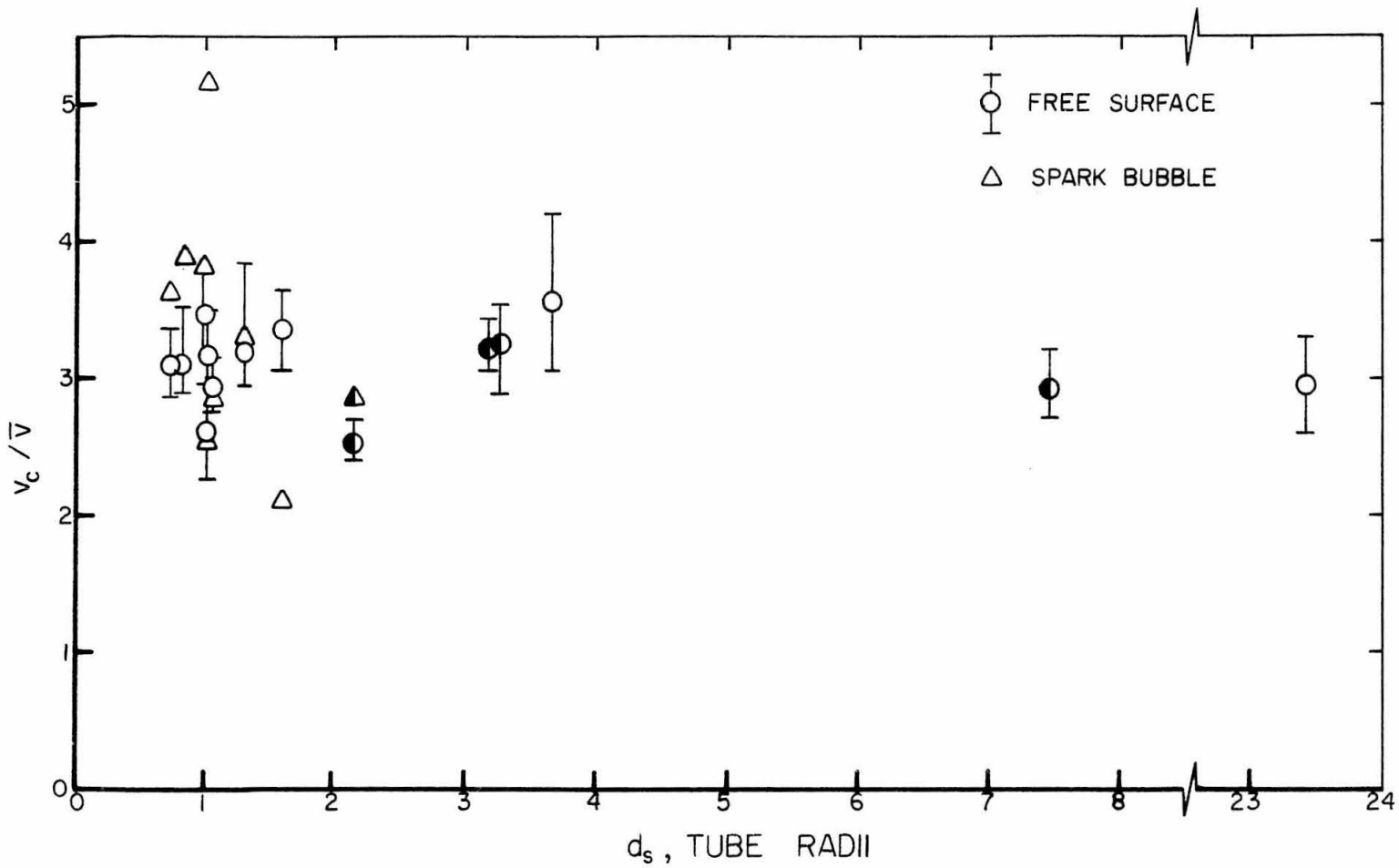

Fig. 22: Ratio of initial midpoint velocity to initial mean velocity. Mean velocity based on displaced volume at free surface and on spark bubble volume. Shaded symbols are for 50 ppm. polyethylene dioxide solution.

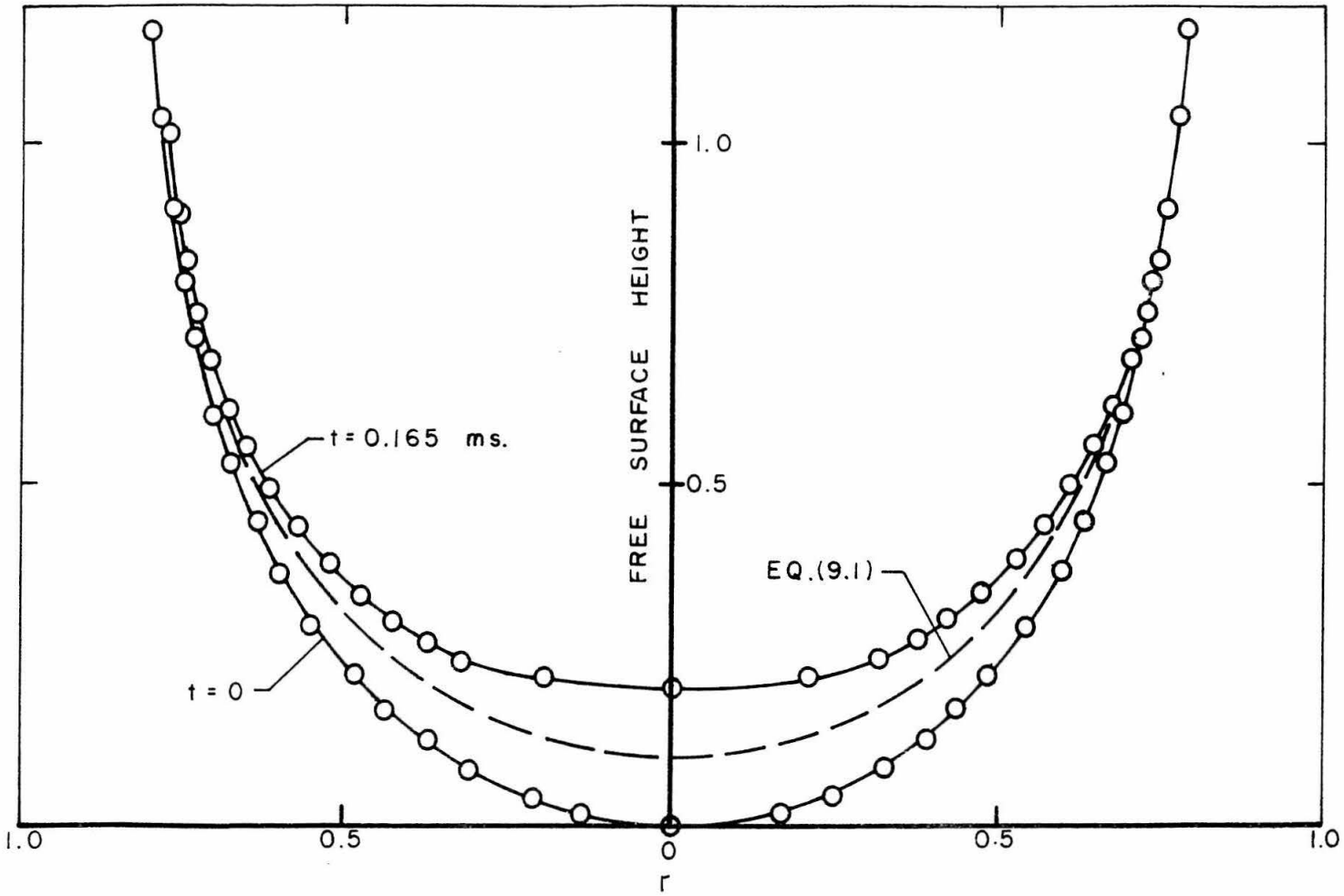

Fig. 23: Experimental free surface displacement for $d_s = 3.67$ compared to exact two-dimensional theory for long column.